

Thesis for the Degree of Doctor of Science

**Search for Pair-production of
Scalar Top Quarks Decaying via R -parity Violation
in $p\bar{p}$ Collisions at $\sqrt{s} = 1.8$ TeV**

Min Jeong Kim

Department of Physics, Major in Particle Physics
The Graduate School

June 2001

**The Graduate School
Kyungpook National University**

Search for Pair-production of Scalar Top Quarks Decaying via R -parity Violation in $p\bar{p}$ Collisions at $\sqrt{s} = 1.8$ TeV

Min Jeong Kim

Department of Physics, Major in Particle Physics
The Graduate School

Supervised by Professor Dong Hee Kim

Approved as a qualified thesis of Min Jeong Kim
for the degree of Doctor of Science
by the Evaluation Committee
June 2001

Chairman

손 동 철

조 상 규

안 창 현

김 귀 년

유 인 태

The Graduate School Council, Kyungpook National University

Contents

1	Introduction	1
2	Supersymmetric Theory (SUSY)	8
2.1	The Minimal Supersymmetric Standard Model (MSSM)	11
2.2	R-parity (R_p)	15
3	Pair-production of Scalar Top Quarks Decaying via R-parity Violation in $p\bar{p}$ Collisions	21
3.1	Scalar Top Quark	22
3.2	Pair-production Cross Section	23
3.3	Decays via R-parity Violating Couplings	23
3.4	Technique to Determine Mass Limit of Scalar Top Quark	31
4	The Experimental Apparatus	35
4.1	The Fermilab Accelerators	37
4.2	The Collider Detector at Fermilab (CDF)	41
4.2.1	The Tracking System	45
4.2.2	The Calorimetry	51
4.2.3	The Muon Detectors	54
4.2.4	The Trigger System	63

5	Monte Carlo Simulation	67
5.1	Signal & Background Monte Carlo Samples	68
5.2	Kinematics of Signals at Generator Level	71
5.3	Detector Simulation and Reconstruction	73
6	Data Analysis	75
6.1	Data Samples	76
6.2	Baseline Event Selection	79
6.2.1	Muon Selection	81
6.2.2	Tau Selection	82
6.3	$Z \rightarrow \tau\tau$ Analysis	90
6.3.1	W Event Rejection	90
6.3.2	QCD Event Rejection	92
6.3.3	Jet Veto	92
6.3.4	Efficiencies and Acceptance Estimations	94
6.3.5	Summary of Data Analysis	95
6.3.6	Background Estimation	95
6.4	$\tilde{t}_1\bar{\tilde{t}}_1$ Analysis	98
6.4.1	W Event Rejection	98
6.4.2	QCD Event Rejection	100
6.4.3	Jet Requirement	100
6.4.4	Efficiencies and Acceptance Estimations	100
6.4.5	Summary of Data Analysis	102
6.4.6	Background Estimation	102
7	Systematic Uncertainties	110
7.1	Systematic Uncertainties due to Trigger Efficiency	111

7.2	Systematic Uncertainties from $Z \rightarrow \tau\tau$ analysis	111
7.3	Systematic Uncertainties from $\bar{t}_1\bar{t}_1$ analysis	113
8	Results & Discussion	115
8.1	Results	116
8.2	Limits	119
9	Conclusion & Summary	124
A	The Main Injector (MI) and the Antiproton Recycler Ring	125
A.1	Brief History	125
A.2	Particle Acceleration in Run II	126
A.2.1	The Main Injector	126
A.2.2	The Antiproton Recycler Ring	127
B	The CDF Upgrades	128
C	Perspectives on Scalar Top Search in Run II	129

List of Tables

2.1	Supersymmetric states	14
2.2	List of pair-production and decay mechanism of different scalar fermions including the couplings and corresponding topologies [30, 31]	19
3.1	The pair-production cross section of the lightest scalar top quarks at the Tevatron from the LO and NLO QCD calculations. The renormalization and factorization scales used in the calculation are $Q = M_{\tilde{t}_1}$	26
3.2	Experimental signature for candidate event selection	28
4.1	η coverage and energy resolution for the various calorimeters. The symbol \oplus signifies the constant term to be included in quadrature to the resolution. Energy resolutions for the electromagnetic calorimeters are for incident electrons and photons. For the hadronic calorimeters, they are for pions. E_T should be expressed in GeV.	52
5.1	Possible background sources to baseline samples	69
5.2	Summary of background MC simulation samples	71

5.3	Identification efficiency for muons [38]	74
5.4	Efficiency of track isolation ($ISO^{trk} < 4 \text{ GeV}/c$) for muons. A cone size of 0.4 was used in this analysis [39].	74
5.5	Efficiency of calorimeter isolation ($ISO^{cal} < 4 \text{ GeV}$) for muons. A cone size of 0.4 was used in this analysis [39].	74
6.1	Muon identification quality cuts	81
6.2	Cuts for the second muon from $Z \rightarrow \mu\mu$	82
6.3	Hadronic tau identification quality cuts	85
6.4	Cut efficiencies and signal acceptance of $Z \rightarrow \tau\tau$ analysis . . .	94
6.5	$Z(\rightarrow \tau\tau) + 0\text{-jet}$ events from the data sample	95
6.6	Number of events in the data and background samples after each cut ($Z \rightarrow \tau\tau$ analysis)	96
6.7	Summary of yields of $\mu + \tau_h$ events in the data and simulated samples after $Z(\rightarrow \tau\tau) + 0\text{-jet}$ selection.	96
6.8	Cut efficiencies with signal acceptance and trigger efficiency at $M_{\tilde{t}_1} = 70$ and $75 \text{ GeV}/c^2$	103
6.9	Cut efficiencies with signal acceptance and trigger efficiency at $M_{\tilde{t}_1} = 80$ and $90 \text{ GeV}/c^2$	104
6.10	Cut efficiencies with signal acceptance and trigger efficiency at $M_{\tilde{t}_1} = 100$ and $110 \text{ GeV}/c^2$	105
6.11	Cut efficiencies with signal acceptance and trigger efficiency at $M_{\tilde{t}_1} = 120$ and $130 \text{ GeV}/c^2$	106
6.12	$\tilde{t}_1 \bar{\tilde{t}}_1$ events from data sample	108
6.13	Number of events in the data and background samples after each cut ($\tilde{t}_1 \bar{\tilde{t}}_1$ analysis)	109

6.14	Summary of estimated backgrounds.	109
7.1	Systematic uncertainties due to trigger efficiency, where $M_{\tilde{t}_1} = 70 \sim 130 \text{ GeV}/c^2$	111
7.2	Systematic uncertainties from $Z \rightarrow \tau\tau$ analysis.	112
7.3	Systematic uncertainties from $\tilde{t}_1\bar{\tilde{t}}_1 \rightarrow (\tau^+b)(\tau^-\bar{b}) \rightarrow \mu\tau_h b\bar{b} + X$ analysis, where $M_{\tilde{t}_1} = 70 \sim 130 \text{ GeV}/c^2$	114
8.1	95% C.L. limits on the production cross section of $\tilde{t}_1\bar{\tilde{t}}_1 + X \rightarrow (\tau^+b)(\tau^-\bar{b}) + X \rightarrow \mu\tau_h b\bar{b} + X$, where $M_{\tilde{t}_1} = 70 \sim 130 \text{ GeV}/c^2$	119
8.2	95% C.L. expected limits on the production cross section of $\tilde{t}_1\bar{\tilde{t}}_1 + X \rightarrow (\tau^+b)(\tau^-\bar{b}) + X \rightarrow \mu\tau_h b\bar{b} + X$, where $M_{\tilde{t}_1} = 70 \sim 130 \text{ GeV}/c^2$	120
8.3	95% C.L. limits on the production cross section of $\tilde{t}_1\bar{\tilde{t}}_1 + X \rightarrow (\tau^+b)(\tau^-\bar{b}) + X \rightarrow e\tau_h b\bar{b} + X$, where $M_{\tilde{t}_1} = 70 \sim 130 \text{ GeV}/c^2$ [27].	122
8.4	Results of the $Z \rightarrow \tau\tau$ analysis [27, 28]	122
8.5	95% C.L. Combined limits on the production cross section of $\tilde{t}_1\bar{\tilde{t}}_1 + X \rightarrow (\tau^+b)(\tau^-\bar{b}) + X \rightarrow \ell\tau_h b\bar{b} + X$, where $M_{\tilde{t}_1} = 70 \sim 130 \text{ GeV}/c^2$	123

List of Figures

3.1	Feynman diagrams for the dominant $\tilde{t}_1\bar{\tilde{t}}_1$ production mechanisms at the Tevatron	24
3.2	The pair-production cross section of the lightest scalar top quarks at the Tevatron	25
3.3	Experimental signature	28
3.4	Feynman diagrams of the scalar top quark decays via $\mathcal{R}_p \lambda'_{33k}$ couplings, where $k = 1, 2, 3$	30
4.1	A schematic view of the Fermilab accelerators	38
4.2	Diagram showing the production of antiprotons	40
4.3	Isometric view of the CDF with a quadrant cut away to show the tracking system	42
4.4	Quarter section of the CDF with coordinate system definition	43
4.5	Schematic drawing of one of the SVX' modules (barrels). Two modules are joined at the dummy ear sides.	47
4.6	Schematic drawing of one of the SVX' ladders	47
4.7	An endplate of the CTC showing the arrangement of the blocks which hold the 84 layers of sense wires	50

4.8	The η - ϕ segmentation of the CDF calorimeters. The shaded area in the forward/backward region is where there is only electromagnetic coverage, and the black area has no coverage at all due to the presence of Tevatron steering magnets.	53
4.9	The central muon detection coverage in the η - ϕ plane	55
4.10	A drawing of a CMU tower showing a muon track.	57
4.11	Configuration of the CMP/CSP system and steel absorber. The circles on the walls are the ends of PMTs. On the top and bottom, the trapezoids are the light-guides viewed end-on. This figure includes the part planned to be upgraded for the next run, Run II [45].	59
4.12	Detail showing the configuration of steel, drift chambers, the scintillation counters for the CMP walls. A muon track is drawn to establish the interaction point. Counter readout is located at $z = 0$. Layers of scintillation counters are offset from the chambers and from each other in x to allow overlapping light-guides and PMTs, minimizing the space required [45].	60
5.1	The p_T or E_T (left) and η (right) distributions of muons (top), hadronic taus (middle) and b quarks (bottom) at the event generator level. $M_{\tilde{t}_1} = 100 \text{ GeV}/c^2$	72
6.1	The CDF Run I experiment and its integrated luminosity . . .	77
6.2	Trigger efficiency curves as a function of p_T (left) and p_T^{-1} (right) in Run IA (top) and Run IB (bottom)	80
6.3	Hadronic tau identification	84

6.4	Distributions of (a) $M(\mu, \tau_h)$, (b) \cancel{E}_T , (c) $\Delta\phi(\mu, \tau_h)$ and (d) $\Delta\phi(\mu, \cancel{E}_T)$ for 163 OS and 82 LS $\mu + \tau_h$ events from the data sample.	86
6.5	Distributions of (a) $p_T(\mu)$, (b) $p_T(\tau_h)$ and (c) the number of jets for 163 OS and 82 LS $\mu + \tau_h$ events from the data sample. . . .	87
6.6	Distributions of (a) $M(\mu, \tau_h)$, (b) \cancel{E}_T , (c) $\Delta\phi(\mu, \tau_h)$ and (d) $\Delta\phi(\mu, \cancel{E}_T)$ for OS–LS events in the data and simulated samples.	88
6.7	Distributions of (a) $p_T(\mu)$, (b) $p_T(\tau_h)$ and (c) the number of jets for OS–LS events in the data and simulated samples.	89
6.8	Distributions of $M_T(\mu, \cancel{E}_T)$ (top) and $S_{Z \rightarrow \tau\tau} / \sqrt{B_{W+jet}}$ (bottom).	91
6.9	Distributions of $ \vec{p}_T(\mu) + \vec{\cancel{E}}_T $ (top) and $S_{Z \rightarrow \tau\tau} / \sqrt{B_{QCD}}$ (bottom).	93
6.10	Distributions of (a) $p_T(\mu)$, (b) $p_T(\tau_h)$, (c) $\Delta\phi(\mu, \tau_h)$, (d) $\Delta\phi(\mu, \cancel{E}_T)$, (e) \cancel{E}_T and (f) $M(\mu, \tau_h)$ in the data and simulated samples after $Z(\rightarrow \tau\tau) + 0$ -jet selection.	97
6.11	Distributions of $M_T(\mu, \cancel{E}_T)$ (top), $M_T(\mu, \cancel{E}_T)$ for $\tilde{t}_1 \bar{\tilde{t}}_1$ and $W +$ jet events (middle) and $\varepsilon_{\tilde{t}_1 \bar{\tilde{t}}_1 \rightarrow \tau\tau b\bar{b}} / \sqrt{\varepsilon_{W+jets}}$ (bottom)	99
6.12	Distribution of $H_T(\mu, \tau_h, \cancel{E}_T)$ (top), $H_T(\mu, \tau_h, \cancel{E}_T)$ for $\tilde{t}_1 \bar{\tilde{t}}_1$ and QCD events (middle) and $\varepsilon_{\tilde{t}_1 \bar{\tilde{t}}_1 \rightarrow \tau\tau b\bar{b}} / \sqrt{\varepsilon_{QCD}}$ (bottom)	101
6.13	Jet multiplicity	102
6.14	Cumulative efficiencies of the $\tilde{t}_1 \bar{\tilde{t}}_1$ event selection cuts vs $M_{\tilde{t}_1}$.	107
8.1	95% C.L. limits for $\tilde{t}_1 \bar{\tilde{t}}_1 + X \rightarrow (\tau^+ b)(\tau^- \bar{b}) + X \rightarrow \mu \tau_h b\bar{b} + X$ along with the NLO QCD calculation	118
8.2	95% C.L. limits for $\tilde{t}_1 \bar{\tilde{t}}_1 + X \rightarrow (\tau^+ b)(\tau^- \bar{b}) + X \rightarrow \ell \tau_h b\bar{b} + X$ along with the NLO QCD calculation	121

C.1 The pair-production cross section of the lightest scalar top quark at the Tevatron in Run II	130
---	-----

Chapter 1

Introduction

The patterns in the phenomena of nature
that are not apparent to the eye,
but only to the eye of analysis.

– Richard Feynman –

What are the fundamental building blocks of matter and how are they held together? This is the essential question that human beings have pondered from their beginning. Although the answer has changed as time goes by, it provides the best way to understand nature at least at the time. Today, particle physics provides a basic understanding of a variety of natural phenomena in terms of a few elementary particles and their interactions. By definition, a particle is considered to be elementary only if there is no evidence that it is made up of more fundamental constituents. It behaves in a point-like way. In nature, there are four interactions known as electromagnetic, weak, strong and gravitational forces.

Elementary particles are classified into fermions and bosons according to their spin: fermions (bosons) have half-integral (integer) spin. The particles constituting the matter are all fermions, while the particles carrying the forces are all bosons. Fermions are classified into quarks which feel all forces, and leptons which don't feel strong force. The electromagnetic, weak, strong and gravitational forces are mediated by the photon, weak gauge bosons, gluons and graviton, respectively. The graviton is a postulated particle which has not yet been seen. Because the gravitational force (or gravity) is significantly weaker than the other three forces, its mediator is much more difficult to detect. Every type of particle has a corresponding antiparticle. Some neutral particles are their own antiparticles. Antiparticles are conventionally denoted by a $-$.

Many other particles called "hadrons" can be built out of the quarks by means of two particular combinations. The baryons composed of three quarks have half-integral spin. The proton and neutron belong to this class. The mesons composed of a quark and an antiquark have integer spin. The strong interaction plays a crucial role in binding quarks and gluons together to form hadrons.

Recently, many theories have linked elementary particles with one of the grandest questions: how did the universe begin? These theories suggest that many of the complexities manifest at lower energies would be greatly simplified at extremely high energy. At such a high energy, the different forces would be seen as different manifestations of a single universal force. There is no doubt that these energies prevailed at the time of the "big bang" that initiated the expansion of the universe [1].

The Standard Model (SM) is a currently accepted theory which successfully describes the properties and interactions of the elementary particles. The

successes of the last thirty years in particle physics have been embodied in the Standard Model, which contains electroweak and strong interactions. In the 1960s, the electroweak theory of Weinberg, Salam and Glashow demonstrated the unification of electromagnetic and weak forces. The electromagnetic and weak forces are different manifestations of a single unified force called “electroweak.” The model has passed many stringent experimental tests. In the 1970s, Quantum Chromodynamics (QCD) describing the strong interactions between quarks and gluons emerged as a mathematically consistent theory. In the 1980s, trijet phenomena were observed in e^+e^- collisions, which were the first apparent signature of gluon’s existence and strong evidence to support the theory. Quantum Chromodynamics has become one of the cornerstones of the Standard Model.

In the Standard Model, all known quarks (q)¹ and leptons (ℓ)² – each comes in six “flavors” – are arranged in a three “family” (or “generation”) structure. The Standard Model is a quantum field theory based on the gauge symmetry group $SU(3)_C \times SU(2)_L \times U(1)_Y$ with spontaneous breaking of the $SU(2)_L \times U(1)_Y$ symmetry through the Higgs mechanism. The Higgs mechanism invokes a special kind of neutral scalar particle called the “Higgs boson” (H). The Higgs boson is unlike either a matter particle or a force-carrying particle. Interaction of the Higgs boson with other particles generates particle masses. The Higgs bosons give fermions their mass via Yukawa interactions for which the coupling is proportional to the fermion mass. They couple to the weak gauge bosons with the normal weak interaction strength providing them

¹The quark comes in three colors: red, green and blue.

²The neutrino masses are not yet measured. They are very small. Recently, there is experimental evidence that they are nonzero.

with large mass. Before spontaneous symmetry breaking, all the gauge bosons are massless. When the symmetry is broken through the Higgs mechanism, the weak gauge bosons become massive. Many extensions of the Standard Model retain the Higgs mechanism as the primary method for mass generation, but with more complicated Higgs sectors and more Higgs bosons. The three interactions arise by requiring invariance under the local gauge transformations described by the group generators. The broken $SU(2)_L \times U(1)_Y$ symmetry describes the electromagnetic and weak interactions. The $SU(3)_C$ symmetry describes the strong interaction. The production cross sections and decay branching ratios for the various interactions are accurately predicted in the theory. So far the Standard Model has been in remarkable agreement with the experimental measurements [2, 3, 4, 5].

In spite of its success, the Standard Model is regarded as merely a good low energy effective theory, since it builds on many assumptions and still leaves open many theoretical questions which can be answered only by the introduction of new physics. Here “low energy” means energies presently achievable by experiments. First, the Standard Model has nineteen free parameters which cannot be predicted from first principles but must be measured by experiments including the masses of the elementary particles and the coupling strengths of the forces [6, 7, 8, 9]. Second, the gauge symmetry group of the Standard Model is a direct product of three groups with three independent coupling constants. It does not explain the three family structure of quarks and leptons, and the observed pattern of the particle masses. The particle masses are fixed by arbitrary Yukawa couplings. Third, the Higgs sector, responsible for the electroweak symmetry breaking and the fermion masses, has not been verified experimentally and the mass of the Higgs boson is unstable

under higher order corrections involving loop effects in quantum field theory, even though consistency requires that it should be less than a few TeV. The Standard Model Lagrangian contains terms that are quadratically divergent unless unnatural “fine-tuning” takes place. As a consequence, the Standard Model has a large hierarchy of scales that exists between the mass scale of the weak interaction, set by the Fermi coupling constant G_F (or the W mass, M_W), and that of gravity, set by Newton’s constant G_N (or the Planck Mass, $M_P \sim 10^{19} \text{ GeV}/c^2$). It is known as “naturalness/hierarchy problem.” Fourth, the gravitational force is not included in the theory. Fifth, the source of CP (C: particle-antiparticle exchange symmetry, P: space inversion symmetry) or time-reversal symmetry violation³ – a phenomenon that bears on the apparent dominance of matter over antimatter in the universe – has not been clarified. Finally, the Standard Model fails to provide a “cold dark matter” candidate. All of these facts lead us to believe that there must be a theory beyond the Standard Model.

There have been various theoretical attempts to solve the problems of the Standard Model such as quark compositeness, technicolor, left-right symmetric model, supersymmetric theory (SUSY) and large extra dimensions. Each of them solves some problems of the Standard Model, and has their own set of strengths and weaknesses. No experimental evidence for any of them has been discovered yet.

Supersymmetric theory is a natural extension to the Standard Model. It provides a solution to the hierarchy problem by proposing a new type of space-

³After the discovery of large C and P violation in the weak interaction, it appeared that the product CP was a good symmetry. In 1964, CP violation was observed in K^0 decays. Larger CP violation effects are anticipated in B^0 decays.

time symmetry called “supersymmetry” between fermions and bosons. All the Standard Model particles have their own “superpartners” by the theory: every fermion (boson) has a bosonic (fermionic) superpartner. New scalar particles cancel the quadratic divergences involving Yukawa interactions without fine-tuning. The evidence of supersymmetry may be seen in the running of three gauge coupling constants. Gauge coupling constants extrapolated to very high energies don’t converge at a single point in the Standard Model, but they do at a scale ($M_{GUT} \sim 10^{16} \text{ GeV}/c^2$) when supersymmetric Renormalization Group Equations (RGE) are taken into account. This could be the evidence of the Grand Unified Theories (GUT), too. Besides, supersymmetric theory predicted a heavy top quark in the early 1980s, and provided a connection between the Standard Model forces and gravitational force and a candidate for the cold dark matter of the universe before astronomy demonstrated the need for non-baryonic cold dark matter. The Minimal Supersymmetric Standard Model (MSSM) expands the Standard Model with minimum number of new particles and interactions while remaining consistent with observation. It has one hundred and twenty-four free parameters. A series of assumptions can reduce the number of free parameters to a manageable number.

Supersymmetric theory defines a new multiplicative quantum number called “ R -parity” (R_p), which distinguishes Standard Model particles from their superpartners: Standard Model particles (their superpartners) have even (odd) R -parity. The Minimal Supersymmetric Standard Model is constructed to conserve both baryon number (B) and lepton number (L) so that R -parity Conservation (RPC) is imposed on the couplings. If R -parity is conserved, superpartners can only be produced in pairs and the Lightest Supersymmetric Particle (LSP) should be stable to be a candidate of dark matter. However,

the conservation of R -parity is not required by supersymmetric theory or gauge invariance in general. There is considerable theoretical and phenomenological interest in studying the implications of R -parity Violation (RPV, \mathcal{R}_p). In this alternative scenario, the Lightest Supersymmetric Particle is not stable any longer and various new decays have to be considered in supersymmetry search.

This analysis poses a search for pair-production and R -parity violating decays of the lightest scalar top quark (\tilde{t}_1), a superpartner of the top quark, using 106 pb^{-1} of data in proton-antiproton ($p\bar{p}$) collision at a center-of-mass energy (\sqrt{s}) of 1.8 TeV collected by the Collider Detector at Fermilab (CDF) in the 1992 – 1995 run of the Tevatron Collider at Fermilab.

This thesis is organized as follows. In this chapter, an overview on the Standard Model has been given to present the theoretical motivations of this analysis. Chapter 2 introduces supersymmetric theory with emphasis on the aspects relevant to this analysis. Chapter 3 outlines this analysis in detail with the explanation on the technique to determine the mass limit of scalar top quark through the calibration of the result with an analysis of $Z \rightarrow \tau\tau$ events. Chapter 4 summarizes the Fermilab accelerators and CDF detector. Chapter 5 describes the Monte Carlo simulation for signal and background modeling. Chapter 6 describes data samples and candidate event selection cuts. We estimate the efficiencies of those cuts, and signal acceptances. We summarize the results of data analysis. The background estimation is also detailed in the same chapter. Chapter 7 describes the systematic uncertainties from possible sources and determines the total systematic uncertainty of this analysis. Finally, a 95% C.L. upper limit on $\sigma_{\tilde{t}_1\bar{\tilde{t}}_1}$ is derived in Chapter 8. By comparing the limit to the Next-to-Leading Order (NLO) theoretical calculations, we set a 95% C.L. lower limit on the mass of scalar top quark.

Chapter 2

Supersymmetric Theory (SUSY)

Supersymmetry is a generalization of the space-time symmetry of quantum field theory that transforms fermions into bosons and vice versa. In supersymmetric theory [10, 11], all the Standard Model particles have their own superpartners and they are combined into a superfield differing by one-half unit of spin: every fermion (boson) has a spin-0 bosonic (spin- $\frac{1}{2}$ fermionic) superpartner. The name of the scalar partner of a Standard Model fermion is obtained by putting an “s” in front. The name of the fermionic partner of a Standard Model boson is obtained by putting an “ino” at the end. Superpartners are conventionally denoted by a \sim . For example, the superpartners of quarks and leptons are spin-0 bosons: squarks (\tilde{q}), charged sleptons ($\tilde{\ell}$) and sneutrinos ($\tilde{\nu}$). Supersymmetry is a hypothetical symmetry to propose that the basic laws are symmetric under interchanging bosons and fermions in the appropriate manner. If supersymmetry were an exact symmetry, Standard Model particles and their superpartners would be degenerate in mass. However, Standard Model particles don’t have the same mass as their superpartners. Therefore, supersymmetry cannot be an exact symmetry and must

be broken. It has been shown that mathematically consistent supersymmetric quantum field theory can be constructed. Supersymmetric theory is considered to provide solutions on major problems of the Standard Model. It contains many desirable features. However, the physics of supersymmetry breaking is not yet understood well: how is supersymmetry broken? This is the essential question for supersymmetric theory both theoretically and experimentally.

In low energy supersymmetric theories, the scale of supersymmetry breaking is tied to the electroweak scale characterized by the Standard Model Higgs vacuum expectation value of $v = 2M_W/g = (\sqrt{2}G_F)^{\frac{1}{2}} = 246$ GeV, where g and G_F denote the running coupling constant for the non-Abelian SU(2) field and the Fermi coupling constant, respectively. This solves the hierarchy problem: it is possible that supersymmetry will explain the origin of the large hierarchy of energy scales from the W mass to the Planck scale. In supersymmetric theory, we are allowed to introduce widely separate energy scales such as the weak scale characterized by M_W , the scale of the Grand Unified Theories and Planck scale without having to worry about quantum corrections, as long as the mass splitting between Standard Model particles and their superpartners does not greatly exceed more than 1 TeV. At present, there is little experimental evidence for low energy supersymmetry. However, if experimentation at future colliders uncovers evidence for supersymmetry, this would have a profound effect on the study of TeV-scale physics and the development of a more fundamental theory of mass and symmetry breaking phenomena in particle physics.

Currently, we don't know for sure whether an elementary Higgs boson does exist. However, supersymmetric theory is still interesting, since it realizes the idea of spontaneous breaking of gauge symmetries in the simplest

way. While one can speak of supersymmetric theory, where predictions for measurable quantities in terms of a few as-yet unknown parameters can be reliably derived, the same cannot be said for models that attempt to make do without elementary scalars. In supersymmetric theory, the mass of the Higgs boson is stabilized under higher order corrections because the loops containing Standard Model particles is partially cancelled by the contributions from loops containing their superpartners.

If the notion of the Grand Unified Theories is added into the Minimal Supersymmetric Standard Model, the three gauge couplings unify at a scale, M_{GUT} . Measurements of the gauge couplings at the CERN¹ Large Electron Positron (LEP) collider and neutral current data are in good agreement with MSSM-GUT with the supersymmetric scale $M_{SUSY} \leq 1$ TeV. In addition, the unification scale in SUSY-GUT is high enough to predict proton decay rate slower than present experimental limits, as opposed to the non-SUSY-GUT, where the proton decays too fast.

Supersymmetry would support another even more comprehensive theory called “string theory.” Traditionally, elementary particles have been modeled as points that take up no space at all. This approach leads to some theoretical problems, since two particles could get extremely close and exert arbitrarily large forces on each other. String theory solves this problem by picturing particles as extremely tiny vibrating loops with the details of their vibrations determining their properties and interactions. This simple idea leads to a theory that is able to encompass all of the forces of nature including gravity in a unified and self-consistent manner.

¹The European Laboratory for Particle Physics

2.1 The Minimal Supersymmetric Standard Model (MSSM)

In the Minimal Supersymmetric Standard Model [12, 13, 14, 15], every fermion has a bosonic superpartner which has the same quantum numbers as fermion except for the spin and vice versa. Two Higgs doublets are required to generate mass for both “up”-type quarks and “down”-type quarks and charged leptons, which is the minimal structure for the Higgs sector to establish an anomaly-free theory. Supersymmetry breaking is accomplished by including the most general renormalizable soft-supersymmetry-breaking terms consistent with the $SU(3) \times SU(2) \times U(1)$ gauge symmetry and baryon and lepton number conservation. These terms parameterize our ignorance of the fundamental mechanism of supersymmetry breaking.

The parameters of the MSSM are conveniently described by considering separately the supersymmetry-conserving and supersymmetry-breaking sectors. The parameters of the supersymmetry-conserving sector consist of:

- gauge couplings: g_s , g and g' , corresponding to the Standard Model gauge group $SU(3) \times SU(2) \times U(1)$ respectively
- a supersymmetry-conserving Higgs mass parameter: μ
- Higgs-fermion Yukawa coupling constants: λ_f ($f = u, d, e, c, s, \mu, t, b, \tau$), corresponding to the coupling of quarks, leptons and their superpartners to the Higgs bosons and higgsinos

The parameters of the supersymmetry-breaking sector consist of:

- gaugino Majorana masses: M_3 , M_2 and M_1 associated with the SU(3), SU(2) and U(1) subgroups of the Standard Model
- scalar squared-mass parameters for the squarks and sleptons: M_Q^2 , M_U^2 , M_D^2 , M_L^2 and M_E^2 corresponding to the five electroweak gauge multiplets, which, for example, are superpartners of $(u, d)_L$, u_R^c , d_R^c , $(\nu, e^-)_L$ and e_R^c when only the first generation is considered. Q and L are the lepton and quark left-handed doublet superfields, respectively. Namely, E^c , U^c and D^c are right-handed singlet charge conjugate superfields for the charged leptons and down-type and up-type quarks, respectively.
- coefficients for Higgs-squark-squark and Higgs-slepton-slepton trilinear couplings: A_f (called “A-parameters,” $f = u, d, e, c, s, \mu, t, b, \tau$)
- three scalar Higgs squared-mass parameters: two of them contribute to the diagonal Higgs squared-masses, given by $m_1^2 + |\mu|^2$ and $m_2^2 + |\mu|^2$, and one off-diagonal Higgs squared-mass, $m_{12} \equiv B\mu$ (called “B-parameter”). These parameters can be re-expressed in terms of the two Higgs vacuum expectation values, v_u and v_d , and one physical Higgs mass. Here, v_u (v_d) is the vacuum expectation value of the Higgs field which couples exclusively to up-type (down-type) quarks and leptons. It should be noted that $v_u^2 + v_d^2 = (246 \text{ GeV})^2$ is fixed by the W mass and the Fermi coupling constant, while the ratio of two Higgs vacuum expectation values $\tan \beta = v_u/v_d$ is a free parameter of the model.

The total number of degrees of freedom of the MSSM is quite large primarily due to the parameters of the soft-supersymmetry-breaking sector. However, not all these parameters are physical. Some of the MSSM parame-

ters can be eliminated by expressing interaction eigenstates in terms of the mass eigenstates, with an appropriate redefinition of the MSSM fields to remove unphysical degrees of freedom. The MSSM possesses one hundred and twenty-four independent parameters. If the nineteen parameters of the Standard model are excluded, one hundred and five parameters are genuinely new parameters. The latter include:

- five real parameters and three CP-violating phases in the gaugino/higgsino sector
- twenty-one squark and slepton masses
- thirty-six new real mixing angles to define the squark and slepton mass eigenstates
- forty new CP-violating phases that can appear in squark and slepton interactions

Table 2.1 lists particles predicted by the MSSM. The superpartners of the right-handed and left-handed fermions are no longer mass eigenstates. They are mixed to generate mass eigenstates. The mass eigenstate superpartners of the charged bosons are the charginos ($\tilde{\chi}_i^\pm$, $i = 1, 2$) which are the result of mixing between wino (\tilde{W}^\pm) and charged higgsino (\tilde{H}^\pm). The mass eigenstate superpartners of the neutral bosons are the neutralinos ($\tilde{\chi}_i^0$, $i = 1, 2, 3, 4$) which are the result of mixing among neutral higgsinos (\tilde{H}_i^0 , $i = 1, 2$), zino (\tilde{Z}) and photino ($\tilde{\gamma}$).

Standard Model particles	Supersymmetric states	
	Interaction eigenstates	Mass eigenstates
Quarks (spin-1/2)	Squarks (spin-0)	
$\begin{pmatrix} u \\ d \end{pmatrix}_L, u_R, d_R$ $\begin{pmatrix} c \\ s \end{pmatrix}_L, c_R, s_R$ $\begin{pmatrix} t \\ b \end{pmatrix}_L, t_R, b_R$	$\begin{pmatrix} \tilde{u} \\ \tilde{d} \end{pmatrix}_L, \tilde{u}_R, \tilde{d}_R$ $\begin{pmatrix} \tilde{c} \\ \tilde{s} \end{pmatrix}_L, \tilde{c}_R, \tilde{s}_R$ $\begin{pmatrix} \tilde{t} \\ \tilde{b} \end{pmatrix}_L, \tilde{t}_R, \tilde{b}_R$	$\tilde{q}_{1,2}$
Leptons (spin-1/2)	Sleptons (spin-0)	
$\begin{pmatrix} \nu_e \\ e \end{pmatrix}_L, e_R$ $\begin{pmatrix} \nu_\mu \\ \mu \end{pmatrix}_L, \mu_R$ $\begin{pmatrix} \nu_\tau \\ \tau \end{pmatrix}_L, \tau_R$	$\begin{pmatrix} \tilde{\nu}_e \\ \tilde{e} \end{pmatrix}_L, \tilde{e}_R$ $\begin{pmatrix} \tilde{\nu}_\mu \\ \tilde{\mu} \end{pmatrix}_L, \tilde{\mu}_R$ $\begin{pmatrix} \tilde{\nu}_\tau \\ \tilde{\tau} \end{pmatrix}_L, \tilde{\tau}_R$	$\tilde{\ell}_{1,2}, \tilde{\nu}_{1,2}$
Gauge bosons & Higgs bosons	Gauginos & Higgsinos	Neutralinos & Charginos
γ (spin-1) Z^0 (spin-1) W^\pm (spin-1) g (spin-1) G (spin-2) h, H^0, A, H^\pm (spin-0)	Photino: $\tilde{\gamma}$ (spin-1/2) Zino: \tilde{Z} (spin-1/2) Wino: \tilde{W}^\pm (spin-1/2) Gluino: \tilde{g} (spin-1/2) Gravitino: \tilde{G} (spin-3/2) Higgsinos: $\tilde{H}_{1,2}^0, \tilde{H}^\pm$ (spin-1/2)	$\tilde{\chi}_{1,2,3,4}^0$ $\{\tilde{\gamma}, \tilde{Z}, \tilde{H}_{1,2}^0\}$ $\tilde{\chi}_{1,2}^\pm$ $\{\tilde{W}^\pm, \tilde{H}^\pm\}$

Table 2.1: Supersymmetric states

2.2 R-parity (R_p)

R -parity is a new discrete multiplicative quantum number defined as

$$R_P \equiv (-1)^{3B+L+2S} \quad (2.1)$$

for a particle of spin S , where B and L are baryon and lepton numbers. R -parity distinguishes SM particles from their superpartners: SM particles have even R -parity ($R_P = +1$) and their superpartners have odd R -parity ($R_P = -1$). R -parity Conservation (RPC) is imposed on the couplings so that the MSSM conserves both B and L . RPC implies that superpartners are always produced in pairs and decay through cascades to SM particles and the Lightest Supersymmetric Particle (LSP). Also SM particles and their superpartners do not mix each other. The LSP is expected to be stable and to escape detection due to its weakly interacting nature. Therefore, the characteristic signature of the process is appreciable missing energy. Cosmological arguments require the LSP to be colourless and electrically neutral. Then, the only possible candidates are the lightest neutralino, sneutrino and gravitino. The lightest neutralino ($\tilde{\chi}_1^0$) is often treated as the LSP in RPC models. It is necessary to decide which will be the LSP in RPC models, since all the others will decay into it. It is also technically possible to construct a theory where the LSP is not absolutely stable.

The LSP behaves differently from baryons. Because their interactions are typically electroweak with low energy cross sections in the 10^{-38} cm^2 range, they would not undergo nuclear reactions and form luminous stars. They would have normal gravitational interactions so they would concentrate near galaxies. But because their interactions are so weak they would not lose energy easily, they would be spread out in spherical halos. They therefore could constitute

cold dark matter. It is exciting that in recent years astronomers have found evidence from the behavior of galaxies contain several times more matter than the amount we can see in the form of stars. Such matter must be a new form of weakly interacting particle, and that is a possible interpretation of the data. In addition, if it is believed that the universe is flat and just closed, considerable matter is required that cannot be in the form of baryons. Therefore, the dark matter is one of the strong motivation for supersymmetric theory.

RPC was introduced to conserve B and L as global symmetry, otherwise R -parity Violation (RPV, \mathcal{R}_p) [16, 17] is allowed by supersymmetric theory and gauge invariance. Indeed, RPC is arbitrary and there is no *a priori* motivation for it. Viable RPV models which are compatible with existing experimental constraints can be constructed. RPV couplings affect SUSY phenomenology: (1) B or L violating processes such as the production of single superpartners and the direct decay of superpartners to SM particles are allowed. (2) The LSP is not stable any longer and might decay to SM particles within a detector. Consequently the experimental signatures differ very much from the large missing energy signatures of RPC models. (3) Because the LSP is unstable, it can be charged or colored. It can not explain cold dark matter.

In RPV Models, the superpotential could be given by

$$W = W_{MSSM} + W_{\mathcal{R}_p}, \quad (2.2)$$

where W_{MSSM} is the superpotential term of the MSSM which conserves R -parity and $W_{\mathcal{R}_p}$ is the superpotential term which violates it. W_{MSSM} is given by

$$W_{MSSM} = \epsilon_{ij} \mu \hat{H}_u^i \hat{H}_d^j + \epsilon_{ij} \left[\lambda_L \hat{H}_u^i \hat{L}^j \hat{E}^c + \lambda_D \hat{H}_u^i \hat{Q}^j \hat{D}^c + \lambda_U \hat{H}_d^i \hat{Q}^j \hat{U}^c \right], \quad (2.3)$$

where i and j are the SU(2) indices; μ is the Higgs mass parameter; and $\hat{H}_{u(d)}$

stands for the Higgs doublet; \hat{L} and \hat{Q} are the left-handed doublets of leptons and quarks, while \hat{E}^c , \hat{D}^c and \hat{U}^c are the right-handed singlets of charged leptons, down-type and up-type quarks, respectively. The λ parameters could be matrices which mix the interaction of the three generations.

$W_{\mathcal{R}_p}$ consists of two-types of R -parity violating terms. One includes the explicit R -parity violation resulting from the Trilinear RPV (TRPV) couplings and the other includes the spontaneous R -parity violation resulting from the Bilinear RPV (BRPV) couplings. In other words, $W_{\mathcal{R}_p}$ is written by

$$W_{\mathcal{R}_p} = W_{TRPV} + W_{BRPV} \quad (2.4)$$

where W_{TRPV} and W_{BRPV} represent the superpotentials for the trilinear and bilinear \mathcal{R}_p couplings, respectively. W_{TRPV} is given by

$$W_{TRPV} = \varepsilon_{ij} \left[\lambda_{ijk} \hat{L}^i \hat{L}^j \hat{E}^{ck} + \lambda'_{ijk} \hat{L}^i \hat{Q}^j \hat{D}^{ck} + \lambda''_{ijk} \hat{U}^{ci} \hat{D}^{cj} \hat{D}^{ck} \right], \quad (2.5)$$

and W_{BRPV} is given by

$$W_{BRPV} = \varepsilon_{ij} \epsilon_i \hat{L}^i \hat{H}_d^j. \quad (2.6)$$

In the TRPV framework [18], L violation is induced by the λ_{ijk} and λ'_{ijk} terms, while B violation is induced by the λ''_{ijk} terms. The λ_{ijk} are non-vanishing if $i < j$ so that at least two different generations are coupled in the purely leptonic vertices. The λ_{ijk} is antisymmetric under the interchange of the first two indices. The λ'_{ijk} are non-vanishing for $j < k$. The λ''_{ijk} is antisymmetric under the interchange of the last two indices. There are nine λ couplings for the triple lepton vertices, twenty-seven λ' couplings for the lepton-quark-quark vertices and nine λ'' couplings for the triple quark vertices. Therefore, the TRPV involves forty-five new free parameters in total. The simultaneous presence of the last two terms leads to rapid squark-mediated

proton decay at tree level and the solution of this problem is not unique. A number of RPV models predict only a subset of the terms in the formula, thus protecting the proton decay. When the analysis results are translated into limits, it is also assumed that the couplings are significant for only one choice of i, j and k . The derived limits correspond to the most conservative choice of the coupling. Another solution of this problem is to exclude all terms by imposing RPC. The interactions corresponding to the W_{TRPV} are assumed to respect the gauge symmetry $SU(3)_C \times SU(2)_L \times U(1)_Y$ of the SM.

The pair-production and decay via TRPV couplings of scalar fermions are summarized in Table 2.2 with final state topologies. Even though Table 2.2 shows only the pair-production of different scalar fermions, superpartners can also be singly produced since pair-production is not required in RPV models. The particles resulting from the neutralino decay are put in parentheses. Often the scalar particle decay modes are classified according to their topologies: all decays toward the LSP, the neutralino, via a gauge interaction with subsequent decay of the LSP via an RPV interaction are referred to as “indirect decay” modes. The others correspond to “direct decay” modes to SM particles via an RPV interaction.

In the BRPV framework [19], the R -parity is spontaneously broken through the Vacuum Expectation Values (VEV) of the right-handed sneutrinos $\langle \bar{\nu}^c \rangle = v_R \neq 0$. The ϵ_i parameters violate L in the i -th generation. The ϵ_3 induces a nonzero VEV of the left-handed tau neutrinos $\langle \bar{\nu}_\tau \rangle = v_3/\sqrt{2}$ and violates tau-lepton number. v_3 contributes to the W mass according to $M_W^2 = \frac{1}{4}g^2(v_u^2 + v_d^2 + v_3^2)$. In this framework, charginos mix with charged leptons, neutralinos mix with neutrinos and charged sleptons mix with charged Higgs bosons.

<i>Pair-production and decay of scalar fermions</i>	<i>Coupling</i>	<i>Topology</i>
$\tilde{\ell}^+ \tilde{\ell}^- \rightarrow \nu \ell \nu \ell$	λ	$2\ell + \cancel{E}_T$
$\tilde{\nu} \tilde{\nu} \rightarrow \nu \tilde{\chi}_1^0 \nu \tilde{\chi}_1^0 \rightarrow \nu(\nu \ell^+ \ell^-) \nu(\nu \ell^+ \ell^-)$	λ	$4\ell + \cancel{E}_T$
$\tilde{\nu} \tilde{\nu} \rightarrow \ell^+ \ell^- \ell^+ \ell^-$	λ	4ℓ
$\tilde{\ell}^+ \tilde{\ell}^- \rightarrow \ell^+ \tilde{\chi}_1^0 \ell^- \tilde{\chi}_1^0 \rightarrow \ell^+(\nu \ell^+ \ell^-) \ell^-(\nu \ell^+ \ell^-)$	λ	$6\ell + \cancel{E}_T$
$\tilde{t}_1 \tilde{t}_1 \rightarrow e^+ q e^- q$	λ'	$2e + 2 \text{ jets}$
$\tilde{t}_1 \tilde{t}_1 \rightarrow \mu^+ q \mu^- q$	λ'	$2\mu + 2 \text{ jets}$
$\tilde{t}_1 \tilde{t}_1 \rightarrow \tau^+ q \tau^- q$	λ'	$2\tau + 2 \text{ jets}$
$\tilde{\tau}^+ \tilde{\tau}^- \rightarrow \tau^+ \tilde{\chi}_1^0 \tau^- \tilde{\chi}_1^0 \rightarrow \tau^+(\ell q q) \tau^-(\ell q q)$	λ'	$\tau + \text{jets}$
$\tilde{\tau}^+ \tilde{\tau}^- \rightarrow \tau^+ \tilde{\chi}_1^0 \tau^- \tilde{\chi}_1^0 \rightarrow \tau^+(\nu q q) \tau^-(\ell q q)$	λ'	$\tau + \text{jets}$
$\tilde{\tau}^+ \tilde{\tau}^- \rightarrow \tau^+ \tilde{\chi}_1^0 \tau^- \tilde{\chi}_1^0 \rightarrow \tau^+(\nu q q) \tau^-(\nu q q)$	λ'	$\tau + \text{jets}$
$\tilde{\ell}^+ \tilde{\ell}^- \rightarrow \ell^+ \tilde{\chi}_1^0 \ell^- \tilde{\chi}_1^0 \rightarrow \ell^+(\ell q q) \ell^-(\ell q q)$	λ'	$\ell + \text{jets}$
$\tilde{\ell}^+ \tilde{\ell}^- \rightarrow \ell^+ \tilde{\chi}_1^0 \ell^- \tilde{\chi}_1^0 \rightarrow \ell^+(\nu q q) \ell^-(\ell q q)$	λ'	$\ell + \text{jets}$
$\tilde{\ell}^+ \tilde{\ell}^- \rightarrow \ell^+ \tilde{\chi}_1^0 \ell^- \tilde{\chi}_1^0 \rightarrow \ell^+(\nu q q) \ell^-(\nu q q)$	λ'	$\ell + \text{jets}$
$\tilde{\nu} \tilde{\nu} \rightarrow \nu \tilde{\chi}_1^0 \nu \tilde{\chi}_1^0 \rightarrow \nu(\nu q q) \nu(\nu q q)$	λ'	$4 \text{ jets} + \cancel{E}_T$
$\tilde{\nu} \tilde{\nu} \rightarrow q q q q$	λ'	4 jets
$\tilde{\ell}^+ \tilde{\ell}^- \rightarrow q q q q$	λ'	4 jets
$\tilde{q} \tilde{q} \rightarrow q q q q$	λ''	4 jets

Table 2.2: List of pair-production and decay mechanism of different scalar fermions including the couplings and corresponding topologies [30, 31]

RPV models have recently attracted considerable theoretical and phenomenological interest. The branching ratios of some of the RPV decay modes can be comparable or even larger than RPC modes. For example, this could be the case for the scalar top quark decay modes to the third generation fermions.

Chapter 3

Pair-production of Scalar Top Quarks Decaying via R-parity Violation in $p\bar{p}$ Collisions

In this chapter, the basic concepts and main idea of the analysis – Search for Pair-production of Scalar Top Quarks Decaying via R -parity Violation in $p\bar{p}$ Collisions at $\sqrt{s} = 1.8$ TeV – are outlined in detail. Section 3.1 explains the reasons why scalar top quark searches are so interesting in supersymmetry search. Section 3.2 shows the pair-production cross section of scalar top quarks at the Tevatron. Section 3.3 describes the decays of scalar top quarks via \mathcal{R}_p couplings and the most recent and competing results from similar searches. Section 3.4 shows the strategy of this analysis. In the case of no discovery, it explains our technique to determine the mass limit of scalar top quark.

3.1 Scalar Top Quark

Scalar top (“stop,” \tilde{t}) quark physics is a very interesting part of SUSY phenomenology, since the lightest scalar top quark might be the lightest charged SUSY particle and potentially lighter than the top quark due to the following two reasons: (1) The large top Yukawa coupling leads to reduced soft SUSY breaking masses compared to the first two generation in GUT models, and (2) The off-diagonal elements of scalar top quark mass matrix are proportional to the top quark mass leading to a strong mixing and a large mass splitting between the mass eigenstates \tilde{t}_1 and \tilde{t}_2 ($M_{\tilde{t}_1} < M_{\tilde{t}_2}$).

The mass matrix \mathcal{M} of the scalar top quark is

$$\mathcal{M}_{\tilde{t}}^2 = \begin{pmatrix} M_{\tilde{t}_L}^2 + M_t^2 + M_Z^2 \cos 2\beta(\frac{1}{2} - \frac{2}{3} \sin^2 \theta_W) & M_t (A_t - \mu \cot \beta) \\ M_t (A_t - \mu \cot \beta) & M_{\tilde{t}_R}^2 + M_t^2 + M_Z^2 \cos 2\beta(\frac{2}{3} \sin^2 \theta_W) \end{pmatrix}, \quad (3.1)$$

where the angle θ_W is the weak mixing angle (or Weinberg angle). The mass matrix eigenvalues are

$$\begin{aligned} M_{\tilde{t}_{1,2}}^2 &= \frac{1}{2} (M_{\tilde{t}_L}^2 + M_{\tilde{t}_R}^2) + \frac{1}{4} M_Z^2 \cos 2\beta + M_t^2 \\ &\pm ([\frac{1}{2} (M_{\tilde{t}_L}^2 - M_{\tilde{t}_R}^2) + M_Z^2 \cos 2\beta(\frac{1}{4} - \frac{2}{3} \sin^2 \theta_W)]^2 + M_t^2 (A_t - \mu \cot \beta)^2)^{1/2}. \end{aligned} \quad (3.2)$$

The mass eigenstates are

$$\begin{aligned} \tilde{t}_1 &= \tilde{t}_L \cos \theta_{LR} - \tilde{t}_R \sin \theta_{LR}, \\ \tilde{t}_2 &= \tilde{t}_L \sin \theta_{LR} + \tilde{t}_R \cos \theta_{LR}, \end{aligned} \quad (3.3)$$

where the angle θ_{LR} is a new real mixing angle to relate the scalar top quark mass eigenstates to the interaction eigenstates.

3.2 Pair-production Cross Section

At the Tevatron, scalar top quarks are pair-produced via gg fusion and $q\bar{q}$ annihilation. These are RPC processes. Figure 3.1 shows the dominant $\tilde{t}_1\bar{\tilde{t}}_1$ production mechanism at the Tevatron. Figure 3.2 shows the pair-production cross section of the lightest scalar top quarks at the Tevatron calculated in the Leading Order (LO) and Next-to-Leading Order (NLO) using PROSPINO¹ program with CTEQ4L and CTEQ4M Parton Distribution Functions (PDF), respectively [20, 21, 22, 53]. We provide input parameters for the program such as masses of the squarks, gluino and top quark: 500, 284 and 175 GeV/ c^2 . The values of the input parameters are identical to those used for signal Monte Carlo generation. The default scale for renormalization and factorization is $M_{\tilde{t}_1}$ and theoretical uncertainty due to the scale has been estimated by moving the scale by a factor of two up and down.

3.3 Decays via R-parity Violating Couplings

This analysis assumes that the lightest scalar top quarks are pair-produced by a RPC coupling in $p\bar{p}$ collisions at $\sqrt{s} = 1.8$ TeV; and, each scalar top quark decays into a tau lepton and a bottom quark via nonzero λ'_{333} [23, 24, 25] and ϵ_3 couplings:

$$\tilde{t}_1 \rightarrow \tau + b \quad (\text{Channel 1})$$

The branching ratio of this channel will be 100 % in both TRPV and BRPV frameworks, if the scalar top quark is the LSP. If the LSP is the lightest

¹A program for the **PRO**duction of Supersymmetric Particles In Next-to-leading Order QCD

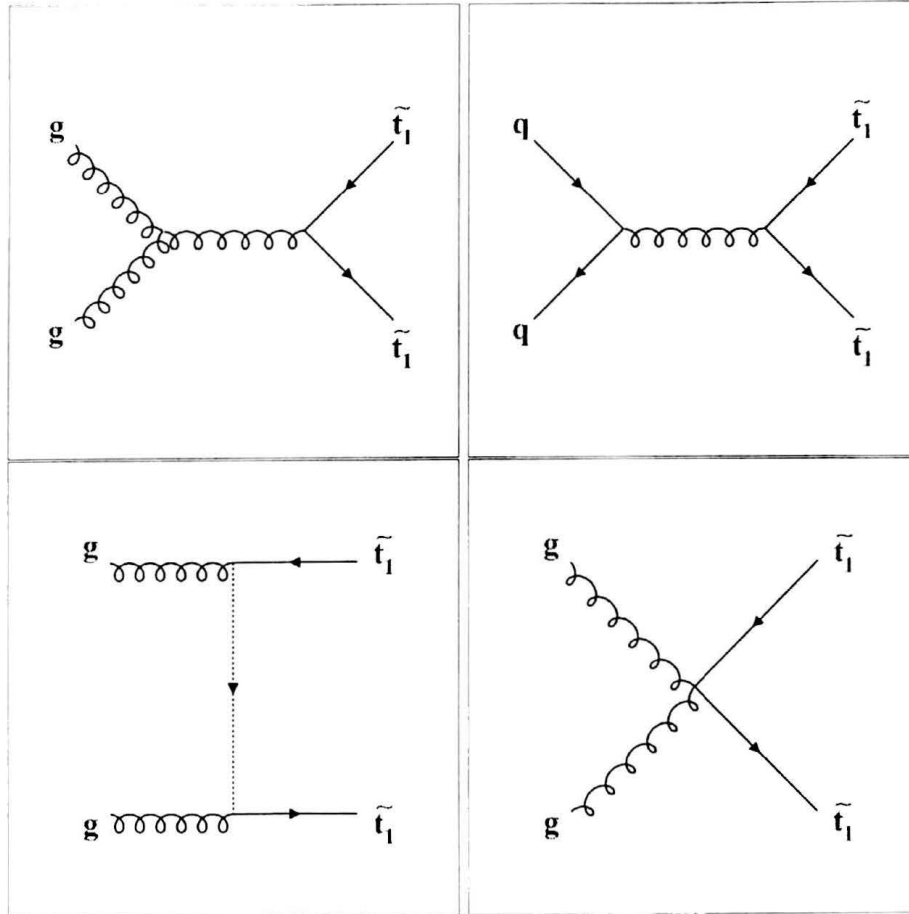


Figure 3.1: Feynman diagrams for the dominant $\tilde{t}_1 \tilde{t}_1^*$ production mechanisms at the Tevatron

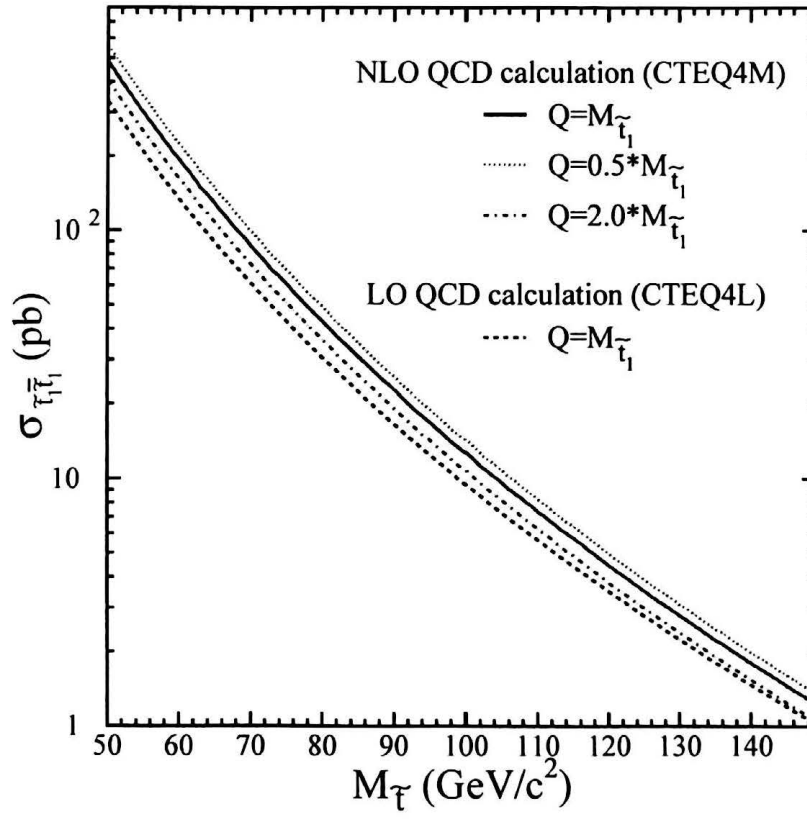


Figure 3.2: The pair-production cross section of the lightest scalar top quarks at the Tevatron

$M_{\tilde{t}_1}$ (GeV/ c^2)	σ_{LO} (pb)	σ_{NLO} (pb)
60	134.10	193.20
70	61.09	86.51
80	30.52	42.84
90	16.45	22.50
100	9.38	12.63
110	5.63	7.33
120	3.50	4.45
130	2.25	2.80
140	1.47	1.81

Table 3.1: The pair-production cross section of the lightest scalar top quarks at the Tevatron from the LO and NLO QCD calculations. The renormalization and factorization scales used in the calculation are $Q = M_{\tilde{t}_1}$.

neutralino with the Next Lightest Supersymmetric Particle (NLSP) being the scalar top quark, the scalar top quark can decay into χ_1^0 and a charm quark via the following R -parity conserving process:

$$\bar{t}_1 \rightarrow \chi_1^0 + c \quad (\text{Channel 2})$$

However, if $|\epsilon_3|$ and $|v_3|$ are below a GeV, it is possible that the decay mode of the scalar top quark shown in Channel 1 is dominant in the BRPV even when the LSP is χ_1^0 . Therefore, the Channel 1 is important for a signature of the R -parity violation. However, one more assumption is required to validate our analysis: those couplings should be strong enough for the scalar top quarks to decay promptly inside our detector.

The experimental signature is two tau leptons and two b quark jets. This topology is identical to that of the CDF third-generation leptoquark (LQ_3) search. When the direct decays of scalar quarks are dominant, the signature is identical to leptoquark production [26].

Events are inclusively selected by requiring at least a central muon (μ) from $\tau \rightarrow \mu\nu_\mu\nu_\tau$, a hadronically decaying tau (τ_h) lepton and two jets. The muon is our trigger particle. The tau branching ratio to a muon and neutrinos is approximately 18% and to hadrons is approximately 64% (“1-prong”: 50%, “3-prong”: 14%) [6]. It is possible that one of taus decays into an electron and neutrinos and the other tau decays hadronically. An analysis in CDF using electron as trigger particle instead of muon has been performed concurrently with this analysis [27]. In both analyses, it is not necessary to require b-tag for any of jets with current luminosity. No candidate events are observed after the requirement of two or more jets. We combine two results to set a complete limit in Chapter 8 [29].

$$p\bar{p} \rightarrow \tilde{t}_1 \bar{\tilde{t}}_1 + X \rightarrow (\tau^+ b) (\tau^- \bar{b}) + X \rightarrow \mu \text{ (or } e) \tau_h b \bar{b} + X$$

Table 3.2: Experimental signature for candidate event selection

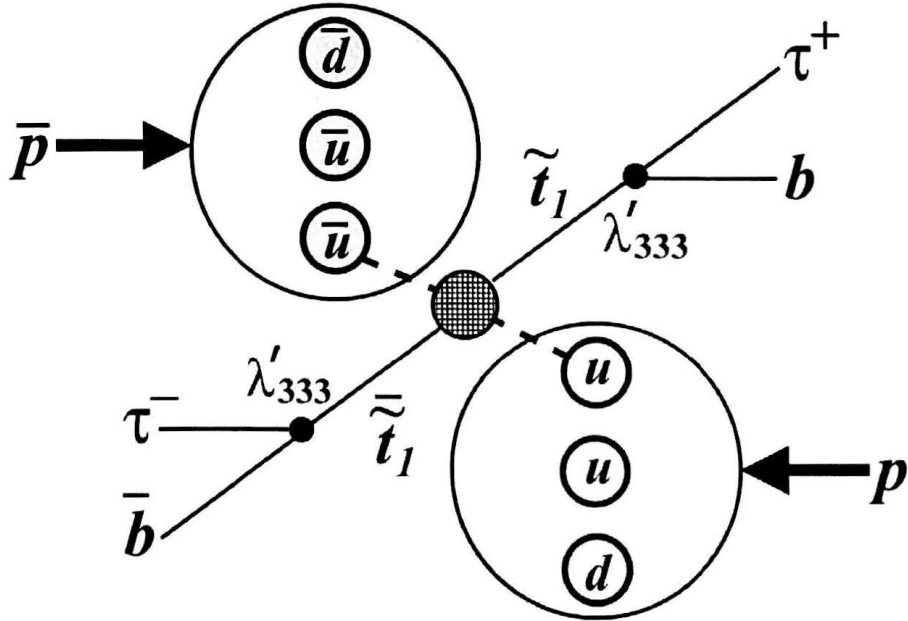


Figure 3.3: Experimental signature

Collaborations at LEP have published similar searches. The OPAL Collaboration has accomplished the searches on the basis of an integrated luminosity of 56 pb^{-1} gathered at $\sqrt{s} = 183 \text{ GeV}$ in the middle of the LEP2 period, in 1997. For the case of scalar top quark searches in LEP, the mass limit depends on the value of the mixing angle in the scalar top quark sector, θ_{LR} in Equation 3.3, which controls the coupling of the scalar top quark to the Z boson. This coupling is largest for a pure left-handed scalar top quark with “null mixing angle” and vanishes for a value of the mixing angle close to 0.98 radians, the “full mixing angle.” They set a 95% C.L. lower limit of the scalar top quark mass at $81 \text{ GeV}/c^2$ for null mixing angle and $73 \text{ GeV}/c^2$ for full mixing angle with two tau leptons plus two jet topology under the assumption of significant λ'_{33k} ($k = 1, 2, 3$). Figure 3.4 shows the Feynman diagrams of those decays [30]. The most recent and competing results on the lower limit of the scalar top quark mass with same signature come from ALEPH experiment. They use 410 pb^{-1} of data collected in 1998 – 1999 at $\sqrt{s} = 189 - 202 \text{ GeV}$. They set a 95% C.L. lower limit of the pure left-handed scalar top quark mass at $93 \text{ GeV}/c^2$ with $e^+e^- \rightarrow \tilde{t}_1 \bar{\tilde{t}}_1 \rightarrow \tau^+\tau^- + 2 \text{ jet}$ topology under the assumption of non-negligible λ'_{33k} ($k = 1, 2, 3$) couplings [31].

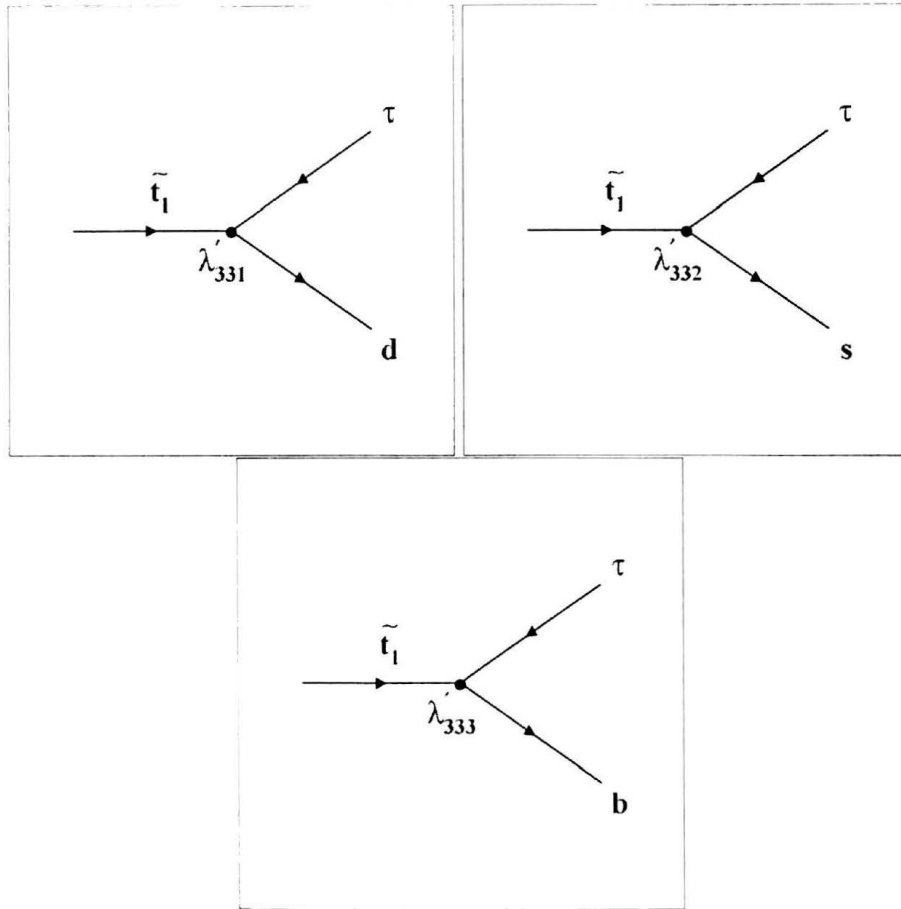


Figure 3.4: Feynman diagrams of the scalar top quark decays via \mathcal{R}_p λ'_{33k} couplings, where $k = 1, 2, 3$

3.4 Technique to Determine Mass Limit of Scalar Top Quark

We have taken known effects such as trigger, muon identification and muon isolation efficiencies into account for Monte Carlo (MC) corrections, and they are well known on the basis of several studies in CDF [32, 33, 34, 35, 36, 37, 39, 38]. It will be described more in Section 5.3. However, the tau identification efficiency and the geometrical acceptance of tau are not so well known and are difficult to estimate. To get around this difficulty, we “calibrate” our simulation by tuning a related process to match the data. We use $Z \rightarrow \tau\tau$ which is the same as scalar top quark signature except for two b quark jets. There are also some kinematic differences. Using this method, we can estimate and reduce unknown effects related with muons and hadronic taus. Therefore, we simultaneously study $Z \rightarrow \tau\tau$ and $\tilde{t}_1\tilde{t}_1^* \rightarrow \tau^+\tau^-b\bar{b}$ processes, and reduce or cancel some of our systematic uncertainties.

Here is the method. We assume that one of two taus decays leptonically to a muon and neutrinos and the other decays hadronically to pions. First, we constitute “baseline samples” based on the events including a muon and a hadronic tau: $\mu + \tau_h$ pair. These samples are prerequisite for the two analyses, since both processes include two taus and the taus will be identified in the same way. We lower thresholds for object selection as much as we can to increase signal acceptance considering the fact that the muon from $\tau \rightarrow \mu\nu_\mu\nu_\tau$ has relatively lower p_T . We keep both Opposite Sign (OS) and Like Sign (LS) $\mu + \tau_h$ pairs in our baseline samples. The signal $\mu + \tau_h$ pairs always have OS. We use the LS samples to estimate QCD backgrounds. This will be explained more in Section 5.1. Second, we separately devise additional cuts to reject major

backgrounds and ensure the purity of samples in both analyses, which will be explained in detail in Sections 6.3 and 6.4. Third, we estimate acceptances and select candidate events in the data for both processes. Finally, we obtain the production cross section of $\tilde{t}_1\bar{\tilde{t}}_1$ through the calibration with $Z \rightarrow \tau\tau$ events.

The “master” formula is introduced here. The number of Z events expected from the simulation including the correction factor for hadronic tau is:

$$\begin{aligned} N_Z^{MC} &= N_Z^{obs} - N_Z^{BG} \\ &= \sigma_Z \cdot B(Z \rightarrow \tau\tau) \cdot \int \mathcal{L} dt \cdot \underbrace{B(\tau\tau \rightarrow \mu + \text{hadrons} + X)}_{B_{\mu\tau_h}} \cdot A_Z \end{aligned} \quad (3.4)$$

where, N_Z^{obs} , N_Z^{BG} and N_Z^{MC} are the numbers of candidates from the data, expected backgrounds and expected signals, respectively. σ_Z represents the inclusive production cross section of Z bosons. $B(Z \rightarrow \tau\tau)$ stands for the branching ratio of $Z \rightarrow \tau\tau$. $\int \mathcal{L} dt$ refers to the integrated luminosity. $B_{\mu\tau_h}$ is the branching ratio of tau decays, which is calculated as follows:

$$\begin{aligned} B_{\mu\tau_h} &= 2 \times B(\tau \rightarrow \mu\nu\bar{\nu}) \cdot B(\tau \rightarrow \text{hadrons} + \nu) \\ &\simeq 2 \times 0.18 \times 0.64 = 0.23 . \end{aligned} \quad (3.5)$$

A_Z is the acceptance for $Z \rightarrow \tau\tau$ events and written as follows:

$$A_Z = A_Z^{MC} \cdot \epsilon_Z^{trg} \cdot f^\mu \cdot f^{\tau_h} , \quad (3.6)$$

where A_Z^{MC} is the MC acceptance for $Z \rightarrow \tau\tau$ calculated on the basis of event counting and ϵ_Z^{trg} is the trigger efficiency. $f^\mu \equiv f_{unknown}^\mu \cdot f_{ID}^\mu \cdot f_{ISO}^\mu$ and f^{τ_h} are the MC correction factors for muon and hadronic tau, where f_{ID}^μ and f_{ISO}^μ correct the identification and isolation efficiencies of muon. A factor, $f_{unknown}^\mu$, can be assumed to correct all unknown effects related with muon. See

3.4 Technique to Determine Mass Limit of Scalar Top Quark 33

Section 5.3 for f_{TD}^μ and f_{ISO}^μ . Therefore, the correction factor to MC events for variables whose effects are unknown can be determined as:

$$f_{unknown}^\mu \cdot f^\tau = \frac{N_Z^{MC}}{\sigma_Z \cdot B(Z \rightarrow \tau\tau) \cdot \int \mathcal{L} dt \cdot B_{\mu\tau_h} \cdot A_Z^{MC} \cdot f_{TD}^\mu \cdot f_{ISO}^\mu} \quad (3.7)$$

The signature of $\tilde{t}_1 \bar{\tilde{t}}_1$ is a muon, a hadronic tau and two jets. Therefore, we expect the difference between the data and simulated efficiencies for the $\tilde{t}_1 \bar{\tilde{t}}_1$ analysis will be similar to $Z \rightarrow \tau\tau$. We need to include the correction factor for hadronic tau for the acceptance estimation. Assuming f^μ and f^{τ_h} for $\tilde{t}_1 \bar{\tilde{t}}_1$ are the same values as those for $Z \rightarrow \tau\tau$, the number of events expected from MC for $\tilde{t}_1 \bar{\tilde{t}}_1$ is written as follows:

$$\begin{aligned} N_{\tilde{t}_1 \bar{\tilde{t}}_1}^{MC} &= N_{\tilde{t}_1 \bar{\tilde{t}}_1}^{obs} - N_{\tilde{t}_1 \bar{\tilde{t}}_1}^{BG} \\ &= \sigma_{\tilde{t}_1 \bar{\tilde{t}}_1} \cdot (B(\tilde{t}_1 \rightarrow \tau^+ b))^2 \cdot \int \mathcal{L} dt \cdot B_{\mu\tau_h} \cdot A_{\tilde{t}_1 \bar{\tilde{t}}_1} \\ &= \sigma_{\tilde{t}_1 \bar{\tilde{t}}_1} \cdot (B(\tilde{t}_1 \rightarrow \tau^+ b))^2 \cdot \int \mathcal{L} dt \cdot B_{\mu\tau_h} \cdot A_{\tilde{t}_1 \bar{\tilde{t}}_1}^{MC} \cdot \epsilon_{\tilde{t}_1 \bar{\tilde{t}}_1}^{trg} \cdot f^\mu \cdot f^{\tau_h} \quad (3.8) \end{aligned}$$

where, $N_{\tilde{t}_1 \bar{\tilde{t}}_1}^{obs}$, $N_{\tilde{t}_1 \bar{\tilde{t}}_1}^{BG}$ and $N_{\tilde{t}_1 \bar{\tilde{t}}_1}^{MC}$ are the numbers of candidates from the data, expected backgrounds and expected signals for $\tilde{t}_1 \bar{\tilde{t}}_1$ production, respectively. $\sigma_{\tilde{t}_1 \bar{\tilde{t}}_1}$ is the production cross section of $\tilde{t}_1 \bar{\tilde{t}}_1$. $(B(\tilde{t}_1 \rightarrow \tau^+ b))^2$ represents the branching ratio of $\tilde{t}_1 \bar{\tilde{t}}_1 \rightarrow \tau^+ \tau^- b \bar{b}$. $A_{\tilde{t}_1 \bar{\tilde{t}}_1}$ is the acceptance for $\tilde{t}_1 \bar{\tilde{t}}_1 \rightarrow \tau^+ \tau^- b \bar{b}$, while $A_{\tilde{t}_1 \bar{\tilde{t}}_1}^{MC}$ denotes the MC acceptance for $\tilde{t}_1 \bar{\tilde{t}}_1 \rightarrow \tau^+ \tau^- b \bar{b}$ calculated on the basis of event counting. $\epsilon_{\tilde{t}_1 \bar{\tilde{t}}_1}^{trg}$ is the trigger efficiency. Therefore, the pair-production cross section of the lightest scalar top quark can be determined by the combination of Equations (3.4) and (3.8) as follows:

$$\sigma_{\tilde{t}_1 \bar{\tilde{t}}_1} \cdot (B(\tilde{t}_1 \rightarrow \tau^+ b))^2 = \frac{N_{\tilde{t}_1 \bar{\tilde{t}}_1}^{obs} - N_{\tilde{t}_1 \bar{\tilde{t}}_1}^{BG}}{\int \mathcal{L} dt \cdot B_{\mu\tau_h} \cdot A_{\tilde{t}_1 \bar{\tilde{t}}_1}}$$

$$\begin{aligned}
 &= \frac{N_{\tilde{t}_1\tilde{t}_1}^{obs} - N_{\tilde{t}_1\tilde{t}_1}^{BG}}{A_{\tilde{t}_1\tilde{t}_1}^{MC} \cdot \varepsilon_{\tilde{t}_1\tilde{t}_1}^{trg} \cdot \left(\frac{N_Z^{obs} - N_Z^{BG}}{\sigma_Z \cdot B(Z \rightarrow \tau\tau) \cdot A_Z^{MC} \cdot \varepsilon_Z^{trg}} \right)} \\
 &= \left(\frac{N_{\tilde{t}_1\tilde{t}_1}^{obs} - N_{\tilde{t}_1\tilde{t}_1}^{BG}}{N_Z^{obs} - N_Z^{BG}} \right) \cdot \left(\frac{A_Z^{MC} \cdot \varepsilon_Z^{trg}}{A_{\tilde{t}_1\tilde{t}_1}^{MC} \cdot \varepsilon_{\tilde{t}_1\tilde{t}_1}^{trg}} \right) \cdot \sigma_Z \cdot B(Z \rightarrow \tau\tau) \cdot R(0 - jet) \quad (3.9)
 \end{aligned}$$

The production cross section times branching ratio, $\sigma_Z \cdot B(Z \rightarrow \tau\tau)$, is taken from the CDF measurement of $Z \rightarrow e^+e^-$ [40]. However, we use only $Z(\rightarrow \tau\tau) + 0$ -jet events for calibration so we have to multiply the ratio of 0-jet events, $R(0 - jet)$, which is taken from the CDF measurement based on the $Z(\rightarrow ee) + \geq n$ -jet events [41] at the end. $R(0 - jet)$ is given as follows:

$$\begin{aligned}
 R(0 - jet) &= R(\geq 0 \text{ jet}) - R(\geq 1 \text{ jet}) \\
 &= 1 - \frac{\sigma_Z(\geq 1 \text{ jet})}{\sigma_Z(\geq 0 \text{ jet})} \\
 &= 0.8040 \pm 0.0065 \text{ (stat+sys)} \pm 0.0238 \text{ (Jet Def.)} \quad (3.10)
 \end{aligned}$$

We assume $\sigma \cdot B(Z \rightarrow ee) = \sigma \cdot B(Z \rightarrow \mu\mu) = \sigma \cdot B(Z \rightarrow \tau\tau)$ by lepton universality.

This method provides more merits. First, it cancels several parameters mentioned above: $\int \mathcal{L} dt$ and $B_{\mu\tau_h}$. Second, it reduces systematic uncertainties from muon and hadronic tau. The demerit of this method is to involve large uncertainty from the statistical error of $Z \rightarrow \tau\tau$ data. See Chapter 7, especially Section 7.2. In spite of various merits, this statistical component is quite crucial to the calculation of our limit. The limit is set in Section 8.2.

Chapter 4

The Experimental Apparatus

In quantum mechanics, particles have wave-like properties and the wavelength of a particle is inversely proportional to its momentum. As the momentum of a particle increases, its wavelength decreases. This is the reason why high-energy particle beams are required to probe small distances. The high-energy particle beams can be produced by particle accelerators. A “collider,” a special kind of accelerator configuration in which particle beams are directed at each other to produce head-on collisions, provides the most efficient mechanism for translating beam energy into collision energy. High-energy collisions generate a vast profusion of particles. To separate out the interesting events requires complex systems of detectors to trace the paths of the particles, using high-speed electronics to evaluate the events in real time. The processing power of the electronics used to untangle the data from the detectors compares with the capabilities of the fastest supercomputers. After reconstruction of events, each event can be interpreted in terms of the underlying physical processes involved. Therefore, accelerators and detectors are two important tools used in particle physics experiments [1].

The data used for this analysis were collected by the Collider Detector at Fermilab (CDF), while the collisions were produced by the Tevatron proton-antiproton ($p\bar{p}$) collider at Fermi National Accelerator Laboratory (Fermilab). At Fermilab, protons and antiprotons are accelerated to 900 GeV by a series of accelerators. The principal accelerator, called the “Tevatron,” is a synchrotron. A synchrotron is a circular accelerator that uses magnets to confine electrically charged particles in a circular path so that they experience the repeated acceleration by electric fields during each revolution. Because the recirculation circle is fixed in a synchrotron, the confining magnetic field should be increased in proportional to the beam energy. Thus, the maximum energy attainable in a synchrotron is limited by the maximum strength of the magnets. After all, the energy could be increased more in a synchrotron by applying electric fields over many revolutions, only when the product of the confining magnetic field and accelerator radius is big enough to keep the particle beam circulating at the highest energy. The Tevatron uses superconducting magnets and Radio Frequency (RF) cavities to accelerate protons and antiprotons close to the speed of light, and brings them into head-on collisions at $\sqrt{s} = 1.8$ TeV. The particles are accelerated by RF cavities in which a RF wave is injected. The part of this wave closest to the beam has an electric field aligned so that the charged particle gets a boost in the right direction at that time. At room temperature, the average proton energy is $\simeq \frac{1}{40}$ eV, significantly less than the final energy. Thus, the protons must be accelerated to roughly 0.99944 c. Inside of the Tevatron, protons and antiprotons travel in opposite directions. The collisions take place inside two collider detectors, the CDF and DØ detector, on the Tevatron ring. The CDF is general purpose solenoidal detector for the study of hadron collisions.

In Section 4.1, a brief description of particle acceleration at Fermilab is given [42]. In the following section, an overview on the CDF detector and its trigger system [43] is continued. The CDF detector has been described in detail elsewhere [44].

4.1 The Fermilab Accelerators

The acceleration of particles is accomplished by a series of accelerators: the Cockcroft-Walton Preaccelerator, Linac, Booster, Main Ring and Tevatron. The accelerators can be operated in fixed target and colliding beam modes. Figure 4.1 shows the general layout of the accelerators.

The beam of particles begin as negative hydrogen ions in the **Cockcroft-Walton Preaccelerator**. Inside this device, electrons are added to hydrogen atoms. The resulting negative ions, each consisting of two electrons and one proton, are accelerated to an energy of 750 keV.

The negative hydrogen ions enter a linear accelerator called the **Linac**. The Linac accelerates negative hydrogen ions from 750 keV to 400 MeV before injecting them into the Booster. The Linac consists of several tanks filled with small tubes, called “drift tubes,” spaced further and further apart. An electric field is applied to the tubes repeatedly reversing in direction. The particles travel through the drift tubes, hiding in them when the electric field is in a direction that would slow them down and emerging into the gaps between the drift tubes when the field is in the direction to speed them up. The total length of the Linac is approximately 150 m. Before entering the Booster, the negative hydrogen ions pass through a carbon foil which removes the electrons, leaving only the protons.

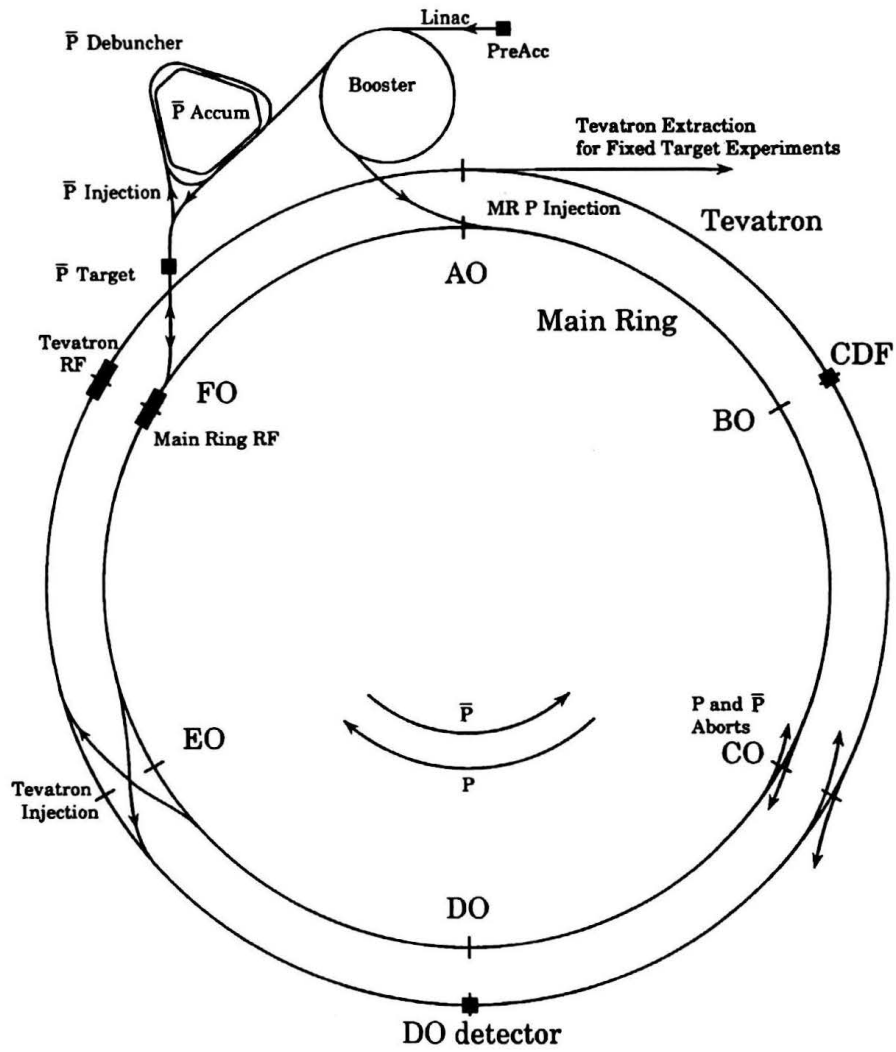


Figure 4.1: A schematic view of the Fermilab accelerators

The **Booster** is a synchrotron 475 m in circumference. The protons travel around the Booster about 20,000 times and are accelerated to 8 GeV through RF cavities. The Booster normally cycles twelve times in rapid succession, loading twelve pulses (or bunches of protons) into the Main Ring.

The **Main Ring**¹ is another synchrotron 6.3 km in circumference. A tunnel 3 m in diameter, buried 6 m underground, it houses 1,000 conventional, copper-coiled magnets which continuously bend and focus the protons. The Main Ring accelerates protons to 150 GeV.

The same tunnel that houses the Main Ring contains the 1,000 superconducting magnets which comprise the rapid cycling synchrotron known as the **Tevatron**² because of its ability to accelerate protons to nearly 1 TeV. The superconducting magnets form a ring directly below the Main Ring and operate in the temperature range of liquid helium (5.37 K). Superconducting magnets produce a larger magnetic field at a lower operating cost than conventional magnets. The Tevatron accelerates protons close to the speed of light. In fixed target mode, the proton beam is extracted and sent down the fixed target beamline to the experimental areas.

Some of the experiments at Fermilab are performed by colliding a beam of protons with a beam of antiprotons. To produce the antiprotons, the protons are first accelerated to an energy of 120 GeV in the Main Ring, then extracted, transported to a target area, and focused on target consisting of nickel. The collisions in the target produce a wide range of secondary particles

¹During the next run (Run II) which will start in early 2001, the Main Ring will be replaced by Main Injector (MI). See Appendix A

²The Tevatron is the highest-energy accelerator today and will remain so until the Large Hadron Collider (LHC) era. The discovery of the top quark at Fermilab demonstrates its power to explore physics and its capabilities will be considerably enhanced with the MI.

including many antiprotons. The antiprotons selected using a magnetic field are transported to the **Debuncher Ring** where their momentum spread is reduced by a process known as “stochastic cooling.” Subsequently, they are stored in the **Accumulator Ring**. When a sufficient number of antiprotons, typically 5×10^{11} , has been produced, they are reinjected into the Main Ring traveling in an opposite direction from the protons. Finally, they pass into the Tevatron where they are accelerated to 900 GeV simultaneously with a countercirculating beam of protons. The protons and antiprotons collide at a combined energy of 1.8 TeV inside two detectors named “CDF” and “DØ.”

When the Tevatron is operating in colliding beam mode, six bunches of protons collide with six bunches of antiprotons in the CDF detector. Each proton bunch contains about 2×10^{11} protons and travels clockwise along the ring. Each antiproton bunch contains about 6×10^{10} antiprotons and travels counter-clockwise. Special magnets called “low beta quadrupoles” focus the beam spot to about $60 \mu\text{m}$ across to increase the probability of a collision. These crossings occur every $3.5 \mu\text{s}$ to produce an instantaneous luminosity (\mathcal{L}) on the order of $10^{31} \text{ cm}^{-2}\text{s}^{-1}$, where \mathcal{L} is defined to be the interaction cross section (σ) times the number of particles (N). The longitudinal interaction region of the beam is about 30 cm.

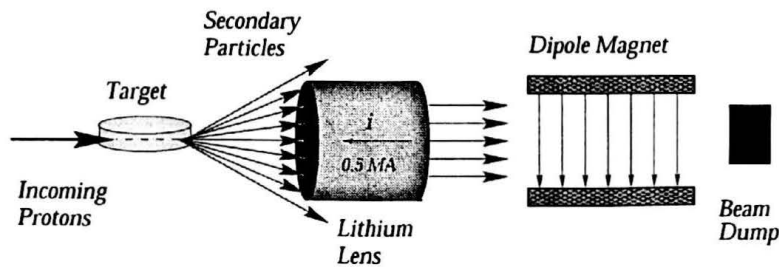


Figure 4.2: Diagram showing the production of antiprotons

4.2 The Collider Detector at Fermilab (CDF)

The Collider Detector at Fermilab (CDF) is a general purpose solenoidal detector designed to study $p\bar{p}$ collisions at $\sqrt{s} = 1.8$ TeV. The CDF measures the energy and momentum, and identifies particles over as large a fraction of the solid angle as possible by surrounding the interaction region with layers of different detector components. Several detector components are designed for distinct tasks. Starting at the interaction point, particles encounter the beam pipe, tracking system, calorimetry and muon detectors, in sequence. Because of the natural phase space for energetic hadron collisions described by rapidity, transverse momentum and azimuthal angle, detector components are almost cylindrically symmetric with respect to the beamline and uniformly segmented in azimuth (ϕ) and pseudo-rapidity (η).

The CDF consists of the movable **central detector** which has polar angle coverage $10^\circ < \theta < 170^\circ$ and is made up of the solenoidal magnet, steel yoke, tracking system, electromagnetic and hadronic calorimeters and muon detectors, and two symmetrical **forward/backward detectors** which has polar angle coverage $\theta < 10^\circ / \theta > 170^\circ$ and is made up of the Beam-Beam Counters (BBC), electromagnetic and hadronic calorimeters and muon toroidal spectrometers. Figure 4.3 shows an isometric view of the CDF detector.

Figure 4.4 shows one quarter of a CDF elevation view with coordinate system definition. The CDF uses a right-handed coordinate system where the z -axis is aligned along the proton direction at the interaction point, the x -axis points away from the center of the Tevatron ring, which leaves the y -axis pointing up out of the ground. We assume the nominal interaction point to be at the center of the detector. The polar angle (θ) and azimuthal angle (ϕ)

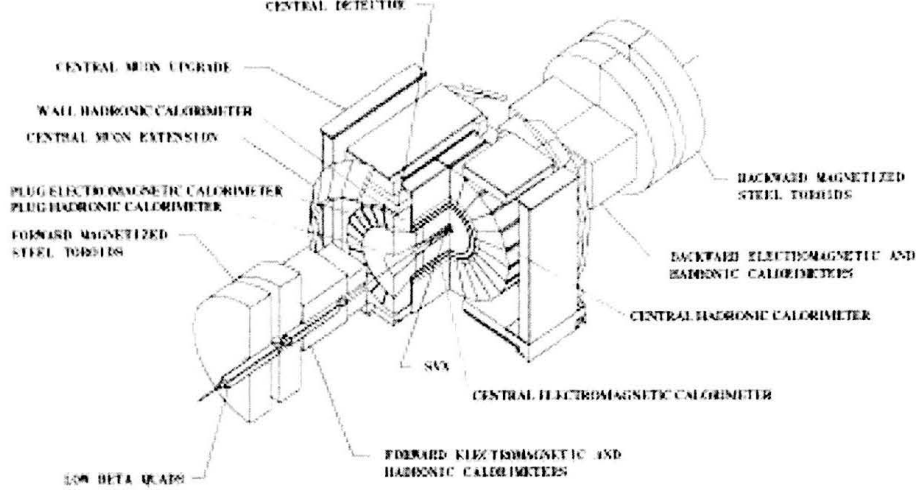


Figure 4.3: Isometric view of the CDF with a quadrant cut away to show the tracking system

are measured from the z -axis and the x -axis respectively, while the cylindrical radius (r) measures the perpendicular distance from the beamline. Transverse quantities like p_T and E_T refer to as “projections” in the r - ϕ plane.

$$p_T = p \times \sin \theta, \quad E_T = E \times \sin \theta \quad (4.1)$$

For particles with momenta large compared to their masses such as electrons and muons at the Tevatron, the p_T and E_T are nearly identical. However, p_T refers to momentum measured in the Central Tracking Chamber (CTC) and E_T refers to energy measured in the calorimeters. Finally, pseudo-rapidity is defined as

$$\eta \equiv -\ln \tan \left(\frac{\theta}{2} \right). \quad (4.2)$$

Pseudo-rapidity is a convenient variable to express angle with respect to the

beam, since it is independent of mass unlike rapidity (y). For massless particle, pseudo-rapidity is equal to rapidity. In minimum bias events, the average number of particles per unit pseudo-rapidity is approximately constant.

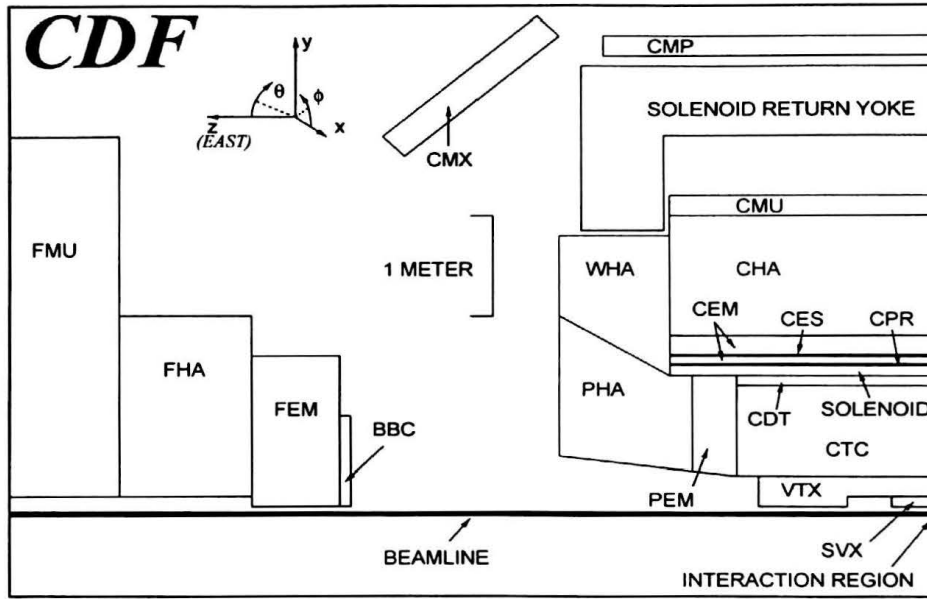


Figure 4.4: Quarter section of the CDF with coordinate system definition

The central detector includes the calorimeter endplugs which form the pole pieces for the solenoidal magnet and have polar angle coverage $10^\circ < \theta < 30^\circ$ and $150^\circ < \theta < 170^\circ$. The steel yoke forms a large box 9.4 m high by 7.6 m wide by 7.3 m long. The superconducting coil and the endplugs are supported by the yoke. The whole yoke assembly rolls from its garaged position in the CDF assembly building to its position in the Tevatron beamline. The 31.4 m move takes one day. At angles less than 10° to either the proton or antiproton beam, particles produced at the interaction point exit the conical holes in the endplugs and strike either the forward or backward calorimeters. On each

end the calorimeter are followed by two 7.6 m diameter steel toroidal magnets used as muon spectrometers. The BBC, a single plane of scintillator at the front face of the calorimeter in the forward and backward detectors, provide a minimum bias trigger and luminosity monitor.

Event analysis is based on precise charged particle tracking, magnetic momentum analysis, fine grained projective calorimetry and fine grained muon detection. Charged particle momenta are analyzed in a 1.4 T solenoidal magnetic field generated by a superconducting coil. The tracking system measures particle momenta with a resolution better than $\delta p_T/p_T^2 = 2 \times 10^{-3} \text{ (GeV/c)}^{-1}$ in the region $40^\circ < \theta < 140^\circ$, and $\delta p_T/p_T^2 = 4 \times 10^{-3} \text{ (GeV/c)}^{-1}$ for $21^\circ < \theta < 40^\circ$ and $140^\circ < \theta < 159^\circ$. The calorimetry has polar angle coverage from 2° to 178° and full azimuthal coverage, consists of electromagnetic and hadronic calorimeters, and is segmented into about 5000 solid angle elements called “projective towers.” It measures the energy of electrons, photons and jets. A muon is identified by drift chambers in the region $56^\circ < \theta < 124^\circ$ and by either forward or backward toroid system in the range $3^\circ < \theta < 16^\circ$ and $164^\circ < \theta < 177^\circ$. Isolated high momentum muons can be identified in the intermediate angular range by a comparison of the tracking and calorimetry information in many cases.

The three most relevant detector components for this analysis are the tracking system, calorimetry and muon detectors. The following subsections briefly describe these detector components with particular emphasis on geometrical coverage which have a direct bearing on physics results.

4.2.1 The Tracking System

The trajectories of the charged particles are reconstructed in three dimensions and their momenta are precisely measured using the tracking system. The tracking system overlaps the calorimeter acceptance. The tracking system consists of the Silicon Vertex detector (SVX), Vertex Time Projection Chambers (VTPC or VTX), Central Tracking Chamber (CTC) and Central Drift Tubes (CDT). All four sub-systems are immersed in a uniform 1.4 T magnetic field. The field is produced by a 3 m diameter 5 m long superconducting solenoidal coil. The coil is made of 1164 turns of an aluminum stabilized NbTi/Cu superconductor, fabricated by the Extrusion with Front Tension (EFT) method in which high purity aluminum is friction welded to the superconducting wire during the extrusion process. The overall radial thickness of the solenoid is 0.85 radiation lengths.

The SVX, the innermost tracking system surrounding the beryllium beampipe of 1.9 cm radius, is used to determine the momenta of charged particles in conjunction with the CTC and to reconstruct vertices displaced from the primary interaction. These secondary vertices result from b or c quark decays. Originally the SVX was installed in the CDF detector in 1992 and was replaced by new radiation hard silicon vertex detector, the SVX', in 1993. The SVX' has several improvements over the original SVX, such as better signal-to-noise and higher efficiency.

The SVX' modules (or barrels) consist of four concentric layers of silicon microstrip detectors segmented into twelve 30° wedges according to ϕ and numbered from 0 to 3 in increasing radius. Two such modules are aligned along the beam direction with a gap of 2.15 cm at $z = 0$. The total active length

of the SVX' is 51.1 cm which results in a geometrical acceptance of $\sim 60\%$ of the $p\bar{p}$ interaction vertices, since true interaction vertices are spread along the beamline by a Gaussian distribution centered on $z = 0$ with $\sigma = 30$ cm. The basic detector element is called a "ladder" and there are total 96 ($= 12$ wedges $\times 4$ layers $\times 2$ modules) ladders in the complete detector. The adjacent ladders overlap each other slightly to ensure that the SVX' provides complete coverage in ϕ . The inner and outer radii of the module are 2.86 cm and 7.87 cm, respectively. The layer 0 is closer to the beamline than the SVX by $\sim .14$ cm and the ladders in layer 0 have an additional 1° rotation along their longitudinal axis. There is 0.17° (0.24 strip) overlap between the adjacent layer 0 ladders at the edges in the SVX' compared to 1.26° gap in the SVX. A ladder has three AC coupled, single-sided silicon microstrip detectors microbonded together. Axial microstrips with $60\ \mu\text{m}$ pitch on the three innermost layers and $55\ \mu\text{m}$ pitch on the outermost layer provide precision track reconstruction in the plane transverse to the beam. The readout end of the ladder is microbonded to the front end chips. The SVX and SVX' have a total of 46080 readout channels. Figure 4.5 and Figure 4.6 show schematic drawings of one of the SVX' modules and the SVX' ladders.

The SVX' is an AC-coupled detector with a radiation hard front-end readout circuit, SVX IC Rev. H3 (noisy but radiation hard, henceforth SVXH3 chip), so that radiation induced leakage currents will not saturate the input of preamps. SVXH3 was fabricated in $1.2\ \mu\text{m}$ CMOS technology and the CMOS process was radiation hard. It is expected to have a radiation tolerance in excess of 1 Mrad. This chip has 30 (40)% more gain than the chip used for the SVX. Typical gains are around 21 mV/fC at the input capacitance typical of our detectors, which is $\simeq 30$ pF for a full strip length of 25.5 cm. The SVX'

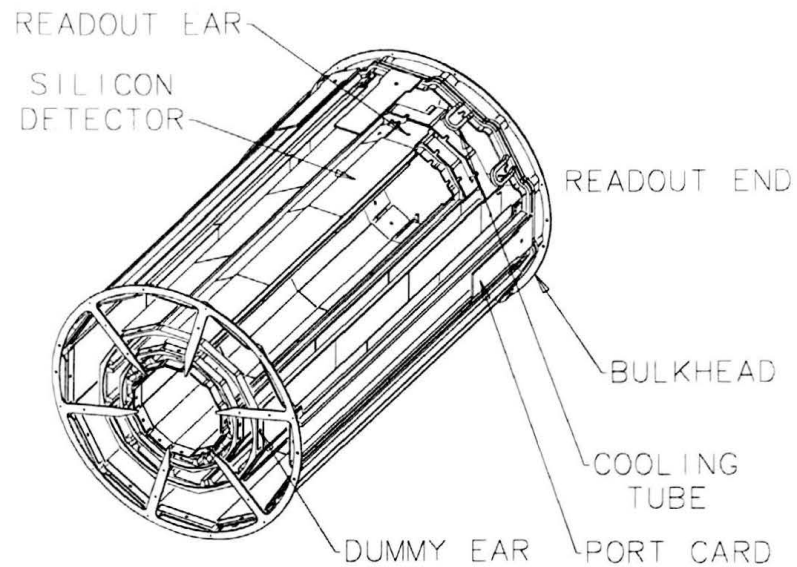


Figure 4.5: Schematic drawing of one of the SVX' modules (barrels). Two modules are joined at the dummy ear sides.

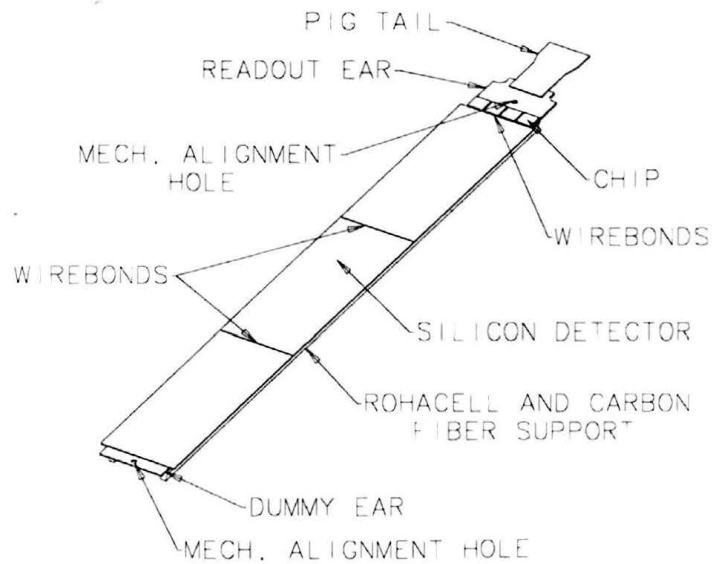


Figure 4.6: Schematic drawing of one of the SVX' ladders

has lower noise due mostly to the AC coupling. The SVX was a DC-coupled detector with SVX IC Rev. D (less noisy but radiation soft, henceforth SVXD chip) and in order to get rid of the baseline shift due to the varying strip to strip leakage currents which would also be integrated during the sampling time it had to be operated in quadruple sample & hold mode. In this mode the charge is integrated twice, once “on beam” and once “off beam,” and the difference of these integration gives the signal. In case of the AC coupled detectors like the SVX', to maximize the advantages of them that the leakage current will not be seen by the readout electronics, double sample & hold mode with only one charge integration (“on beam”) can be used so the noise is lower by a factor $\sqrt{2}$ compared to the SVX.

The average spatial resolutions are $13\ \mu\text{m}$ for the SVX and $11.6\ \mu\text{m}$ for the SVX'. The impact parameter resolutions for the high transverse momentum track are $17\ \mu\text{m}$ for the SVX and $13\ \mu\text{m}$ for the SVX'. We measured a signal-to-noise ratio of 9 for the SVX and 15 (16) for the SVX'.

The **VTPC (or VTX)** surrounds the SVX (or SVX') and provides tracking information upto a radius of 22 cm and $|\eta| < 3.25$. It is used to measure the $p\bar{p}$ interaction vertex along the z -axis with a resolution of 1 mm by finding the point of convergence of all the reconstructed tracks in the event. Exact knowledge of the event vertex is important for lepton track reconstruction, measurements of the transverse energy (E_T) and missing transverse energy (\cancel{E}_T), and so on. The primary vertex is required to be within ± 60 cm of $z = 0$. In events with more than one reconstructed vertex, the primary vertex is taken to be the one with the largest number of VTPC hits on its associated tracks. The VTPC is also used to detect the photon conversion.

The **CTC** is a main detector to detect charged particles in CDF. If is

a large cylindrical drift chamber with excellent spatial and momentum resolution. It covers the central region, $|\eta| < 1$, with 3.2 m in length, inner radius of 0.3 m, and outer radius of 1.3 m. It is mounted outside the VTPC.

The CTC contains 6156 sense wires grouped into 84 layers, and these layers are again grouped into 9 superlayers labelled 0 to 8 from the most inner layer. The five (0, 2, 4, 6 and 8) of the superlayers are axial superlayers whose wires are parallel to the beamline. Each axial superlayer consists of 12 layers of sense wires. There are four stereo superlayers (1, 3, 5 and 7) which consist of 6 layers of sense wires tilted $\pm 3^\circ$ relative to the beamline in order to provide r - z information. The tracking algorithm begins by reconstructing charged particle tracks in the r - ϕ plane using information from the axial superlayers. The z -position of the primary vertex is used as a seed for the stereo track reconstruction, the z -position of a track. The momentum resolution for isolated and high p_T tracks is better than $\delta p_T/p_T^2 = 2 \times 10^{-3} (\text{GeV}/c)^{-1}$, when the track is constrained to go through the beam position determined for each run. The CTC track information combined with SVX information improves the resolution upto $\delta p_T/p_T^2 = 1 \times 10^{-3} (\text{GeV}/c)^{-1}$. Figure 4.7 show an endplate of the CTC displaying the 45° tilt of the superlayers to the radial direction to correct for the Lorentz angle of the electron drift in the magnetic field in gas mixture consisting of 49.6% of argon, 49.6% of ethane, and 0.8% of ethanol. The sense wires in each superlayers are organized into r - ϕ cells.

The CDT are located on the outer cylindrical surface of the CTC and just inside solenoidal magnet. The CDT provide high-accuracy three-dimensional r - ϕ - z information of tracks via both drift time and charge division measurements in the central region, $|\eta| < 1$.

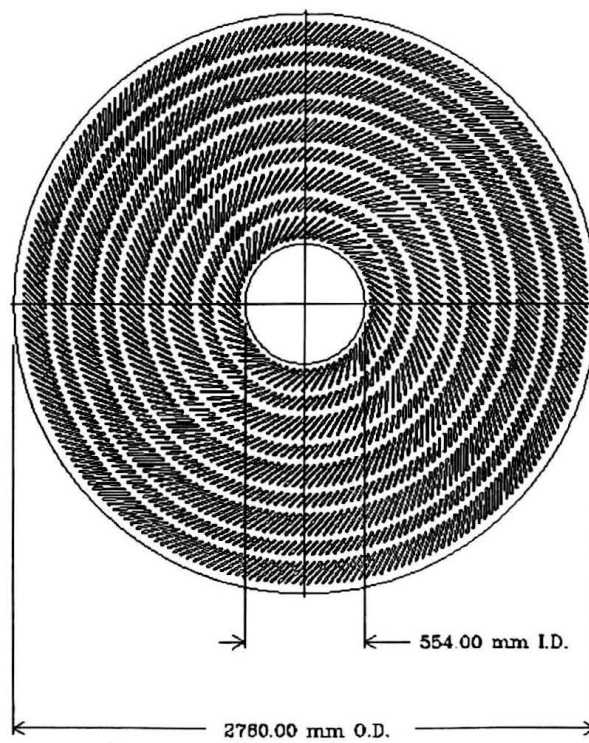


Figure 4.7: An endplate of the CTC showing the arrangement of the blocks which hold the 84 layers of sense wires

4.2.2 The Calorimetry

The calorimetry provides identification of, and energy measurement for jets, electrons, and photons, by stopping them and measuring the absorbed energy. The whole calorimetry covers $|\eta| < 4.2$ and full azimuthal angles. Because of the importance of the hadronic jets in high energy $p\bar{p}$ collisions, the calorimeters are segmented in pseudo-rapidity and azimuth to form a projective tower geometry which points back to the nominal interaction region. There are three separate calorimeters covering different η regions, the central, endplug, and forward/backward. The central calorimeter is located just outside the solenoid and the forward/backward detectors house calorimeters. Each has an electromagnetic calorimeter (CEM, PEM, FEM) in front of a corresponding hadronic calorimeter (CHA/WHA, PHA, FHA) so that one can make a comparison of electromagnetic to hadronic energy on a tower by tower basis. All of the electromagnetic calorimeters use lead as the absorber, while the hadronic calorimeters use iron. The CEM is composed of alternating layers of lead and scintillator, whereas the CHA and WHA are composed of alternating layers of iron and scintillator. The others use gas proportional chambers, instead of scintillators, as the active sampling medium. The towers are 0.1 units of η wide by 15° (central region) or 5° (endplug and forward/backward region) in ϕ . The physical size of a tower ranges from about 24.1 cm (η) \times 46.2 cm (ϕ) in the central region to 1.8 cm (η) \times 1.8 cm (ϕ) in the forward/backward region. Table 4.1 shows the coverage in pseudo-rapidity and energy resolution for the calorimeters. Figure 4.8 shows the η - ϕ segmentation of the whole calorimeters.

	η coverage	Energy resolution
CEM	$ \eta < 1.1$	$13.5\%/\sqrt{E_T} \oplus 2\%$
CHA	$ \eta < 0.9$	$50\%/\sqrt{E_T} \oplus 3\%$
WHA	$0.7 < \eta < 1.3$	$75\%/\sqrt{E_T} \oplus 4\%$
PEM	$1.1 < \eta < 2.4$	$22\%/\sqrt{E_T} \oplus 2\%$
PHA	$1.3 < \eta < 2.4$	$106\%/\sqrt{E_T} \oplus 6\%$
FEM	$2.2 < \eta < 4.2$	$26\%/\sqrt{E_T} \oplus 2\%$
FHA	$2.4 < \eta < 4.2$	$137\%/\sqrt{E_T} \oplus 3\%$

Table 4.1: η coverage and energy resolution for the various calorimeters. The symbol \oplus signifies the constant term to be included in quadrature to the resolution. Energy resolutions for the electromagnetic calorimeters are for incident electrons and photons. For the hadronic calorimeters, they are for pions. E_T should be expressed in GeV.

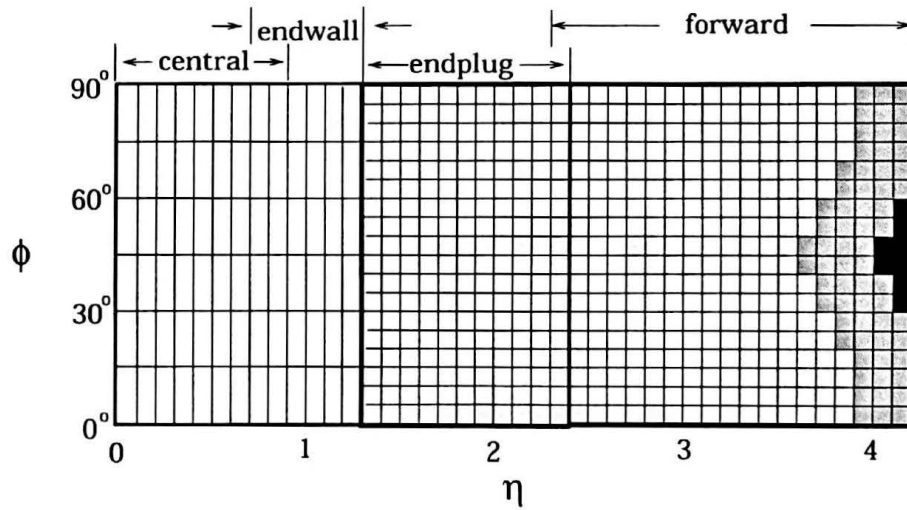


Figure 4.8: The η - ϕ segmentation of the CDF calorimeters. The shaded area in the forward/backward region is where there is only electromagnetic coverage, and the black area has no coverage at all due to the presence of Tevatron steering magnets.

4.2.3 The Muon Detectors

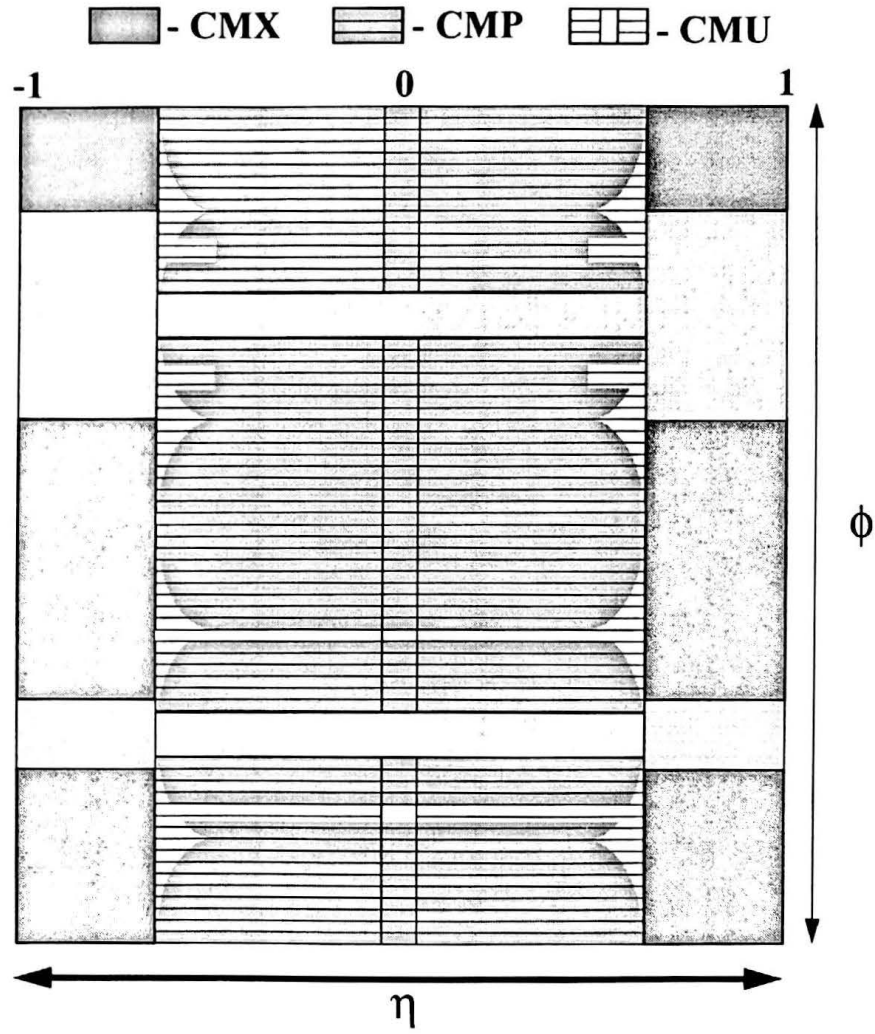
The CDF has traditionally emphasized charged particle tracking and lepton identification. Triggering and reconstructing muons is at the core of several broad physics program. Muons radiate much less energy than electrons, since the mass of muon is roughly 200 times heavier than the mass of electron. Muons interact only through the electroweak force and they don't feel the strong force. Therefore, they don't interact strongly with nuclei as hadrons do. These properties cause muons to be extremely penetrating. Because of this reason, the muon detectors are located outside substantial material like the calorimetry which shield the muon detectors from most other particles in both the central and forward/backward regions.

Central muons are identified by their penetrating ability, and detected by the Central MUon chambers (CMU), the Central Muon uPgrade (CMP)/CSP system, and the Central Muon eXtension (CMX)/CSX system. The momentum of muon is measured by its bending in the solenoidal magnetic field using the tracking system. Figure 4.9 shows the η - ϕ coverage of three systems.

Forward muons are identified and detected by the Forward MUon (FMU) system, and their momenta are simultaneously measured in toroidal magnetic field of the FMU system.

The CMU drift chambers identify muons in the central region, $|\eta| \leq 0.6$, by measuring their positions and directions and providing a Level 1 trigger for muons which have a transverse momentum greater than a given value. The trigger system is explained in Section 4.2.4

The CMU is located around the outside of the central calorimeter at a radial distance of 347 cm from the beampipe. It is segmented in ϕ into

Figure 4.9: The central muon detection coverage in the η - ϕ plane

12.6° wedges which fit into the top of each central calorimeter wedge, while leaving a gap in the central muon coverage of 2.4° between each wedge. Each wedge is further segmented in ϕ into three modules of 4.2° each which bolted together at each end to form a single unit. This unit is suspended from the top of the calorimeter wedge at three points which provide for adjustment of the chambers in both η and ϕ . Each of the three modules in a wedge consists of four layers of four rectangular drift cells. Overall dimensions of the cell are 6.35 cm (width) \times 2.68 cm (height) \times 226.1 cm (length). A 50 μm stainless steel sense wire with a length of 226.1 cm and a resistance of $0.4 \Omega\text{mm}^{-1}$ is located at the center of the cell. The wire is placed under a tension of 110 g which limits the wire sag to 90 μm . Therefore, the CMU consists of total 144 ($= 2 \text{ barrels} \times 24 \text{ wedges} \times 3 \text{ stacks}$) modules with 16 rectangular cells per module.

Four sense wires, one from each layer, make up a muon stack (or tower). Two of the four sense wires from alternating layers lie on a radial line which passes through the interaction point. The remaining two wires of the stack lie on a radial line which is offset from the first by 2 mm at the midpoint of the chambers. Each wire pair, the first and third wires and the second and fourth wires, ganged together in the readout and is instrumented with a TDC to measure the position of muon in ϕ , and an ADC on each end to measure the position of muon in z via charge division. The ambiguity as to which side of sense wires in ϕ a track passes is resolved by determining which wire pair was hit first. The angle between a particle track and the radial line passing through the sense wires can be determined by the measuring the difference in arrival times of the drift electrons.

The position of a track along the sense wire (pseudo-rapidity), and the drift direction (ϕ) is measured by charge division and TDC, respectively. For

charge division calibration ^{55}Fe sources have been used. An rms resolution of 1.2 mm along the sense wire and an rms resolution of $250\text{ }\mu\text{m}$ in the drift direction are attained.

The chambers operate in the limited streamer mode with a 50%/50% ratio of argon/ethane gas bubbled through 0.7% ethanol.

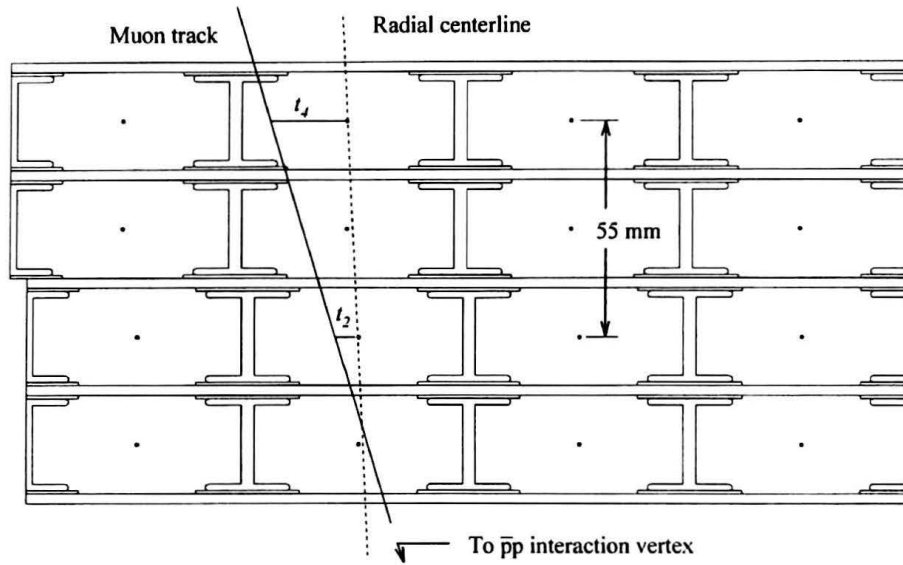


Figure 4.10: A drawing of a CMU tower showing a muon track.

The **CMP** is the second set of chambers which are located outside the CMU, behind an additional 60 cm of steel in the same pseudo-rapidity region as the CMU's, $|\eta| \leq 0.6$. The chambers are of fixed length in z and form a box around the CMU. Thus, the pseudorapidity coverage varies with ϕ .

The chambers of the CMP are rectangular drift tube cells configured in four layers with alternate half-cell staggering. For easy field shaping, dimensions of the cell are 15 cm (width) \times 2.5 cm (height) \times 640 cm (length). They are typically 640 cm long with some shorter sections on the bottom of the

detector to avoid obstructions. The tubes are made of aluminum extrusions with 0.26 cm walls, having a single wire in the center and field shaping cathode strips on the top and bottom. The extrusions are glued into four-tube stacks with a half-cell staggering of the second and fourth layers relative to the first and third. Pre-amplifiers are mounted on one end of the stacks. Signals are read out by a single TDC per wire, and trigger hits are formed from coincidences of nearby wires that are used in association with trigger information from the CMU. The chambers are run in proportional mode with a maximum drift time of approximately $1.4 \mu\text{s}$.

A layer of scintillation counters is installed on outside surface of the wall drift chambers. These are called the **CSP**. The counters are rectangular in shape and dimensions of them are 2.5 cm (thickness) \times 30 cm (width) \times 320 cm (length). Each counter covers two chambers in width and half the chamber length. The total number of scintillation counters is 216. The counters are read out by single phototubes which are located at the center of the array. The east and west counters are offset in x to allow the interleaving of phototubes at the middle, minimizing the space occupied by the light-guide/PMT assembly.

The **CMX/CSX system** is located at each end of the central detector and extends in polar angle from 42° to 55° . At 55° the conical sections of drift tubes, the CMX, and the conical sections of scintillation counters, the CSX, slightly overlap the coverage provided by the CMU and CMP systems and extends its pseudo-rapidity coverage from 0.65 to 1.0. No additional steel was added for this system, but the large angle through the hadronic calorimeter, magnetic yoke, and steel of the detector end support structure yields considerably more absorber material on average than in the CMU.

The azimuthal coverage of this system has a 30° gap at the top of the

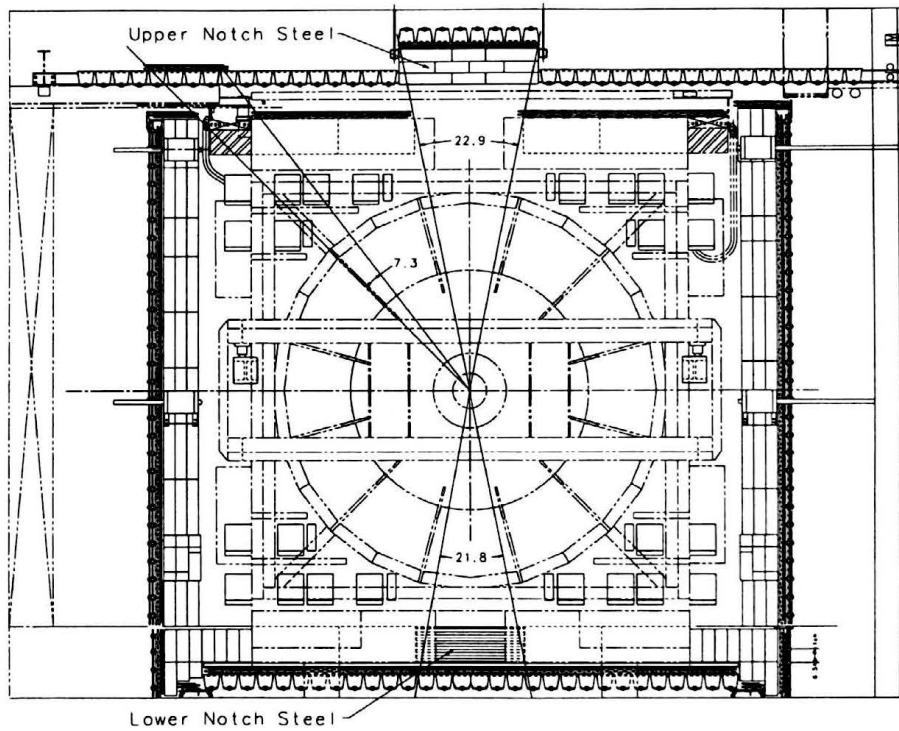


Figure 4.11: Configuration of the CMP/CSP system and steel absorber. The circles on the walls are the ends of PMTs. On the top and bottom, the trapezoids are the light-guides viewed end-on. This figure includes the part planned to be upgraded for the next run, Run II [45].

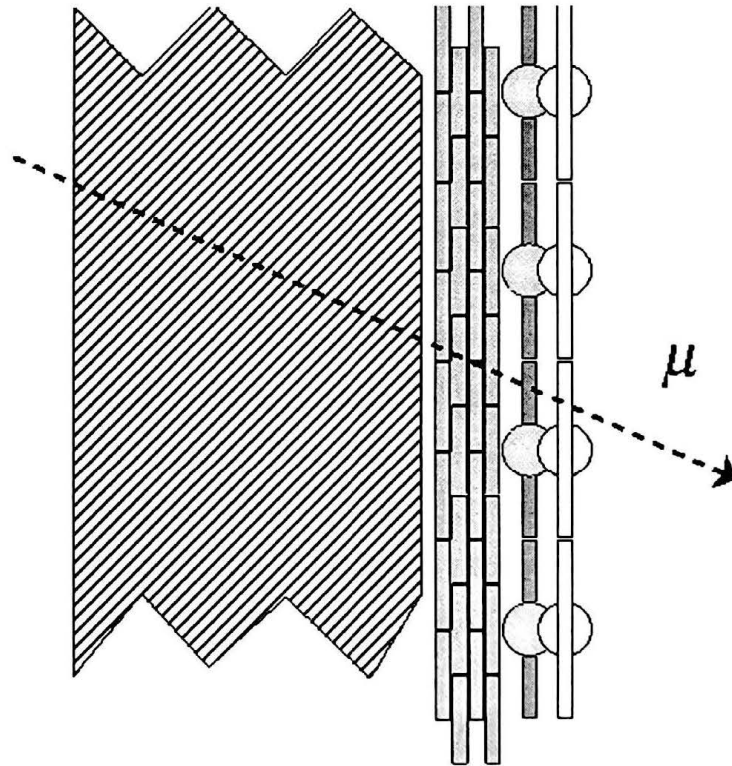


Figure 4.12: Detail showing the configuration of steel, drift chambers, the scintillation counters for the CMP walls. A muon track is drawn to establish the interaction point. Counter readout is located at $z = 0$. Layers of scintillation counters are offset from the chambers and from each other in x to allow overlapping light-guides and PMTs, minimizing the space required [45].

detector for the Main Ring and the solenoid refrigerator. There has been also a 90° gap at the bottom of the detector where the conical sections are interrupted by the floor of the collision hall, but a fan-shaped 90° CMX/CSX section will be installed in this gap to complete the coverage at the bottom for the next run starting in early 2001.

The drift tubes of the CMX are arrayed as a logical extension of the CMU and CMP. There are four logical layers of twelve tubes for each $15^\circ \phi$ sector, and successive layers are half-cell staggered to eliminate ambiguities. Each logical layer consists of two physical layers of drift tubes which partially overlap each other. The overlap is greater at the inner edge as a result of forming a conical surface with rectangular cells. This overlap not only provides redundancy – the average muon intersects six cells – but the resulting stereo angle of 3.6 mrad between adjacent cells permits the measurement of the polar angle of the track. The drift tubes of the CMX differ from those of the CMP only in length. Their length is 180 cm. The total number of tubes installed is 1536.

A layer of four scintillation counters is installed on both the inside and the outside surface of each 15° CMX sector. These are called the CSX. The counters are trapezoidal in shape with the same length as the drift tubes, 180 cm, and with a width of 30 cm at the smaller end and 40 cm at the larger end. The counters on the inside and outside layers are half-cell staggered with respect to each other thereby doubling the effective granularity of the CSX. The total number of counters is 256.

The counters are read out by single phototubes which are located on opposite ends for the inside and outside layers. The mean time of the signals from a particle traversing both layers is independent of the location of the

track along the length of the counters, and the distribution of hit arrival time for real tracks is smeared only by the track path length difference due to the distribution of interaction z vertex. The mean time is calculated in the trigger, and the excellent timing resolution of the counters is used to reject large CMX backgrounds from out-of-time interactions in the beampipe and the face of the forward calorimeter.

The **FMU** is a muon spectrometer system for the pseudo-rapidity region of $2.0 < |\eta| < 2.8$, and one of the elements of the CDF forward and backward detectors.

Each spectrometer consists of a pair of steel (iron) toroidal magnets instrumented with three planes of drift chambers in front of the first toroid, between two toroids, and behind of the second toroid, and two planes of scintillation trigger counters hung outside of the front drift chamber plane and inside of the rear drift chamber plane. Each drift chamber plane is composed of two planes of drift cells and they are called the “coordinate plane” and “ambiguity plane,” respectively. The former is closer to the beam crossing point than the latter.

4.2.4 The Trigger System

The trigger plays an important role in hadron collider experiments, because the collision rate is much higher than the rate at which data can be stored on tape. The role of the trigger is to efficiently extract the most interesting physics events from the large minimum bias events.

The CDF detector has been designed to study the physics resulting from $p\bar{p}$ interactions at $\sqrt{s} = 1.8$ TeV. The interaction rate at the collider, at the nominal luminosity of $10^{30} \text{ cm}^{-2}\text{s}^{-1}$, is 50–75 kHz with a typical minimum bias multiplicity of fifty or more particles. For picking out events of particular interests from the complex event structure, the CDF trigger system has a three level structure. Each level provides a rate reduction sufficient to process in the next level with minimal deadtime. The first two consist of specially designed hardware which makes the decision to initiate the full detector readout. The last consists of a software processor farm. The idea behind the multi-level trigger structure is to introduce as little bias as possible at the lower levels, with the reduction of the rate to a point where the next level can do a more sophisticated analysis without incurring significant deadtime.

The design goal of the trigger can be summarized as follows. First, we must be capable of triggering on the signatures of known physics. Second, the trigger should be flexible enough to encompass signatures of new physics. Finally, the various strengths of the detector should be exploited to the fullest extent possible. For the CDF detector, these strengths are a finely segmented and projective calorimetry, excellent tracking and strong magnetic field. These features allow a trigger decision based on the topology of transverse energy and identification of electrons, muons, taus, photons and jets in the event.

The Level 1 (L1) decision is based on the global energy deposition in the calorimetry as well as the presence of hits in the muon chambers and stiff tracks in the CTC. The L1 decision is made in the $3.5\ \mu\text{s}$ between beam crossings (six bunch collider operation) incurring no deadtime while reducing a raw event rate of 50–70 kHz to a few kHz. The Level 2 (L2) decision is made by the topology of the event operating on calorimeter clusters, central stiff tracks and muon candidates. It is possible to perform simple calculations such as finding the invariant mass of a group of clusters, to associate stiff tracks with calorimeter clusters and therefore to do a first order electron- π^0 jet discrimination. The L2 decision is made in approximately $10\ \mu\text{s}$ (a longer decision time may be allowed) incurring less than 10% deadtime while reducing the rate to 1–100 Hz. Readout of all the detector elements begins after a L2 trigger has been satisfied. The L2 trigger is able to prescale the data, which means a trigger can be set to accept one of every N events that would normally pass that trigger. A trigger can have a large prescale when the instantaneous luminosity is high, and a small prescale when the instantaneous luminosity is low: this is known as “dynamic prescale.” The effect of the prescale factors can be a decrease in the total luminosity or efficiency of a trigger. The rate of data taking will be limited by two factors: the rate at which events can be written to tape and the rate at which physicists can analyze the data. The first of them limits the data taking rate at CDF about 1 Hz. This coincides nicely, given the projected computing power, with the rate at which data can be analyzed. Thus, it is the formidable task of the trigger system to choose 1 out of every 50 to 75 thousand events to be written to tape. The Level 3 (L3) system is a farm of computers that executes a slightly streamlined version of the offline reconstruction code and writes data on the tape as last stage.

The L1 decision is based on the following information:

- Electromagnetic, hadronic and total transverse energy, summed over those calorimeter elements which are above programmable thresholds.
- The transverse energy imbalance in the electromagnetic and hadronic calorimeters, given by $E_T \cos \phi$ and $E_T \sin \phi$ summed over those calorimeter elements which are above programmable thresholds, where $E_T \cos \phi$ and $E_T \sin \phi$ are the x and y components of transverse momentum as measured by the calorimeters.
- The existence of stiff tracks in the CTC (but not their directions) and the existence of muon candidates in the central and forward muon chambers (but not their positions).
- Presence of a beam-beam interaction and/or the presence of a beam-gas interaction.
- Hits in the small angle silicon counters in combination with hits in the beam-beam counters (diffractive and elastic events).

The L2 decision is based on the following parameters:

- Number of energy clusters in the detector and their properties (position, width and transverse energy), corresponding to both electromagnetic and total energy deposition: E_T , $E_T \sin \phi$ and $E_T \cos \phi$, mean pseudo-rapidity ($\langle \eta \rangle$), rms width in pseudo-rapidity (σ_η), mean azimuth ($\langle \phi \rangle$) and rms width in azimuth (σ_ϕ), as well as the presence of high p_T tracks pointing at these clusters.

- The presence and position of track segments in the muon chambers that are associated with high p_T tracks in the CTC.
- Transverse energy summed over the detector as a whole and transverse energy imbalance in the detector.
- Presence of a beam-beam interaction and/or the presence of a beam-gas interaction.

A large fraction of the trigger hardware is used for the L1 and L2 decisions. The trigger is built of a large number of different FASTBUS cards and FASTBUS data transfers are used in the setup and initialization of the trigger system (i.e. for downloading trigger constants and setting control bits), for testing, and during readout.

Chapter 5

Monte Carlo Simulation

A Monte Carlo (MC) program is used to determine corrections for acceptance and some of the efficiencies. The MC program consists of an **event generator** that generates the signal and background processes contributing to the data based on a physics model, and a **detector simulation and reconstruction** which models the response of the detector to the final state particles so that we can estimate an acceptance considering detector resolution effects. Because detector resolution affects the acceptance, the detector model has been tuned so that the simulated results agree with the data based on well-defined control samples.

This analysis has used several event generators to generate the signal and background samples. All the samples are processed through the CDF detector simulation and reconstruction program. The analysis chain used for the real data has been applied to the MC samples in order to estimate the signal acceptance and backgrounds, see Chapter 6. The MC samples used for this analysis are described in Section 5.1. Section 5.2 demonstrates some kinematic variables, which are useful to understand the signal acceptance, at the event

generator level. Section 5.3 briefly describes the CDF detector simulation and reconstruction program. We also summarize some MC correction factors which are necessary when we normalize our MC samples to real data, since the detector simulation and reconstruction program has a tendency to show slight differences in several efficiencies when compared to real data analysis.

5.1 Signal & Background Monte Carlo Samples

To design proper cuts for candidate event selection and to evaluate the cut efficiencies and signal acceptance, the signal MC samples have been generated using ISAJET [46] (Version: 7.44). ISAJET is a MC generator which simulates pp , $p\bar{p}$ and e^+e^- interactions at high energies. ISAJET includes the complete production and decay processes for superpartners in Born approximation. It incorporates perturbative QCD cross sections for a primary hard scattering, initial and final state QCD radiative corrections in the leading log approximation, independent fragmentations of quarks and gluons into hadrons, a phenomenological model tuned to minimum bias and hard scattering data for the beam jets, and ISASUSY which evaluates branching ratios for the MSSM. It is possible that the lifetime of the scalar quarks decaying directly is sufficiently long for hadronization effects to become important. This has been taken into account for b quark. We have generated signal MC samples by assuming eight different masses of the scalar top quark: 70, 75, 80, 90, 100, 110, 120 and 130 GeV/c^2 .

Table 5.1 is a list of possible background sources to baseline $\mu + \tau_h$ samples prerequisite for the whole analysis. They are estimated using a number of MC generators followed by the CDF detector simulation and reconstruction.

real μ & real τ_h	real μ & fake τ_h	fake μ & real τ_h	fake μ & fake τ_h
$\gamma^*/Z \rightarrow \tau\tau$	$W (\rightarrow \mu\nu)+\text{jets}$ $W (\rightarrow \tau\nu \rightarrow \mu\nu\nu\nu)+\text{jets}$	$W (\rightarrow \tau\nu)+\text{jets}$	
$t\bar{t}$	$t\bar{t}$	$t\bar{t}$	
diboson	diboson	diboson	
QCD ($b\bar{b}/c\bar{c}$)	QCD ($b\bar{b}/c\bar{c}$)	QCD ($b\bar{b}/c\bar{c}$)	QCD
	$\gamma^*/Z \rightarrow \mu\mu$		

Table 5.1: Possible background sources to baseline samples

The production and decay of the single vector bosons associated with any jet are simulated by VECBOS [47] (Version: 3.0). VECBOS provides a LO QCD calculation, which is enhanced with a shower evolution of both initial and final state partons and hadronization by the interface with HERPRT routine of HERWIG [49] (Version: 5.6). We choose $Q^2 = \langle p_T \rangle^2$ as the QCD parameters of renormalization and fragmentation in VECBOS and HERWIG. In case of $Z \rightarrow \tau\tau$ events, we have simulated them using ISAJET with $5 \text{ GeV}/c < q_T < 500 \text{ GeV}/c$ which effectively reproduces the multiplicity and E_T distributions of jets in W or Z production [50]. Because we “calibrate” the scalar top quark search with $Z(\rightarrow \tau\tau) + 0\text{-jet}$ analysis, the study with the samples simulated in the same environment as scalar top quark signal samples is necessary for consistency. Concerning the calibration procedure, we estimate the acceptance of $Z(\rightarrow \tau\tau) + 0\text{-jet}$ events with these samples. The $Z(\rightarrow \tau\tau) + 0\text{-jet}$ analysis is explained in detail in Section 6.3. The pair-production and decay of the

vector bosons are simulated using ISAJET. The pair-production and decay of the top quarks are simulated using ISAJET. The Drell-Yan (γ^*) events are also simulated using ISAJET with $5 \text{ GeV}/c < q_T < 500 \text{ GeV}/c$. The QCD background is the most difficult one to estimate with MC simulation because of a large cross section and low fake rate. The MC study of QCD events is not carried out in this analysis. However, most of the QCD events in OS $\mu + \tau_h$ pairs are estimated by the LS $\mu + \tau_h$ pairs: this is the “OS–LS” subtraction method. Table 5.2 is a summary of background MC samples. All six of the SM background processes have been simulated with much more than the luminosity of the real data.

CTEQ4L [53] is our standard PDF to generate all MC samples. The top quark mass has been fixed at $175 \text{ GeV}/c^2$. TAUOLA [60, 61, 62, 63] (Version: 2.5) is included in the simulation of tau decays. Every event generator handles tau decays in slightly different way in the aspect of tau polarization, branching ratios, and so on. Therefore, we redecay taus according to TAUOLA library to handle tau decays correctly and consistently. The tau branching ratio to muon and neutrinos is approximately 18% and to hadrons is approximately 64% [6]. QQ [48] (Version: 9.1, the lifetime of b quark is 1.45 ps), based on measurements from the CLEO experiment, is included to simulate b quark decays.

To normalize the background MC samples to real data, we have taken the production cross section times branching ratio and trigger efficiencies into account. Then, the MC samples are corrected by several correction factors explained in Section 5.3. The production cross section times branching ratios ($\sigma \cdot B$) are taken from the CDF measurements [40, 55, 56, 57] or the NLO QCD calculations [58, 59]. We assume $\sigma \cdot B(Z \rightarrow ee) = \sigma \cdot B(Z \rightarrow \mu\mu) = \sigma \cdot B(Z \rightarrow \tau\tau)$. The trigger efficiencies are explained in detail in Section 6.1.

SM Processes	Event generators
$Z(\rightarrow \tau\tau) + \text{jets}$	VECBOS+HERPRT
$W(\rightarrow \mu\nu) + \text{jets}$	VECBOS+HERPRT
$W(\rightarrow \tau\nu) + \text{jets}$	VECBOS+HERPRT
γ^*	ISAJET
$WW/WW/ZZ$	ISAJET
$t\bar{t}$	ISAJET

Table 5.2: Summary of background MC simulation samples

5.2 Kinematics of Signals at Generator Level

Figure 5.1 shows the distributions of two kinematic variables at the event generator level, since they are important for the design of event selection cuts. They are also helpful to understand signal acceptance. The signal events used for the figures have $M_{\tilde{t}_1} = 100 \text{ GeV}/c^2$.

The left figures demonstrate the p_T distributions of muons from $\tau \rightarrow \mu\nu_\mu\nu_\tau$ (top) and hadronic taus (middle), and the E_T distribution of two b quark jets (bottom). The right figures show the η distributions of muons (top), hadronic taus (middle) and two b quark jets (bottom). The definitions of p_T , E_T and η have been explained in the previous chapter. The small areas filled with a different color show the events passing two event selection criteria of p_T (or E_T) and η simultaneously. The cut values are given in the next chapter which explains the candidate event selection in detail.

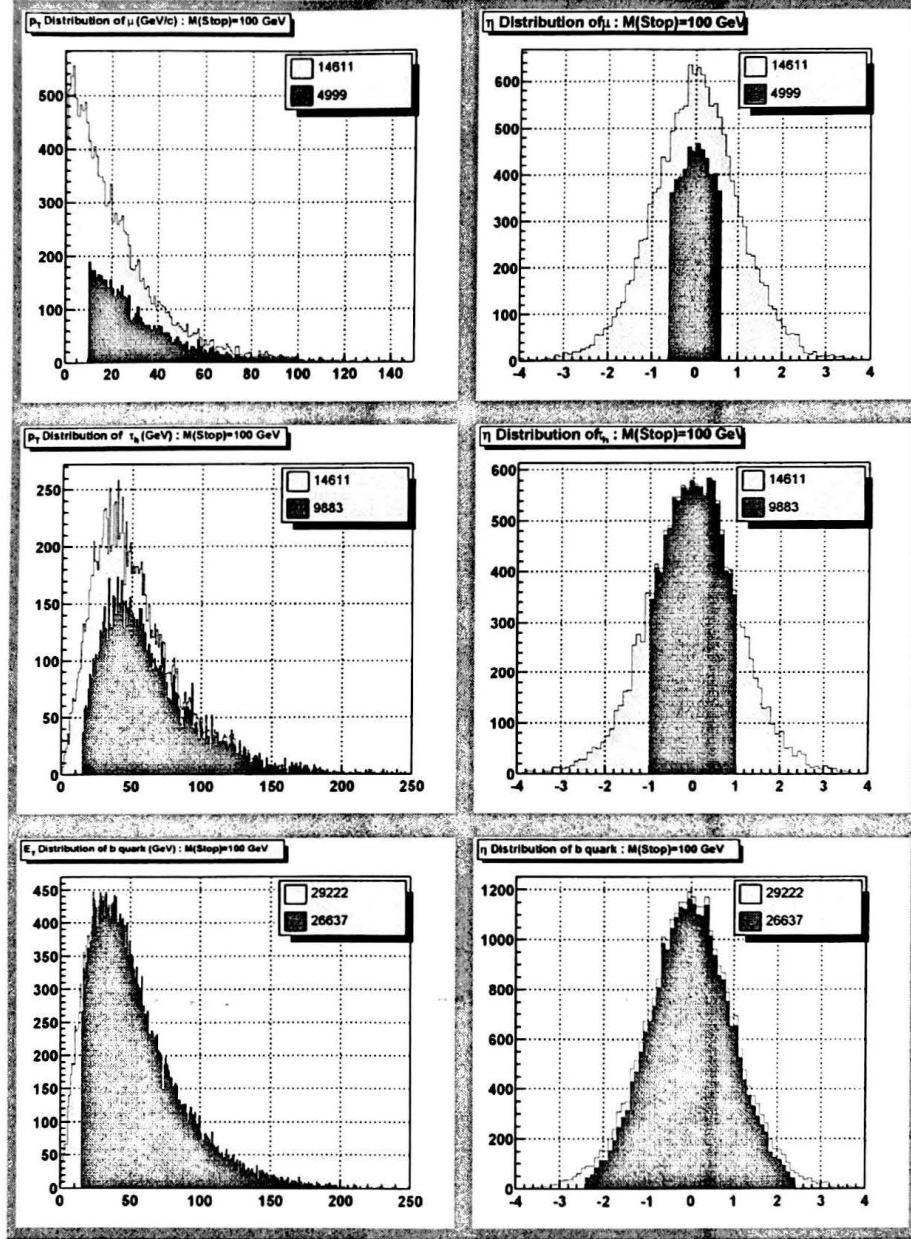


Figure 5.1: The p_T or E_T (left) and η (right) distributions of muons (top), hadronic taus (middle) and b quarks (bottom) at the event generator level. $M_{\tilde{t}_1} = 100 \text{ GeV}/c^2$.

5.3 Detector Simulation and Reconstruction

CDF provides two different packages, QFL' and CDFSIM, for the detector simulation. The generated events have been processed through the simulation and reconstruction program, QFL' (Version: 3.59)+OFFLINE (Version: 7.12) packages. The purpose of the QFL', the CDF fast simulation package, is to provide a fast and reliable detector simulation for high statistics studies and acceptance calculations. QFL' parameterizes detector response rather than simulating the response from first principles; and, it produces higher level analysis banks rather than raw data banks, thus eliminating the need to run the complete reconstruction packages on the simulation output. However, QFL' tends to overestimate performance in the identification (ID) of leptons and doesn't incorporate luminosity or aging effects. Thus, a correction factor, f_{ID}^{μ} , is applied to both the signal and background MC samples. Also, the trigger efficiency is not included in the simulation. Therefore, we weight each event by trigger efficiency on the basis of p_T of muon in this analysis, since the trigger efficiency is a function of p_T (or p_T^{-1}) of the lepton. The method will be explained in detail when the data samples used for this analysis are introduced in Section 6.1. For muons, QFL' calculates two different isolations (ISO) based on track and calorimeter informations. Their definitions are introduced in Subsection 6.2.1. Both isolation quantities are kept in the muon bank (CMUO). This analysis uses isolation cuts, $ISO^{trk} < 4 \text{ GeV}/c$ and $ISO^{cal} < 4 \text{ GeV}$, for the candidate event selection. Therefore, those efficiencies should be corrected for MC samples.

	Efficiency (MC)	Efficiency (IA)	Efficiency (IB)	Scale factor (f_{ID}^μ)
Muon	0.977 ± 0.003	0.903 ± 0.025	0.929 ± 0.007	0.951 ± 0.008

Table 5.3: Identification efficiency for muons [38]

	Efficiency (MC)	Efficiency (IB)	Scale factor (f_{ISO}^μ)
Averaged over all jet multiplicities	0.9939 ± 0.0008	0.9918 ± 0.0017	0.9979 ± 0.0019
$N_{jet}^{0.4} = 0$	0.997 ± 0.001	0.998 ± 0.001	1.001 ± 0.001
$N_{jet}^{0.4} = 1$	0.992 ± 0.002	0.992 ± 0.004	1.000 ± 0.005
$N_{jet}^{0.4} \geq 2$	0.995 ± 0.004	1.000 ± 0.017	1.005 ± 0.018

Table 5.4: Efficiency of track isolation ($ISO^{trk} < 4 \text{ GeV}/c$) for muons. A cone size of 0.4 was used in this analysis [39].

	Efficiency (MC)	Efficiency (IB)	Scale factor (f_{ISO}^μ)
Averaged over all jet multiplicities	0.9835 ± 0.0017	0.9698 ± 0.0044	0.9861 ± 0.0048
$N_{jet}^{0.4} = 0$	0.989 ± 0.002	0.971 ± 0.005	0.982 ± 0.005
$N_{jet}^{0.4} = 1$	0.985 ± 0.004	0.966 ± 0.011	0.981 ± 0.012
$N_{jet}^{0.4} \geq 2$	0.980 ± 0.011	0.904 ± 0.041	0.922 ± 0.043

Table 5.5: Efficiency of calorimeter isolation ($ISO^{cal} < 4 \text{ GeV}$) for muons. A cone size of 0.4 was used in this analysis [39].

Chapter 6

Data Analysis

We carry out two analyses in parallel: the $Z \rightarrow \tau\tau$ calibration analysis and the $\bar{t}_1\bar{t}_1$ search as mentioned earlier in Chapter 3. Section 6.1 describes the data samples used for both analyses. Section 6.2 shows how prerequisite baseline samples including μ and τ_h are selected from the data samples. Then, specific requirements used to identify $Z \rightarrow \tau\tau$ and $\bar{t}_1\bar{t}_1$ events and to reject backgrounds are explained in Sections 6.3 and 6.4, respectively. All efficiencies related with event selection cuts are estimated using the MC signal samples of each case in Subsections 6.3.4 and 6.4.4. We also estimate signal acceptance in the same subsections. In Subsections 6.3.5 and 6.4.5, the results of data analysis are summarized and compared to those of MC simulation. All possible background sources to baseline $\mu + \tau_h$ samples have been examined in Section 5.1. The generation of background MC samples is also explained in the same section. In Subsections 6.3.6 and 6.4.6, we estimate the number of events expected from each source. All correction factors used for the normalization of the MC simulation have been enumerated in the previous chapter.

6.1 Data Samples

There were three runs during 1992–1996. The first run, Run IA, began in August, 1992 and ended in June, 1993 with an integrated luminosity of $18.8 \pm 0.7 \text{ pb}^{-1}$. After the end of Run IA, the SVX was replaced with the SVX' and the Data Acquisition (DAQ) system was upgraded. During Run IA, the SVX received about 15 krad of radiation and would not have lasted for a long time in the second run, Run IB, hence it had to be replaced to ensure good operation throughout this run. Run IB began February, 1994 and ended in July, 1995 with an integrated luminosity of $88.6 \pm 7.1 \text{ pb}^{-1}$. During Run IB, the improvements in the beam optics of the Tevatron allowed for higher instantaneous luminosity than Run IA. The mean instantaneous luminosity increased from $\mathcal{L} \sim 3.6 \times 10^{30} \text{ cm}^{-2}\text{s}^{-1}$ to $\mathcal{L} \sim 7.9 \times 10^{30} \text{ cm}^{-2}\text{s}^{-1}$. The peak instantaneous luminosity in Run IB was $\mathcal{L} \sim 2.5 \times 10^{31} \text{ cm}^{-2}\text{s}^{-1}$. This increase required certain triggers to be prescaled, broadened underlying event distributions and degraded the track momentum resolution. The third run, Run IC, began in November, 1995 and ended in February, 1996, but this data is not used for our analyses. Figure 6.1 shows the integrated luminosity acquired as a function of time.

There are very many events with various event types. Since the data are taken with a variety of event triggers (Section 4.2.4), the data were classified with the triggers that the event had passed. They are called “data samples.”

We use Run IA and Run IB low p_T inclusive muon data samples. The integrated luminosity of these data samples is $\sim (17.9 + 87.4 = 105.3) \text{ pb}^{-1}$. At L1, the relevant trigger was CMU_CMP_6PT0_HTDC*. This trigger requires a muon stub with $p_T > 6 \text{ GeV}/c$ in either the CMU or CMP. The p_T of

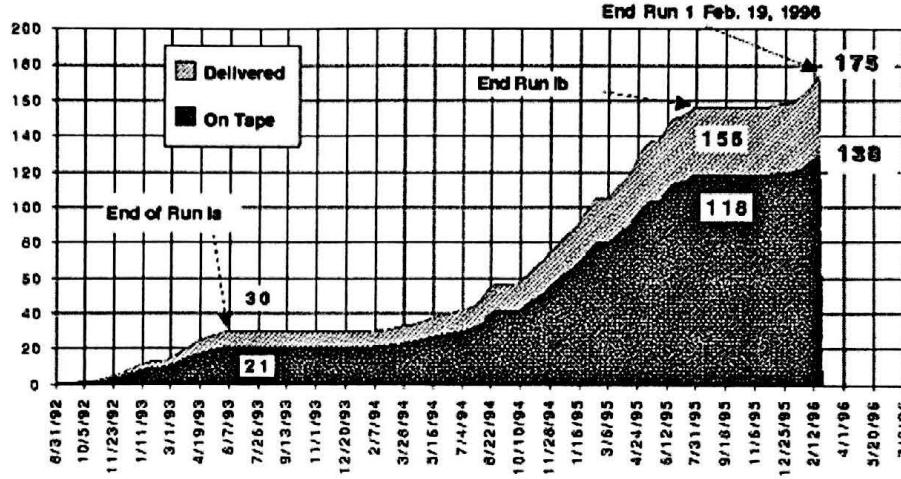


Figure 6.1: The CDF Run I experiment and its integrated luminosity

the muon track is measured by the arrival time of the drift electrons at the sense wires to determine the deflection angle due to the magnetic field. The L2 muon triggers use two-dimensional tracks found by Central Fast Tracker (CFT), a hardware track processor which uses fast timing information from the CTC to find high- p_T tracks. Tracks are found by comparing the hits to predetermined hit patterns for the range of p_T allowed by the CFT trigger threshold. The processor has eight p_T bins covering the range from 2.5 to 15 GeV/c. The L2 trigger extrapolates CFT tracks to the muon chambers and matches them to muon stubs that pass the L1 requirements. In Run 1A, the events were triggered by two different triggers, CMUP_CFT_6* and CMUP_CFT_9.2*, at L2. The CFT track of a muon candidate is required to have $p_T > 6.0$ GeV/c and $p_T > 9.2$ GeV/c respectively and its extrapolation to the muon chambers to be within 15° (5°) of a muon stub in azimuth in the early (late) part of Run 1A. In Run 1B, the events were triggered by

CMUP_CFT_7.5.5DEG* and CMUP_CFT_12.5DEG* at L2. The CFT track of a muon candidate is required to have $p_T > 7.5 \text{ GeV}/c$ and $p_T > 12.0 \text{ GeV}/c$ respectively and its extrapolation to the muon chambers to be within 5° . All the L2 triggers require a muon candidate to have muon stubs in the CMU and CMP. For muons with p_T between the thresholds of the two L2 triggers, the low p_T trigger was dynamically prescaled. The prescale factor in Run 1B is known to be 1.74. The events were triggered by MUO1_CMU_CMP_7PT5_V2* (MUOB_CMU_CMP_8*) in Run 1A (Run 1B) at L3.

The trigger efficiency for muons has been estimated as a function of p_T (p_T^{-1}). In the region of interest, $p_T \geq 10 \text{ GeV}/c$, the L1 and L3 trigger efficiencies are at their plateaus in Run 1A (Run 1B): 93.1% [32] at L1 and 98% (91%) [36, 37] at L3. As for two L2 triggers, they are not independent of each other, because an event accepted by the trigger with high p_T threshold should also be accepted by the trigger with low p_T threshold. The prescale factor of the low p_T trigger, f^{PS} , should be considered. Therefore, they are combined according to the following formula:

$$\epsilon_{L2}(p_T) = \epsilon_{high}(p_T) + \frac{\epsilon_{low}(p_T) - \epsilon_{high}(p_T)}{f^{PS}} \quad (6.1)$$

where ϵ_{L2} is the trigger efficiency at L2. ϵ_{low} and ϵ_{high} are the efficiencies of triggers with low and high thresholds. The parameterization for L2 triggers is given in several studies in CDF [33, 34, 35]. Figure 6.2 shows the total trigger efficiency curves in Run 1A and Run 1B. These curves include the efficiencies for L1, L2 and L3. Simulated samples are scaled event by event by f^{trig} , the trigger efficiency at a point of p_T , estimated from the following equation considering the integrated luminosity of each run:

$$f^{trig}(p_T) = \frac{17.9}{17.9 + 87.4} \epsilon_{Run\ 1A}(p_T) + \frac{87.4}{17.9 + 87.4} \epsilon_{Run\ 1B}(p_T) \quad (6.2)$$

where $\epsilon_{\text{Run IA}}$ and $\epsilon_{\text{Run IB}}$ are the total trigger efficiencies in Run IA and Run IB. MC correction factors have been explained in Section 5.3.

6.2 Baseline Event Selection

The muon and hadronic tau selections used to for the baseline $\mu + \tau_h$ samples are discussed in the present section.

Many analyses begin with a well-identified lepton (electron or muon) with $p_T \geq 20 \text{ GeV}/c$. However, we reduce the cut for muon selection to $10 \text{ GeV}/c$ because the muon from $\tau \rightarrow \mu\nu_\mu\nu_\tau$ has relatively lower p_T . We require a well-identified muon in the central region ($|\eta| < 0.6$) with $p_T(\mu) \equiv p_T^{\text{trk}} \geq 10 \text{ GeV}/c$. Any event is removed if it contains a second muon loosely identified with an OS charge, and forms an invariant mass in $76 \text{ GeV}/c^2 < M(\mu\mu)^{\text{trk}} < 106 \text{ GeV}/c^2$ by track information, as a possible candidate of $Z \rightarrow \mu\mu$. This decreases the probability that the second muon from the Z events is misidentified as 1-prong hadronic tau. The muons are required to be well-isolated based on calorimeter+track information. We require a hadronic tau in the central region ($|\eta| < 1.0$) with $p_T(\tau_h) \geq 15 \text{ GeV}/c$. We keep OS and LS $\mu + \tau_h$ pairs together. The signal always have OS. There are two major sources to the LS $\mu + \tau_h$ pairs: (1) QCD jets (gluon, light quarks, $b\bar{b}/c\bar{c}$) and (2) $W(\rightarrow \mu\nu) + \text{jets}$. Since both μ and τ_h from the QCD events (excluding $b\bar{b}/c\bar{c}$ production) are dominantly fake, we expect to have both OS and LS events at an equal rate. We subtract the QCD background in the OS events by using the LS events (see Section 5.1). It should be noted that there are some charge correlations between μ and τ_h for $W + \text{jets}$, $t\bar{t}$, $b\bar{b}/c\bar{c}$ and diboson productions.

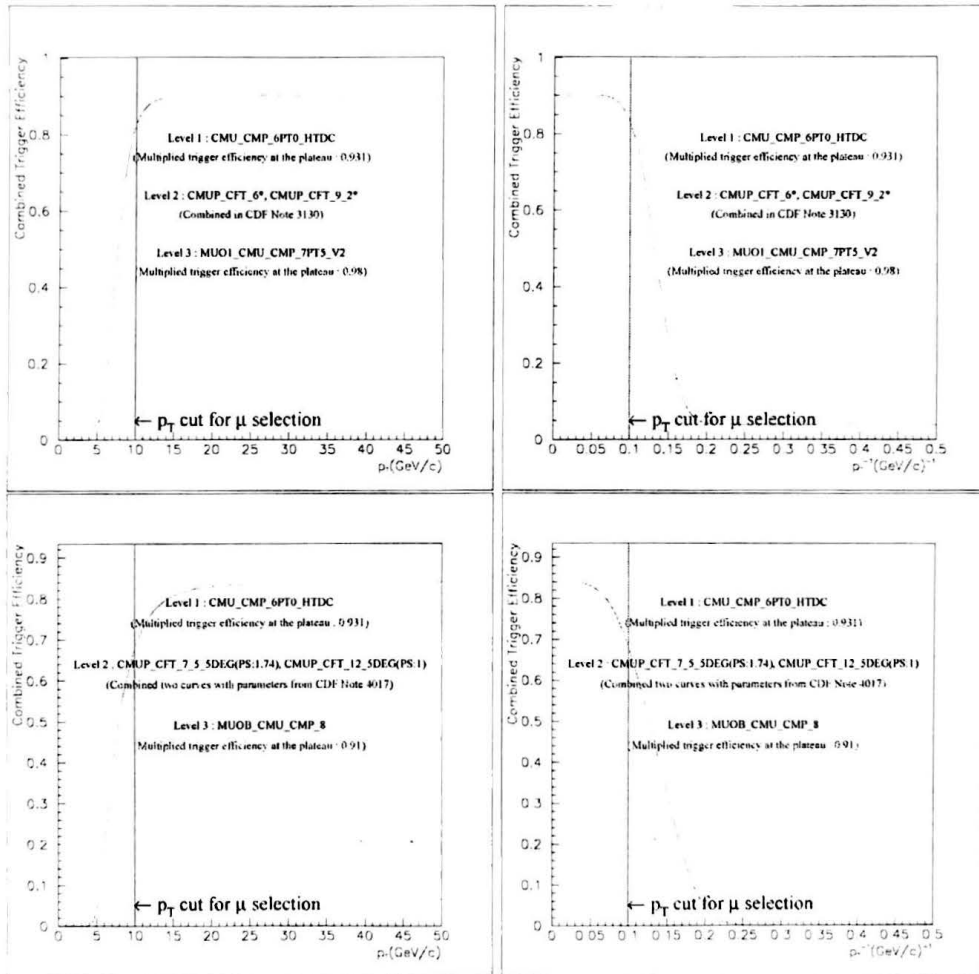


Figure 6.2: Trigger efficiency curves as a function of p_T (left) and p_T^{-1} (right) in Run IA (top) and Run IB (bottom)

$p_T(\mu) \equiv p_T^{trk} \geq 10 \text{ GeV}/c$ (with beam constraint fit), $ \eta < 0.6$
$E^{em} \leq 2.0 \text{ GeV}$, $E^{had} \leq 6.0 \text{ GeV}$, $E^{em} + E^{had} \geq 0.1 \text{ GeV}$
$ \Delta x \text{ (CMU)} \leq 2.0 \text{ cm}$ or $ \Delta x \text{ (CMP)} \leq 5.0 \text{ cm}$
$ d_0 \text{ (corrected)} \leq 0.3 \text{ cm}$
$ z_0^\mu - z_{vtx} \leq 5 \text{ cm}$
$ z_{vtx} \leq 60 \text{ cm}$ (vertex class ≥ 10)

Table 6.1: Muon identification quality cuts

6.2.1 Muon Selection

Muons are reconstructed and identified using the information from the CTC, electromagnetic and hadronic calorimeters and muon chambers. We require a well-identified muon with $p_T(\mu) \equiv p_T^{trk} \geq 10 \text{ GeV}/c$ in the central region of $|\eta| < 0.6$. The momentum of muons is measured by constraining the CTC track to the average beam position: beam constraint fit. The primary backgrounds are from secondary particles in charged hadron showers which “punch through” the calorimeter and produce tracks in the muon chambers, and cosmic rays. To reject the charged hadron background, the muon is required to have an energy deposition in the calorimeters consistent with a Minimum Ionizing Particle (MIP). Backgrounds from cosmic rays are rejected by requiring that the track extrapolates back in r - ϕ plane to within 0.3 cm of the beamline and that it is in the r - z plane within 5 cm of the primary vertex at $r = 0$. The muon identification criteria are summarized in Table 6.1.

Since the second muon from $Z \rightarrow \mu\mu$ can be misidentified as 1-prong hadronic tau, we remove the Z events by using the track information. Table 6.2 shows the cuts applied to the second muons and the mass window of Z removal.

$p_T(\mu) \equiv p_T^{trk} > 10 \text{ GeV}/c$ (second muon)
$E^{em} < 5 \text{ GeV}, E^{had} < 10 \text{ GeV}$
Opposite sign charge
$76 \text{ GeV}/c^2 < M(\mu\mu)^{trk} < 106 \text{ GeV}/c^2$

Table 6.2: Cuts for the second muon from $Z \rightarrow \mu\mu$

We consider the calorimeter and track isolations. The calorimeter isolation, ISO^{cal} , is defined as E_T in a cone of $\Delta R \equiv \sqrt{(\Delta\eta)^2 + (\Delta\phi)^2} = 0.4$ around the muon, excluding the E_T of muon. It is required to be less than 4 GeV:

$$ISO^{cal} \equiv \sum_{\Delta R < 0.4} E_T^{cal,i} - E_T^{clu,\mu} < 4 \text{ GeV} \quad (6.3)$$

where $E_T^{cal,i} \equiv E_T^{em,i} + E_T^{had,i}$ represents the energy deposit on the i -th calorimeter tower and $E_T^{clu,\mu}$ is the cluster energy deposited on the calorimeter by the muon. The tracking isolation, ISO^{trk} , defined in similar way for tracks in the CTC, is also required to be less than 4 GeV/ c :

$$ISO^{trk} \equiv \sum_{\Delta R < 0.4} p_T^{trk} - p_T^{trk,\mu} < 4 \text{ GeV}/c \quad (6.4)$$

The missing- E_T (\cancel{E}_T) of the event is corrected for the muon energy. \cancel{E}_T is the energy imbalance in the directions transverse to the beam direction using the raw energy deposited in calorimeter towers with $|\eta| < 3.6$.

6.2.2 Tau Selection

At $p\bar{p}$ colliders, various processes like W , Z and top quark productions involve high- p_T electrons and muons. CDF has succeeded in detecting electrons and muons from those events. On the other hand, the tau is a much more difficult

signal, since it predominantly decays into charged and neutral pions and suffers from large backgrounds from jet production. Top quark pair-production in the decay channel containing a tau has been studied in CDF [64]. Searches for the Higgs boson and leptoquark in the decay channel containing one or more taus also has been considered [65, 66]. Searches with tau are sensitive to new physics and important for precision measurements and the confirmation of lepton universality.

Taus promptly decay to the lighter leptons or to hadronic jets. However, we only consider the hadronic decay of tau, since the leptons from tau decay cannot be distinguished experimentally from prompt ones. Hadronic tau is identified by an algorithm which relies on track isolation and π^0 reconstruction. The algorithm begins with the calorimeter cluster with $E_T > 4$ GeV in $|\eta| < 1.0$ and requires: (1) the number of tracks with $p_T > 1$ GeV/ c in the 10° cone centered on the line connecting the calorimeter centroid and the event vertex, $N_{track}^{10^\circ}$, to be one or three (see Figure 6.3). The charge of the hadronic tau is defined as a sum of track charges; (2) the track isolation, I_{track} , defined as scalar sum of p_T of all tracks in a cone of $\Delta R = 0.4$ around the cluster center, excluding tracks in the 10° cone, to be less than 1 GeV/ c ; (3) the number of π^0 's to be less than three, where $\pi^0 \rightarrow \gamma\gamma$ candidates are identified in the electromagnetic calorimeter; (4) $p_T(\tau_h) \geq 15$ GeV/ c , where $p_T(\tau_h)$ is defined as the sum of the p_T of track plus E_T of identified π^0 's, in the 10° cone. See Equation (6.5);

$$p_T(\tau_h) \equiv p_T^{trk+\pi^0} \equiv \sum_{10^\circ cone} p_T^{trk} + E_T^{em(\pi^0)} \geq 15 \text{ GeV}/c \quad (6.5)$$

(5) the invariant mass, $M(\tau_h)$, reconstructed from tracks and π^0 's to be less than 1.8 GeV/ c^2 ; (6) clusters being consistent with an electron or a muon to

be rejected. The identification quality cuts for hadronic tau are summarized in Table 6.3.

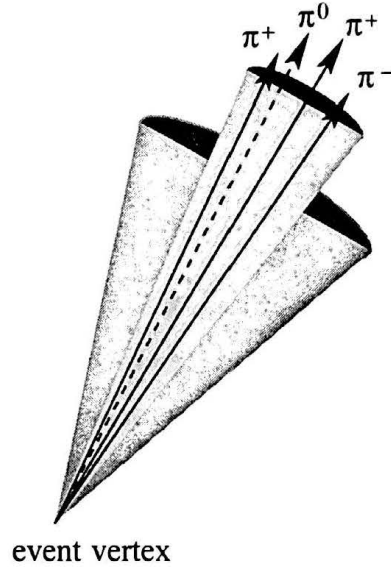


Figure 6.3: Hadronic tau identification

We extract 163 OS and 82 LS $\mu + \tau_h$ events from the data as baseline samples. We check several kinematic distributions with the baseline samples. They support the hypothesis of $Z \rightarrow \tau\tau$ for the data (see Figures 6.4 and 6.5). We also compare the data to simulation. The sources for the $\mu + \tau_h$ pairs in the baseline samples are $Z \rightarrow \tau\tau$, $W + \text{jet}$ and QCD events (see Figures 6.6 and 6.7).

Number of tracks	1-prong or 3-prong ($ \sum_i Q_i = 1$) in 10° cone
Number of π^0 's	< 3
E/p	$0.5 < \frac{E_T^{clu}}{p_T^{trk+\pi^0}} < 2.0$ (1-prong) $0.5 < \frac{E_T^{clu}}{p_T^{trk+\pi^0}} < 1.5$ (3-prong)
Sliding RMS cluster width	$\sigma_{cl} < 0.11 - 0.025 \times E_T^{clu}/100$ (1-prong) $\sigma_{cl} < 0.13 - 0.034 \times E_T^{clu}/100$ (3-prong)
Invariant Mass	$M(\tau_h) \equiv M(trk, \pi^0) < 1.8 \text{ GeV}/c^2$
Isolation	$I^{trk} < 1 \text{ GeV}/c$
Electron removal	Reject clusters with (a) 1-prong with $E_T^{clu}/p_T^{trk} < 4$, EM fraction > 0.9 or (b) EM fraction > 0.95
Muon removal	Reject clusters with (a) $E_T^{clu} < 8 \text{ GeV}$, $0.05 < E^{em} < 2 \text{ GeV}$, $0.5 < E^{had} < 5 \text{ GeV}$ or (b) a muon stub with $ \phi_r - \phi_{stub} < 15^\circ$ as muon

Table 6.3: Hadronic tau identification quality cuts

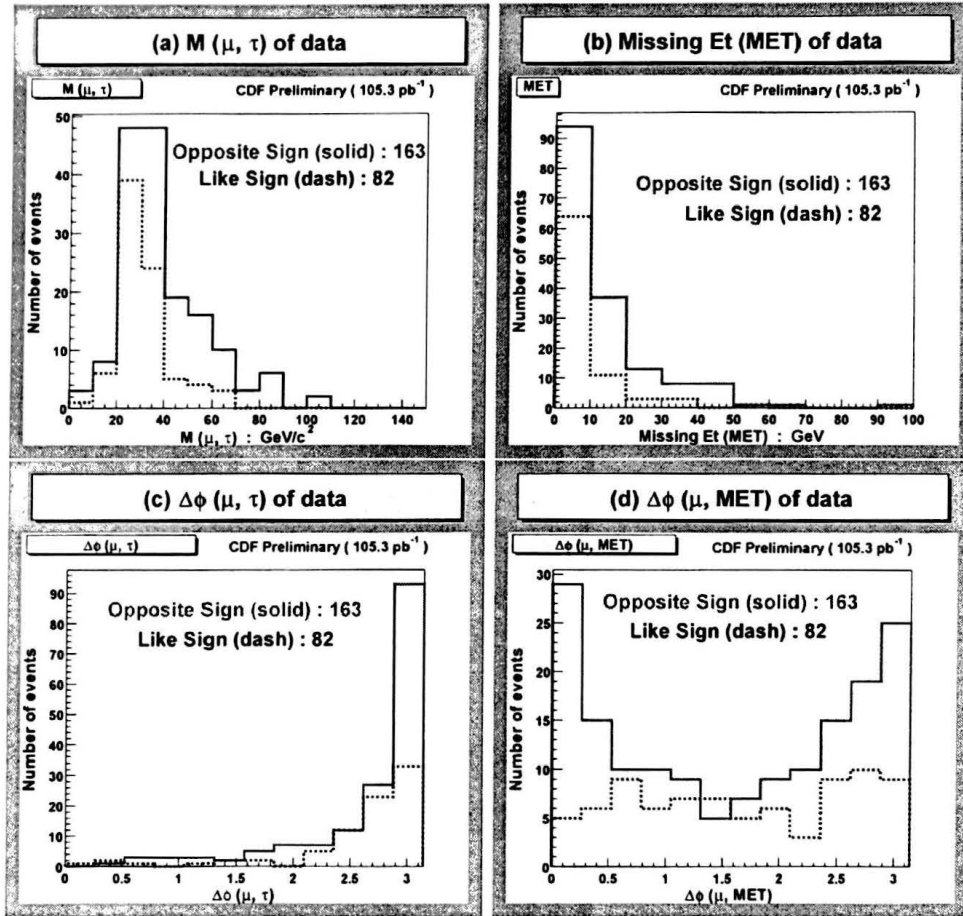


Figure 6.4: Distributions of (a) $M(\mu, \tau_h)$, (b) \cancel{E}_T , (c) $\Delta\phi(\mu, \tau_h)$ and (d) $\Delta\phi(\mu, \cancel{E}_T)$ for 163 OS and 82 LS $\mu + \tau_h$ events from the data sample.

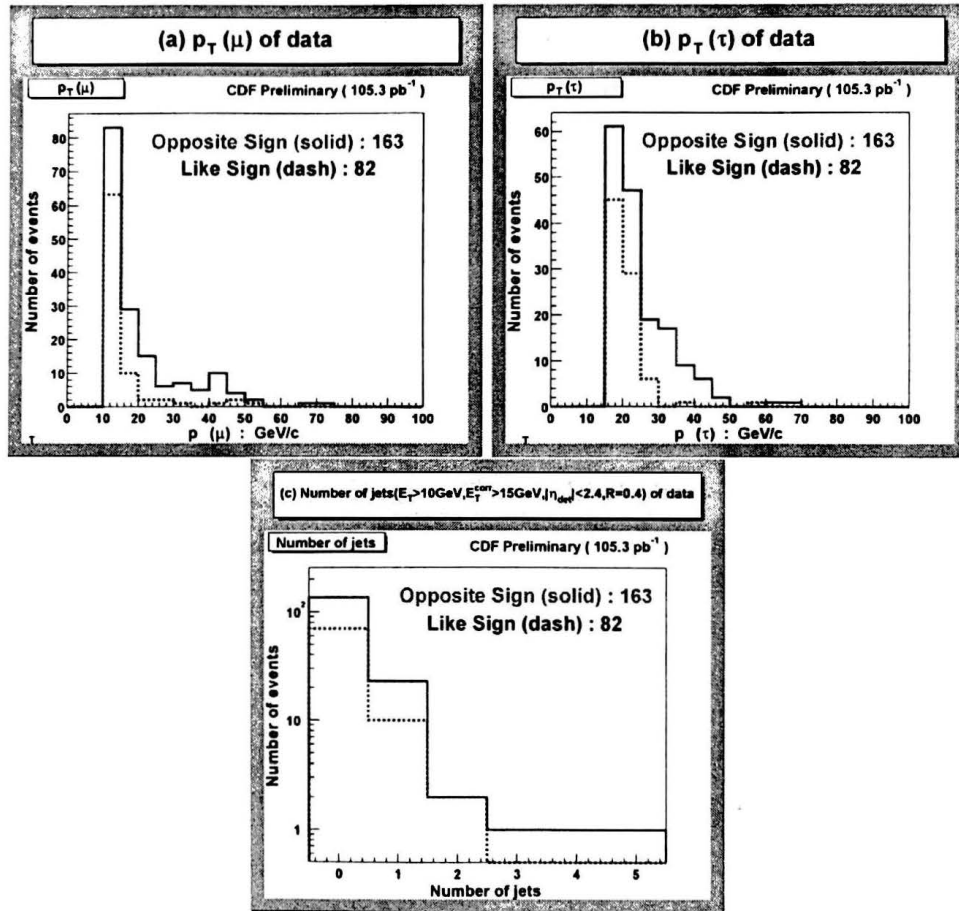


Figure 6.5: Distributions of (a) $p_T(\mu)$, (b) $p_T(\tau_h)$ and (c) the number of jets for 163 OS and 82 LS $\mu + \tau_h$ events from the data sample.

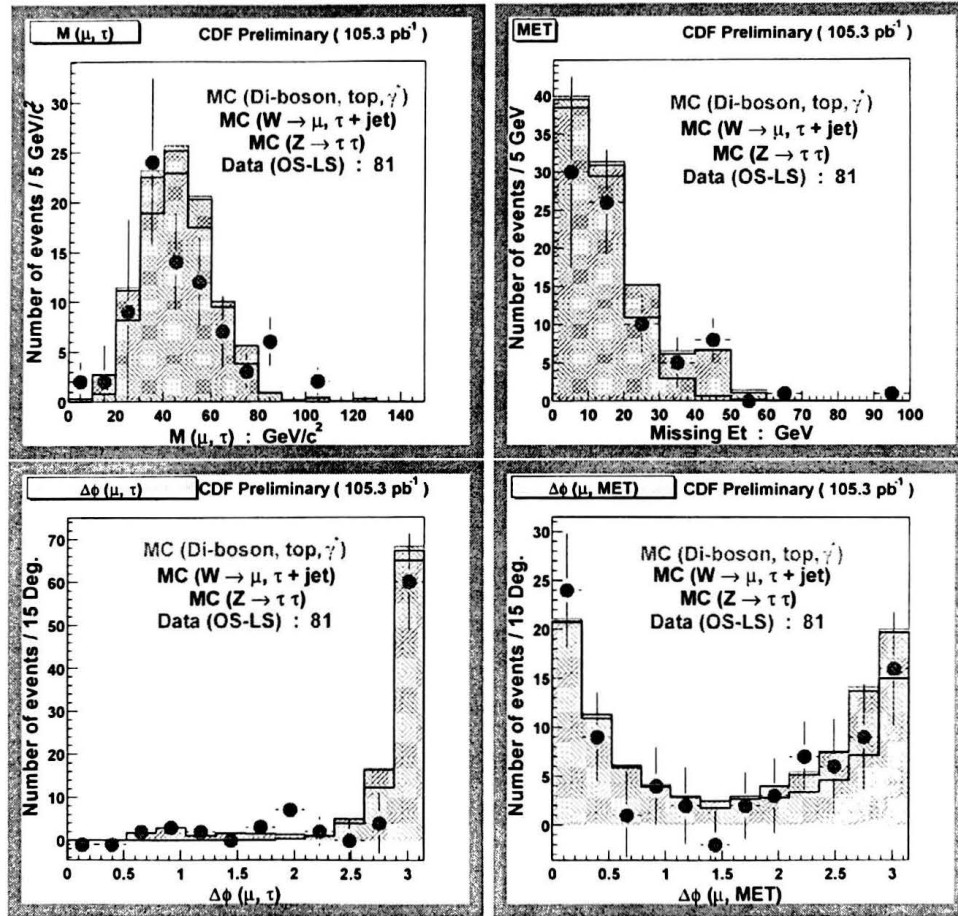


Figure 6.6: Distributions of (a) $M(\mu, \tau_h)$, (b) \cancel{E}_T , (c) $\Delta\phi(\mu, \tau_h)$ and (d) $\Delta\phi(\mu, \cancel{E}_T)$ for OS-LS events in the data and simulated samples.

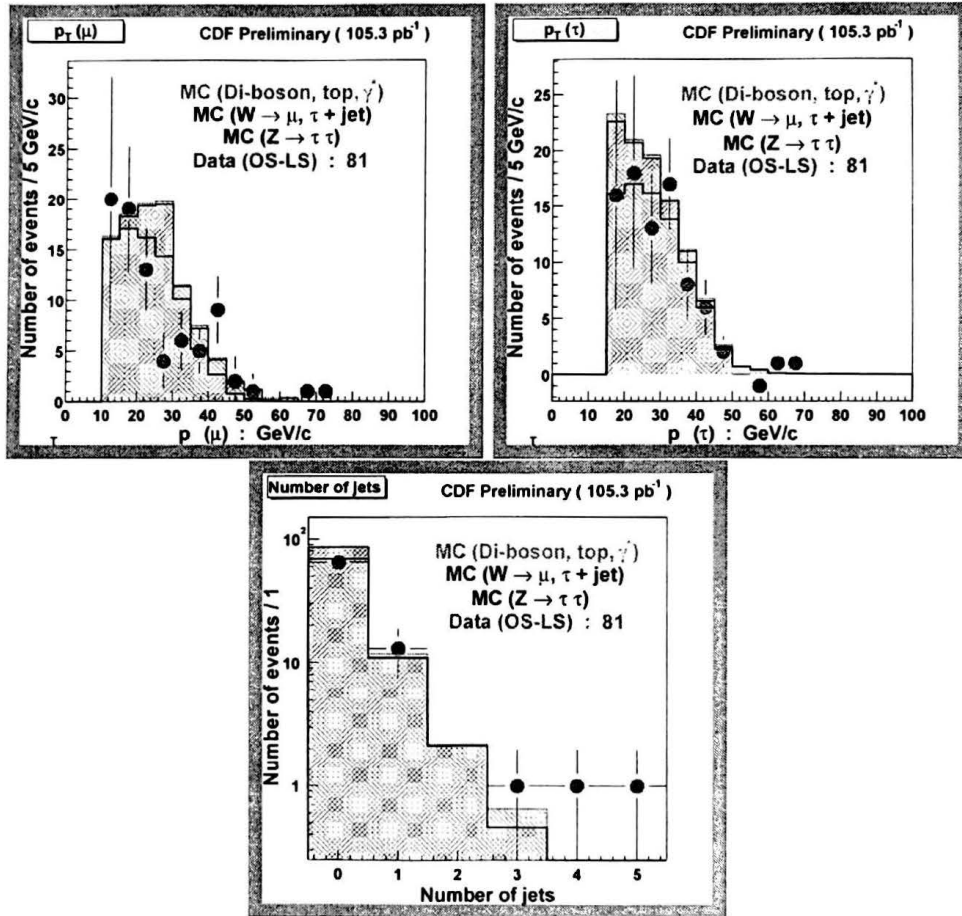


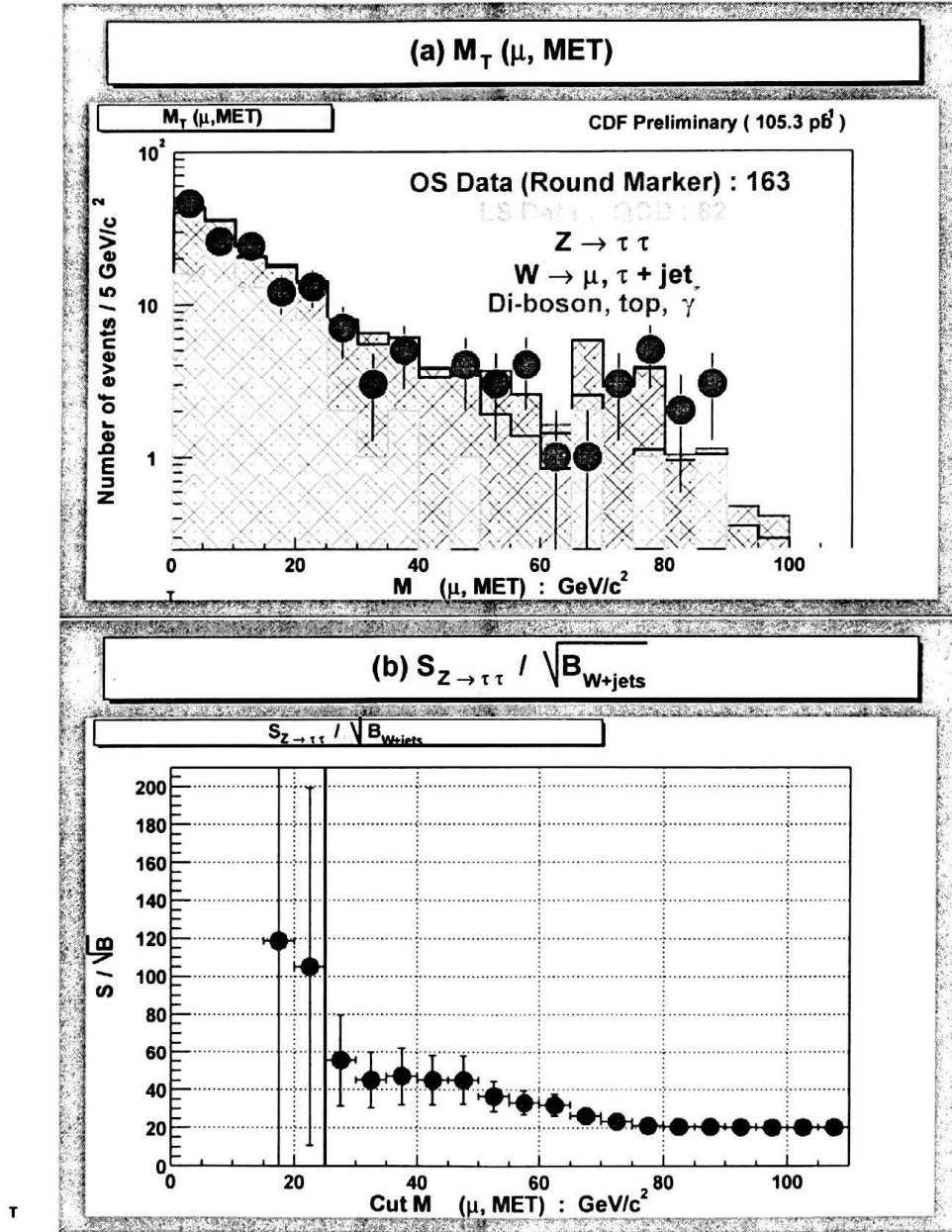
Figure 6.7: Distributions of (a) $p_T(\mu)$, (b) $p_T(\tau_h)$ and (c) the number of jets for OS-LS events in the data and simulated samples.

6.3 $Z \rightarrow \tau\tau$ Analysis

The major backgrounds of $Z \rightarrow \tau\tau$ events are W +jet and QCD events. We begin with the baseline $\mu + \tau_h$ samples and devise two additional cuts to reject the backgrounds and obtain the $Z \rightarrow \tau\tau$ samples with high purity. The cut values are optimized to maximize the significance of $Z \rightarrow \tau\tau$ events against each background source. We remove the W events in OS and LS samples using a cut on the transverse mass of the muon and \cancel{E}_T system, $M_T(\mu, \cancel{E}_T)$, which is insensitive to the charge correlation. Next, we apply a cut on the transverse momentum of the muon and \cancel{E}_T system, $p_T(\mu, \cancel{E}_T)$, chosen by the study of the LS events which reflect the QCD background in OS sample. Finally, we exclude the $Z \rightarrow \tau\tau$ candidates containing one or more jets, since only $Z(\rightarrow \tau\tau) + 0$ -jet events are used for calibration.

6.3.1 W Event Rejection

Figure 6.8 (top) shows the transverse mass distribution of the muon and \cancel{E}_T system, $M_T(\mu, \cancel{E}_T)$, in the data and simulated samples. Starting at the QCD background represented by the LS events, $Z \rightarrow \tau\tau$ signal, $W(\rightarrow \mu\nu \text{ or } \tau\nu) + \text{jet}$ and the other background ($\gamma^* \rightarrow \tau\tau$, $WW/WZ/ZZ$ and $t\bar{t}$) events have been accumulated on the top. We clearly observe the “ W ”-like events in the relatively high $M_T(\mu, \cancel{E}_T)$ region. Figure 6.8 (bottom) shows the distribution of significance, $S_{Z \rightarrow \tau\tau} / \sqrt{B_{W+\text{jet}}}$, which is defined as the ratio of expected number of signal events to the square root of the expected number of background events, where $S_{Z \rightarrow \tau\tau}$ and $B_{W+\text{jet}}$ are obtained from the simulated samples. We require $M_T(\mu, \cancel{E}_T) \leq 25 \text{ GeV}/c^2$. As a result of the first cut, 121 OS and 72 LS events are retained in the data sample (see Table 6.5 in Subsection 6.3.5).

Figure 6.8: Distributions of $M_T(\mu, \cancel{E}_T)$ (top) and $S_{Z \rightarrow \tau\tau} / \sqrt{B_{W+\text{jet}}}$ (bottom).

6.3.2 QCD Event Rejection

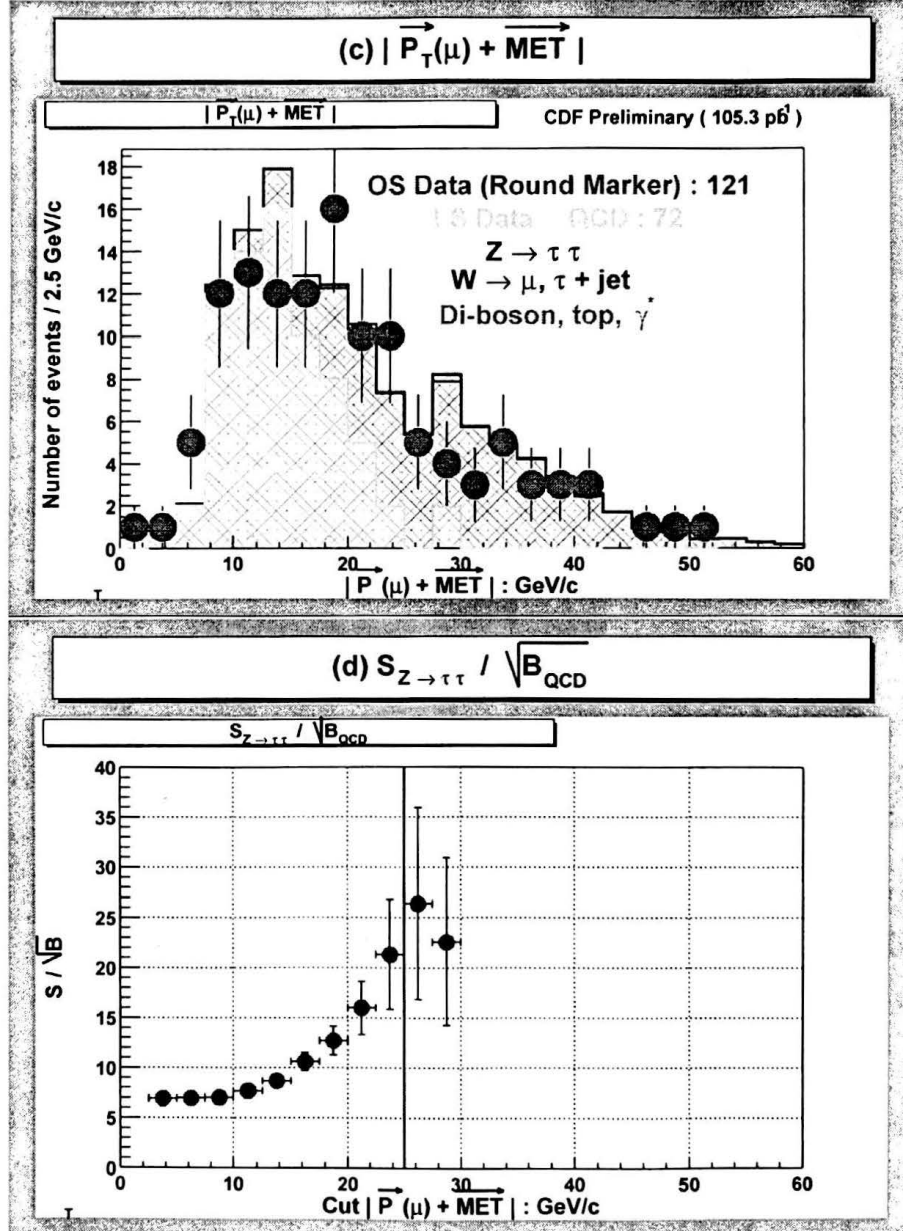
After applying the W rejection cut, the QCD background dominates the LS events. We apply another cut on the transverse momentum of the muon and \cancel{E}_T system, $p_T(\mu, \cancel{E}_T) \equiv |\vec{p}_T(\mu) + \vec{\cancel{E}}_T|$. Figure 6.9 (top) shows the distribution of $p_T(\mu, \cancel{E}_T)$ in the data and simulated samples after applying the W rejection cut. Figure 6.9 (bottom) shows the distribution of significance, $S_{Z \rightarrow \tau\tau} / \sqrt{B_{QCD}}$, where $S_{Z \rightarrow \tau\tau}$ is obtained from the simulated sample and B_{QCD} is obtained from the LS events in the data. We require $p_T(\mu, \cancel{E}_T) \geq 25 \text{ GeV}/c$. As a result of the first and second cuts, 29 OS and 2 LS events are retained in the data sample (see Table 6.5 in Subsection 6.3.5).

6.3.3 Jet Veto

We apply a “jet veto” cut to reject the Z events associated with any jet, since:

- (1) We want to use only $Z(\rightarrow \tau\tau) + 0\text{-jet}$ events for calibration. The majority of the $Z \rightarrow \tau\tau$ events is expected to have 0-jet by the CDF measurement [41] (see Section 3.4);
- (2) it is possible that the $Z \rightarrow \tau\tau$ candidates selected according to the previous procedures also include $\tilde{t}_1 \bar{\tilde{t}}_1$ events. Therefore, we separate $Z \rightarrow \tau\tau$ and $\tilde{t}_1 \bar{\tilde{t}}_1$ events by the jet multiplicity of the events, since the $\tilde{t}_1 \bar{\tilde{t}}_1$ events are expected to have two or more jets (see Subsection 6.4.3).

A jet is reconstructed in the calorimeter using a cone algorithm with the cone radius of $R \equiv \sqrt{(\Delta\eta)^2 + (\Delta\phi)^2} = 0.4$. The jet energy is calculated by the raw energy deposition in calorimeter towers: E_T^{raw} . Tower momenta are calculated from tower energies with the assumption that they are energies of particles with zero mass that originated from the reconstructed primary vertex and are located at the center of the tower. The raw measurements are corrected

Figure 6.9: Distributions of $|\vec{p}_T(\mu) + \vec{E}_T^{\text{miss}}|$ (top) and $S_{Z \rightarrow \tau\tau} / \sqrt{B_{QCD}}$ (bottom).

for non-instrumented regions, non-linear response of the calorimeter, multiple interactions at high luminosity and another effects which account for detector and reconstruction effects: “flavor-independent” jet energy corrections.

We count the number of jets which have $E_T^{raw} > 10$ GeV and $E_T^{corr} > 15$ GeV in $|\eta| < 2.4$, and are well separated from muon and hadronic tau in η - ϕ space:

$$\Delta R(\mu, jet) > 0.4, \Delta R(\tau_h, jet) > 0.4 \quad (6.6)$$

where the separation is defined as $\Delta R \equiv \sqrt{(\Delta\eta)^2 + (\Delta\phi)^2}$.

6.3.4 Efficiencies and Acceptance Estimations

The efficiency of each $Z \rightarrow \tau\tau$ selection cut is estimated with the signal sample simulated by ISAJET. Table 6.4 summarizes the cut efficiencies with signal acceptance, A_Z^{MC} , and trigger efficiency, ϵ_Z^{trg} (see Section 3.4).

	Cut efficiency (%)	Cumulative efficiency (%)
Muon selection	9.82	9.82
$Z \rightarrow \mu\mu$ veto	100	9.82
Muon isolation	98.05	9.63
Hadronic tau selection	19.84	1.91
$M_T(\mu, \cancel{E}_T) \leq 25 \text{ GeV}/c^2$	71.35	1.36
$p_T(\mu, \cancel{E}_T) \geq 25 \text{ GeV}/c$	63.31	0.86
Signal acceptance (%)	$A_Z^{MC} = 0.86 \pm 0.02(\text{stat})$	
Trigger efficiency (%)	$\epsilon_Z^{trg} = 83.0$	

Table 6.4: Cut efficiencies and signal acceptance of $Z \rightarrow \tau\tau$ analysis

6.3.5 Summary of Data Analysis

Table 6.5 shows the event reduction by each selection cut in the data sample. It is compared to the simulated $Z \rightarrow \tau\tau$ and $W + \text{jet}$ samples in Table 6.6. We calculate the expected number of $Z(\rightarrow \tau\tau) + 0\text{-jet}$ events by multiplying the ratio, $R(0 - \text{jet})$ (see Section 3.4), to the total. Therefore, the expected number of $Z(\rightarrow \tau\tau) + 0\text{-jet}$ events is calculated as follows:

$$\begin{aligned}
 N_Z^{\text{expected}} &= \sigma \cdot B(Z \rightarrow \tau\tau) \cdot R(0 - \text{jet}) \cdot \int \mathcal{L} dt \cdot B_{\mu\tau_h} \cdot A_Z^{MC} \cdot \varepsilon_Z^{\text{trg}} \cdot f_{ID}^\mu \cdot f_{ISO}^\mu \\
 &= 30.1 \pm 0.5(\text{stat})
 \end{aligned}
 \tag{6.7}$$

	OS	LS	OS-LS
Muon Selection	511550		
$Z \rightarrow \mu\mu$ veto	510290		
Muon isolation	249050		
Hadronic tau selection	163	82	81
$M_T(\mu, \cancel{E}_T) \leq 25 \text{ GeV}/c^2$	121	72	49
$p_T(\mu, \cancel{E}_T) \geq 25 \text{ GeV}/c$	29	2	27
Jet veto	23	2	$N_Z^{\text{obs}} = 21$

Table 6.5: $Z(\rightarrow \tau\tau) + 0\text{-jet}$ events from the data sample

6.3.6 Background Estimation

Table 6.7 shows the number of events remained after $Z(\rightarrow \tau\tau) + 0\text{-jet}$ selection in the data and simulated samples. The expected number of $Z \rightarrow \tau\tau$ events is $30.0 \pm 0.5(\text{stat})$ from the MC simulation. The number of OS events

Cut	$Z(\rightarrow \tau\tau)$		$W(\rightarrow \mu\nu)+\text{jet}$		Data	
	OS	LS	OS	LS	OS	LS
Baseline $\mu + \tau_h$ samples	83.1	0.5	23.2	7.0	163	82
$M_T(\mu, \cancel{E}_T) \leq 25 \text{ GeV}/c^2$	58.6	0.2	0.3	0.6	121	72
$p_T(\mu, \cancel{E}_T) \geq 25 \text{ GeV}/c$	37.3	0.2	0.3	0.3	29	2
Jet veto	30.1	0.1	0.3	0.0	23	2

Table 6.6: Number of events in the data and background samples after each cut ($Z \rightarrow \tau\tau$ analysis)

subtracted with backgrounds, $N_Z^{obs} - N_Z^{BG}$, is $(23 - 2) - (0.4 + 0.3 + 0.2) = 20.1 \pm 5.0(\text{stat}) \pm 0.2(\text{sys})$.

Process	OS	LS	OS-LS
$Z \rightarrow \tau\tau$	30.1	0.1	$30.0 \pm 0.5(\text{stat})$
$\gamma^* \rightarrow \tau\tau$	0.4	0.0	$0.4 \pm 0.1(\text{stat}) \pm 0.1(\text{sys})$
$W(\rightarrow \mu\nu)+\text{jets}$	0.3	0.0	$0.3 \pm 0.3 \pm 0.1$
$W(\rightarrow \tau\nu)+\text{jets}$	0.2	0.0	$0.2 \pm 0.2 \pm 0.1$
Doboson ($WW/WZ/ZZ$), $t\bar{t}$	0.0	0.0	negligible
Data	23	2	21

Table 6.7: Summary of yields of $\mu + \tau_h$ events in the data and simulated samples after $Z(\rightarrow \tau\tau) + 0\text{-jet}$ selection.

We check kinematic distributions after $Z(\rightarrow \tau\tau) + 0\text{-jet}$ selection. Figure 6.10 shows the kinematic distributions after OS-LS subtraction in the data and simulated samples. We observe a good agreement between the data and MC simulation.

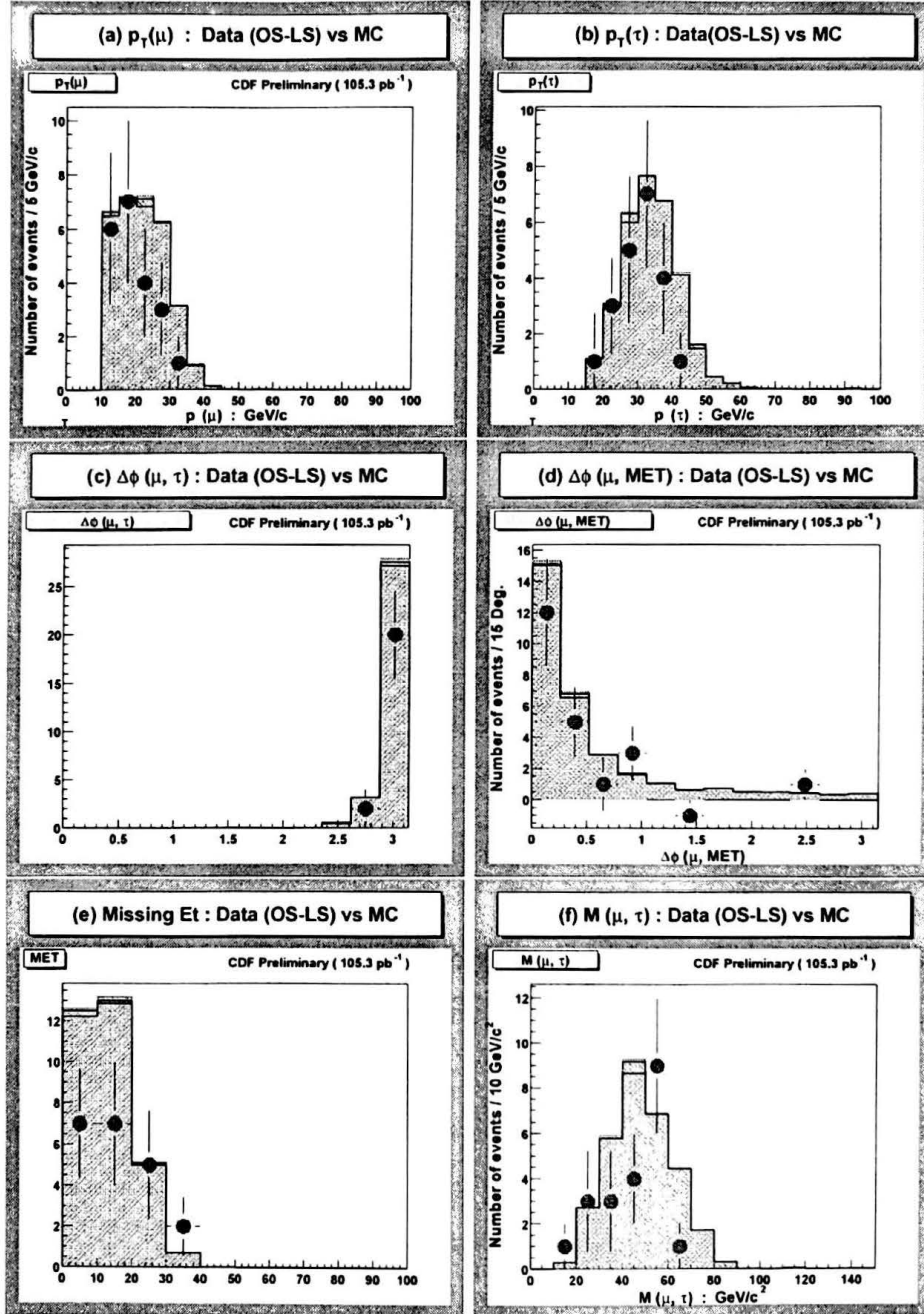


Figure 6.10: Distributions of (a) $p_T(\mu)$, (b) $p_T(\tau_h)$, (c) $\Delta\phi(\mu, \tau_h)$, (d) $\Delta\phi(\mu, \cancel{E}_T)$, (e) \cancel{E}_T and (f) $M(\mu, \tau_h)$ in the data and simulated samples after $Z(\rightarrow \tau\tau) + 0$ -jet selection.

6.4 $\tilde{t}_1\bar{\tilde{t}}_1$ Analysis

The major backgrounds of $\tilde{t}_1\bar{\tilde{t}}_1$ events are $W + 3\text{-jet}$, QCD and $Z(\rightarrow \tau\tau) + 2\text{-jet}$ events. We begin with the same baseline $\mu + \tau_h$ samples as $Z \rightarrow \tau\tau$ analysis and devise three additional cuts to reject each background. We remove the W events in OS and LS samples by the same cut used in $Z \rightarrow \tau\tau$ analysis, the cut on the transverse mass of the muon and \cancel{E}_T system, but with a different cut value. Next, we apply a cut on the scalar sum of the transverse momentum of muon, transverse momentum of hadronic tau and \cancel{E}_T , $H_T(\mu, \tau_h, \cancel{E}_T)$, to remove the QCD events. The cut values are optimized to maximize the significance of $\tilde{t}_1\bar{\tilde{t}}_1$ signal against each background source. Finally, we require the $\tilde{t}_1\bar{\tilde{t}}_1$ candidate events to have two or more jets. This cut is devised mainly for $Z \rightarrow \tau\tau$ event rejection (see Subsection 6.3.3).

6.4.1 W Event Rejection

We remove W events from both OS and LS samples by applying the cut on $M_T(\mu, \cancel{E}_T)$. Figure 6.11 shows: (1) the $M_T(\mu, \cancel{E}_T)$ distribution in the data and simulated samples (top). The data is taken from the baseline $\mu + \tau_h$ samples and no additional cut has been applied yet; (2) the $M_T(\mu, \cancel{E}_T)$ distribution of $\tilde{t}_1\bar{\tilde{t}}_1$ and W events from simulated samples (middle), when the signal events have $M_{\tilde{t}_1} = 100 \text{ GeV}/c^2$; and, (3) the distribution of significance (bottom), $\varepsilon_{\tilde{t}_1\bar{\tilde{t}}_1 \rightarrow \tau\tau b\bar{b}}/\sqrt{\varepsilon_{W+jets}}$, which is defined as the ratio of signal efficiency to square root of background efficiency, as a function of $M_T(\mu, \cancel{E}_T)$, where $\varepsilon_{\tilde{t}_1\bar{\tilde{t}}_1 \rightarrow \tau\tau b\bar{b}}$ and ε_{W+jets} are obtained from the simulated samples. We require $M_T(\mu, \cancel{E}_T) \leq 35 \text{ GeV}/c^2$. As a result of the first cut, we retain 131 OS and 75 LS events in the data samples (see Table 6.12 in Subsection 6.4.5).

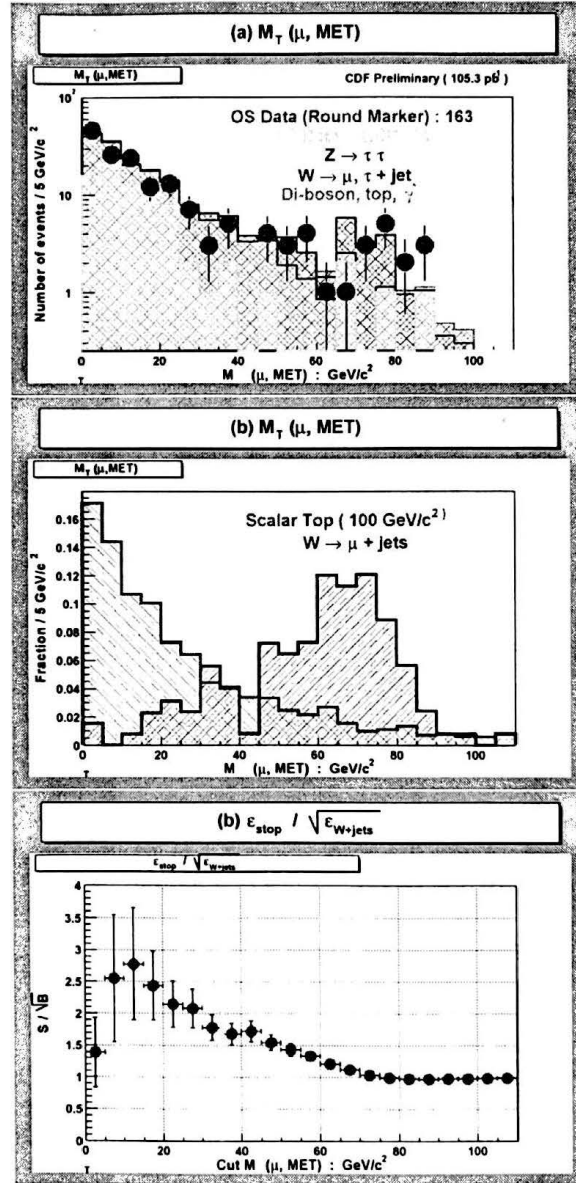


Figure 6.11: Distributions of $M_T(\mu, \cancel{E}_T)$ (top), $M_T(\mu, \cancel{E}_T)$ for $\tilde{t}_1\tilde{t}_1^*$ and $W + \text{jet}$ events (middle) and $\epsilon_{\tilde{t}_1\tilde{t}_1^* \rightarrow \tau\tau b\bar{b}} / \sqrt{\epsilon_{W+\text{jets}}}$ (bottom)

6.4.2 QCD Event Rejection

We apply a cut on the scalar sum of the transverse momentum of muon, transverse momentum of hadronic tau and \cancel{E}_T , $H_T(\mu, \tau_h, \cancel{E}_T) = p_T(\mu) + p_T(\tau_h) + \cancel{E}_T$, in order to remove the QCD events which are dominant after the $M_T(\mu, \cancel{E}_T)$ cut. Figure 6.12 shows: (1) the $H_T(\mu, \tau_h, \cancel{E}_T)$ distribution in the data and simulated samples (top), after applying the W rejection cut; (2) the $H_T(\mu, \tau_h, \cancel{E}_T)$ distribution of $\tilde{t}_1 \bar{\tilde{t}}_1$ and QCD background represented by the LS data (middle); and, (3) the distribution of significance (top), $\varepsilon_{\tilde{t}_1 \bar{\tilde{t}}_1 \rightarrow \tau\tau b\bar{b}} / \sqrt{\varepsilon_{QCD}}$, as a function of $H_T(\mu, \tau_h, \cancel{E}_T)$, where $\varepsilon_{\tilde{t}_1 \bar{\tilde{t}}_1 \rightarrow \tau\tau b\bar{b}}$ is obtained from simulated sample and ε_{QCD} is obtained from the LS events in the data. We require $H_T(\mu, \tau_h, \cancel{E}_T) \geq 75 \text{ GeV}/c^2$. As a result, we retain only 8 OS events in the data sample (see Table 6.12 in Subsection 6.4.5).

6.4.3 Jet Requirement

After the two cuts described above, the retained $\mu + \tau_h$ events dominantly result from $Z \rightarrow \tau\tau$ process. Therefore, we apply a cut on the number of jets, N_{jet} . The definition of jet is the same as that of $Z \rightarrow \tau\tau$ analysis. We require two or more jets well separated from muon and hadronic tau in η - ϕ space with $E_T^{raw} > 10 \text{ GeV}$ and $E_T^{corr} > 15 \text{ GeV}$ in $|\eta| < 2.4$: $N_{jet} \geq 2$. Figure 6.13 shows the distribution of N_{jet} for the signal and $Z \rightarrow \tau\tau$ events. We don't have any candidate events after all three cuts (see Table 6.12 in Subsection 6.4.5).

6.4.4 Efficiencies and Acceptance Estimations

The efficiency of each $\tilde{t}_1 \bar{\tilde{t}}_1$ selection cut is estimated with signal MC samples which have been simulated at the eight different mass points of the scalar top

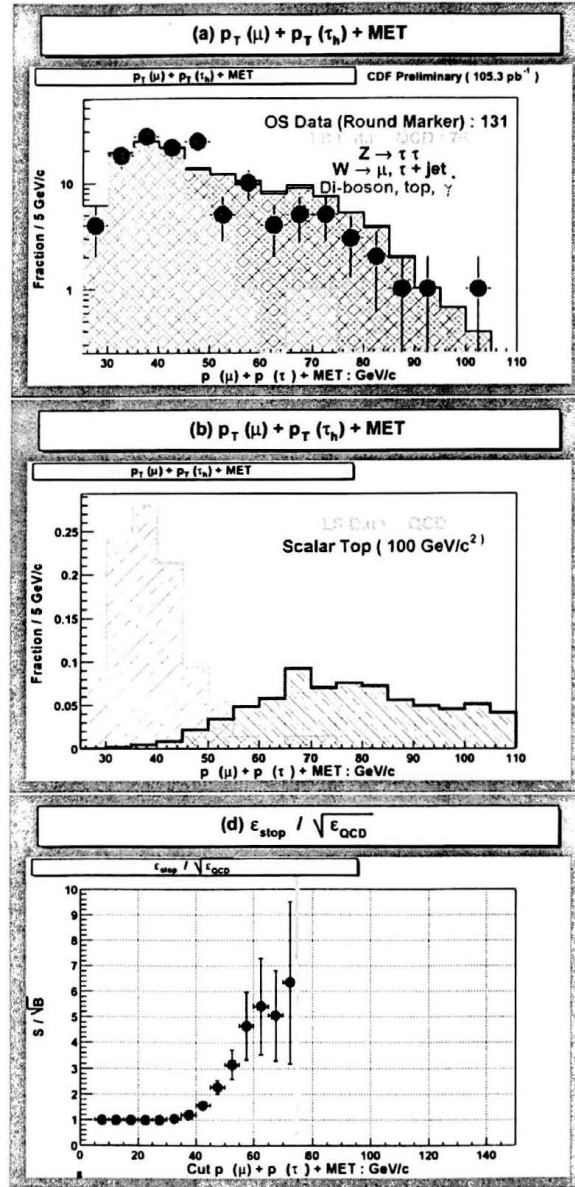


Figure 6.12: Distribution of $H_T(\mu, \tau_h, \cancel{E}_T)$ (top), $H_T(\mu, \tau_h, \cancel{E}_T)$ for $\bar{t}_1 \bar{t}_1$ and QCD events (middle) and $\epsilon_{\bar{t}_1 \bar{t}_1 \rightarrow \tau\tau b\bar{b}} / \sqrt{\epsilon_{\text{QCD}}}$ (bottom)

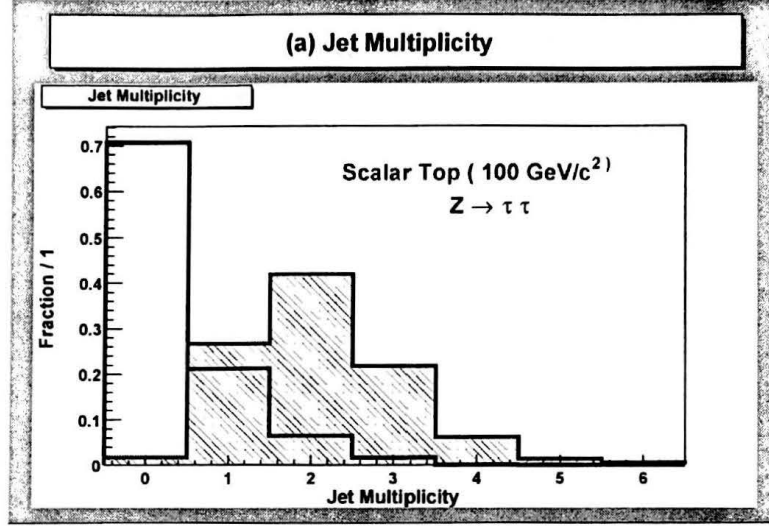


Figure 6.13: Jet multiplicity

quark: 70, 75, 80, 90, 100, 110, 120 and 130 GeV/c². Tables 6.8, 6.9, 6.10 and 6.11 summarize the cut efficiencies with signal acceptances, $A_{\tilde{t}_1\tilde{t}_1}^{MC}$, and trigger efficiencies, $\epsilon_{\tilde{t}_1\tilde{t}_1}^{trg}$ (see Section 3.4). Fig 6.14 shows the cumulative efficiencies of the $\tilde{t}_1\tilde{t}_1$ selection cuts.

6.4.5 Summary of Data Analysis

Table 6.12 shows the event reduction by each selection cut in the data sample. It is compared to the simulated $Z \rightarrow \tau\tau$ and $W + \text{jet}$ samples in Table 6.13.

6.4.6 Background Estimation

Table 6.14 shows the number of events remained after all $\tilde{t}_1\tilde{t}_1$ selection cuts in the data and simulated samples. We observe no candidate events in the data, while the number of background events expected from the Standard Model

$M_{\tilde{t}_1}$ (GeV/ c^2)	70		75	
	Cut efficiency (%)	Cumulative efficiency (%)	Cut efficiency (%)	Cumulative efficiency (%)
Muon selection	13.76	13.76	14.74	14.74
$Z \rightarrow \mu\mu$ veto	99.99	13.76	99.96	14.73
Muon isolation	88.81	12.22	88.63	13.06
Hadronic tau selection	16.35	2.00	17.05	2.23
$M_T(\mu, \cancel{E}_T) \leq 35$ GeV/ c^2	77.84	1.56	76.28	1.70
$p_T(\mu) + p_T(\tau_h) + \cancel{E}_T \geq 75$ GeV	41.01	0.64	44.18	0.75
$N_{jet} \geq 2$	57.51	0.37	59.49	0.45
Signal acceptance (%)	$A_{\tilde{t}_1 \bar{\tilde{t}}_1}^{MC} = 0.37 \pm 0.02(\text{stat})$		$A_{\tilde{t}_1 \bar{\tilde{t}}_1}^{MC} = 0.45 \pm 0.02(\text{stat})$	
Trigger efficiency (%)	$\epsilon_{\tilde{t}_1 \bar{\tilde{t}}_1}^{trg} = 83.6$		$\epsilon_{\tilde{t}_1 \bar{\tilde{t}}_1}^{trg} = 83.6$	

Table 6.8: Cut efficiencies with signal acceptance and trigger efficiency at $M_{\tilde{t}_1} = 70$ and 75 GeV/ c^2

$M_{\tilde{t}_1}$ (GeV/ c^2)	80		90	
	Cut efficiency (%)	Cumulative efficiency (%)	Cut efficiency (%)	Cumulative efficiency (%)
Muon selection	15.45	15.45	16.85	16.85
$Z \rightarrow \mu\mu$ veto	99.96	15.44	99.98	16.85
Muon isolation	89.02	13.75	88.95	14.99
Hadronic tau selection	18.37	2.53	19.72	2.96
$M_T(\mu, \cancel{E}_T) \leq 35$ GeV/ c^2	74.66	1.89	71.67	2.12
$p_T(\mu) + p_T(\tau_h) + \cancel{E}_T \geq 75$ GeV	47.75	0.90	57.38	1.22
$N_{jet} \geq 2$	64.21	0.58	68.52	0.83
Signal acceptance (%)	$A_{\tilde{t}_1\tilde{t}_1}^{MC} = 0.58 \pm 0.03(\text{stat})$		$A_{\tilde{t}_1\tilde{t}_1}^{MC} = 0.83 \pm 0.03(\text{stat})$	
Trigger efficiency (%)	$\epsilon_{\tilde{t}_1\tilde{t}_1}^{trg} = 83.3$		$\epsilon_{\tilde{t}_1\tilde{t}_1}^{trg} = 83.4$	

Table 6.9: Cut efficiencies with signal acceptance and trigger efficiency at $M_{\tilde{t}_1} = 80$ and 90 GeV/ c^2

$M_{\tilde{t}_1}$ (GeV/ c^2)	100		110	
	Cut efficiency (%)	Cumulative efficiency (%)	Cut efficiency (%)	Cumulative efficiency (%)
Muon selection	18.08	18.08	19.03	19.03
$Z \rightarrow \mu\mu$ veto	99.95	18.07	99.92	19.01
Muon isolation	88.91	16.07	89.29	16.98
Hadronic tau selection	21.83	3.51	22.34	3.79
$M_T(\mu, \cancel{E}_T) \leq 35$ GeV/ c^2	70.68	2.48	67.33	2.55
$p_T(\mu) + p_T(\tau_h) + \cancel{E}_T \geq 75$ GeV	66.05	1.64	73.92	1.89
$N_{jet} \geq 2$	71.58	1.17	74.68	1.41
Signal acceptance (%)	$A_{\tilde{t}_1 \bar{\tilde{t}}_1}^{MC} = 1.17 \pm 0.04(\text{stat})$		$A_{\tilde{t}_1 \bar{\tilde{t}}_1}^{MC} = 1.41 \pm 0.04(\text{stat})$	
Trigger efficiency (%)	$\epsilon_{\tilde{t}_1 \bar{\tilde{t}}_1}^{trg} = 83.7$		$\epsilon_{\tilde{t}_1 \bar{\tilde{t}}_1}^{trg} = 83.6$	

Table 6.10: Cut efficiencies with signal acceptance and trigger efficiency at $M_{\tilde{t}_1} = 100$ and 110 GeV/ c^2

$M_{\tilde{t}_1}$ (GeV/ c^2)	120		130	
	Cut efficiency (%)	Cumulative efficiency (%)	Cut efficiency (%)	Cumulative efficiency (%)
Muon selection	20.36	20.36	20.65	20.65
$Z \rightarrow \mu\mu$ veto	99.89	20.34	99.83	20.61
Muon isolation	89.29	18.16	89.68	18.49
Hadronic tau selection	23.33	4.24	24.12	4.46
$M_T(\mu, \cancel{E}_T) \leq 35$ GeV/ c^2	66.30	2.81	64.50	2.88
$p_T(\mu) + p_T(\tau_h) + \cancel{E}_T \geq 75$ GeV	81.46	2.29	86.50	2.49
$N_{jet} \geq 2$	78.29	1.79	80.24	2.00
Signal acceptance (%)	$A_{\tilde{t}_1\tilde{t}_1}^{MC} = 1.79 \pm 0.04(\text{stat})$		$A_{\tilde{t}_1\tilde{t}_1}^{MC} = 2.00 \pm 0.05(\text{stat})$	
Trigger efficiency (%)	$\epsilon_{\tilde{t}_1\tilde{t}_1}^{trg} = 83.7$		$\epsilon_{\tilde{t}_1\tilde{t}_1}^{trg} = 83.8$	

Table 6.11: Cut efficiencies with signal acceptance and trigger efficiency at $M_{\tilde{t}_1} = 120$ and 130 GeV/ c^2

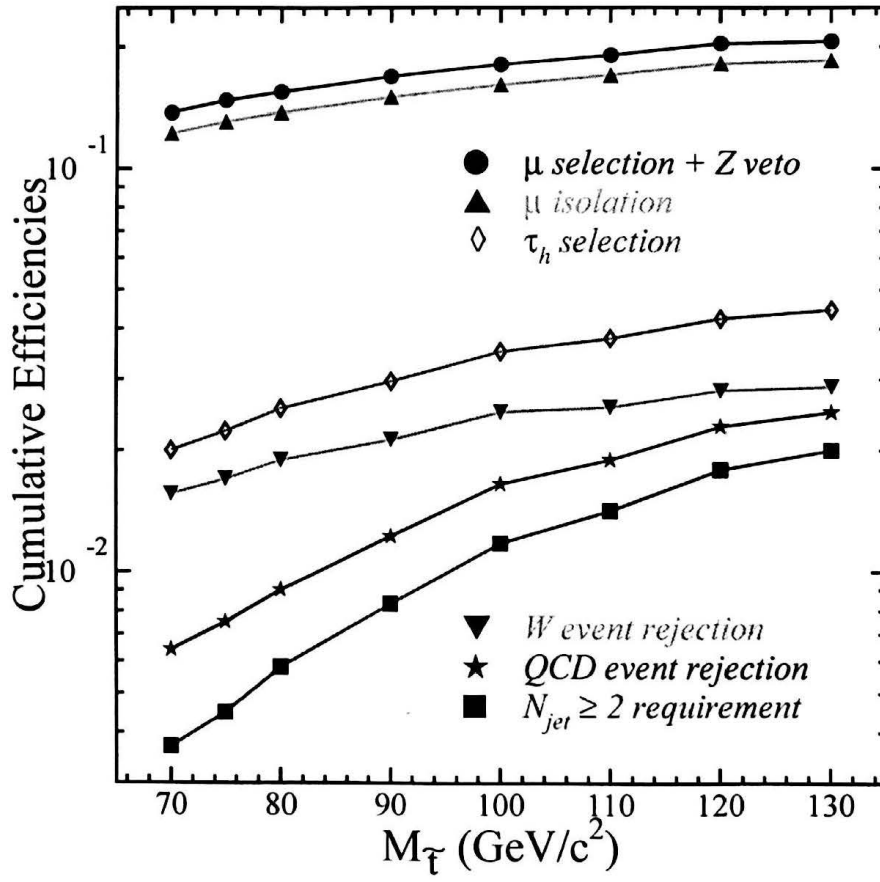


Figure 6.14: Cumulative efficiencies of the $\tilde{t}_1\bar{\tilde{t}}_1$ event selection cuts vs $M_{\tilde{t}_1}$

	OS	LS	OS-LS
Muon selection	511550		
$Z \rightarrow \mu\mu$ veto	510290		
Muon isolation	249050		
Hadronic tau selection	163	82	81
$M_T(\mu, \cancel{E}_T) \leq 35 \text{ GeV}/c^2$	131	75	56
$p_T(\mu) + p_T(\tau_h) + \cancel{E}_T \geq 75 \text{ GeV}$	8	0	8
$N_{jet} \geq 2$	0	0	$N_{\tilde{t}_1\tilde{t}_1}^{obs} = 0$

Table 6.12: $\tilde{t}_1\tilde{t}_1$ events from data sample

processes is $1.13 \pm 0.10(\text{stat}) \pm 0.06(\text{sys})$. The dominant background is $Z \rightarrow \tau\tau$ events. The expected number of $Z \rightarrow \tau\tau$ and $W(\rightarrow \mu\nu \text{ or } \tau\nu) + \text{jet}$ events is estimated by VECBOS+HERPRT. For verification, we also estimate the $Z \rightarrow \tau\tau$ events using ISAJET. The number of OS, LS and OS-LS events in the ISAJET $Z \rightarrow \tau\tau$ samples are $1.10 \pm 0.11(\text{stat})$, $0.04 \pm 0.02(\text{stat})$ and $1.06 \pm 0.12(\text{stat})$, respectively. The estimation of $Z \rightarrow \tau\tau$ using VECBOS+HERPRT is consistent with the estimation by ISAJET.

Cut	$Z(\rightarrow \tau\tau)$		$W(\rightarrow \mu\nu)+\text{jets}$		Data	
	OS	LS	OS	LS	OS	LS
Baseline $\mu + \tau_h$ samples	83.1	0.5	23.2	7.0	163	82
$M_T(\mu, \cancel{E}_T) \leq 35 \text{ GeV}/c^2$	68.0	0.3	2.6	1.4	131	75
$H_T(\mu, \tau_h, \cancel{E}_T) \geq 75 \text{ GeV}/c$	13.5	0.1	0.0	0.3	8	0
$N_{jet} \geq 2$	1.13	0.00	0.00	0.00	0	0

Table 6.13: Number of events in the data and background samples after each cut ($\bar{t}_1 \bar{t}_1$ analysis)

Process	OS	LS	OS-LS
$Z \rightarrow \tau\tau$	1.13	0.00	$1.13 \pm 0.10(\text{stat}) \pm 0.06(\text{sys})$
$W \rightarrow \mu\nu+\text{jets}$			negligible
$W \rightarrow \tau\nu+\text{jets}$			negligible
$\gamma^* \rightarrow \tau\tau$			negligible
$t\bar{t}$	0.05	0.05	$0.00 \pm 0.08 \pm 0.01$
Diboson (WW/WZ/ZZ)	0.02	0.02	$0.00 \pm 0.03 \pm 0.01$
QCD (LS data)	N/A	0	0
Total background	1.20	0.07	$1.13 \pm 0.13 \pm 0.06$
Data (105.3 pb^{-1})	0	0	$N_{\bar{t}_1 \bar{t}_1}^{obs} = 0$

Table 6.14: Summary of estimated backgrounds.

Chapter 7

Systematic Uncertainties

The general concept to estimate the systematic uncertainty from a given source is quite similar for most sources. To estimate the uncertainty from a given source, we change the input parameter for the MC simulation, and evaluate the impact by comparing its event acceptance with that of standard samples. We want to measure the production cross section of $\tilde{t}_1\bar{\tilde{t}}_1$ from experiment using the calibration method introduced in Section 3.4. We calculate the production cross section of $\tilde{t}_1\bar{\tilde{t}}_1$ calibrated by $Z \rightarrow \tau\tau$. Therefore, the systematic uncertainties should be evaluated in both $Z \rightarrow \tau\tau$ and $\tilde{t}_1\bar{\tilde{t}}_1$ events with our strategy. However, the calibration method cancels systematic uncertainties due to the luminosity, z -vertex efficiency and tau branching ratio, and reduces systematic uncertainties due to the unknown effects related with muon and hadronic tau. These advantages are main reason why we use the calibration method. It should be noted that the uncertainty arising from the luminosity measurement is included in the measurement of Z production cross section at CDF.

7.1 Systematic Uncertainties due to Trigger Efficiency

The trigger efficiency of muon depends on its p_T . Therefore, we use trigger efficiency curves to correct the MC simulation. The systematic uncertainty due to the trigger efficiency is estimated with the ratio of trigger efficiencies of $Z \rightarrow \tau\tau$ to $\tilde{t}_1\bar{\tilde{t}}_1$ events. We vary the parameterized curves up and down by one standard deviation for the L1, L2 and L3 triggers. We apply new curves for the acceptance estimation. Then, we evaluate the impact by comparing new acceptances with nominal acceptance. We choose maximum deviation as our systematic uncertainty. They are summarized in Table 7.1.

$M_{\tilde{t}_1}$ (GeV/ c^2)	70	80	90	100	110	120	130
Systematic uncertainties (%)	0.03	0.08	0.07	0.08	0.07	0.08	0.03

Table 7.1: Systematic uncertainties due to trigger efficiency, where $M_{\tilde{t}_1} = 70 \sim 130$ GeV/ c^2 .

7.2 Systematic Uncertainties from $Z \rightarrow \tau\tau$ analysis

Cross Section of $Z(\rightarrow \tau\tau) + \geq n$ -jet Events

We use the production cross section times branching ratio, $\sigma_Z \cdot B(Z \rightarrow ee)$, taken from the CDF measurement [40], as that of $Z \rightarrow \tau\tau$ assuming lepton universality. Therefore, we apply the uncertainties from the $\sigma_Z \cdot Z(\rightarrow ee)$

measurement. However, we use only $Z(\rightarrow \tau\tau) + 0\text{-jet}$ events for calibration, so we also apply the uncertainties caused by the measurement of the ratio of $Z(\rightarrow ee) + \geq n\text{-jet}$ cross section [41]. They are summarized in Table 7.2.

Parton Distribution Function (PDF)

The PDF affects the production cross section, relative contributions of gg fusion and $q\bar{q}$ annihilation and event kinematics. Our nominal choice of PDF is CTEQ4L [53]. For comparison, we choose GRV94LO and MRSG [51]. We generate new simulated samples with two PDFs and evaluate each acceptance deviation by the comparison to nominal samples. We choose the maximum deviation as our systematic uncertainty due to the choice of PDF. It is shown in Table 7.2.

Source of systematic uncertainty	Systematic uncertainties (%)
Data statistics	24.9
PDF	4.7
MC statistics	1.8
$\sigma_Z \cdot B(Z \rightarrow \tau\tau)$	5.2
$R(0\text{-jet})$	3.1
Total	26.1

Table 7.2: Systematic uncertainties from $Z \rightarrow \tau\tau$ analysis.

7.3 Systematic Uncertainties from $\tilde{t}_1\bar{\tilde{t}}_1$ analysis

Gluon Radiation from the Initial or Final State Partons

Gluon radiation, showing up as jet, can originate from the incoming initial state partons, outgoing final state partons or interference between the two. The interference effect is expected to be small, so it is not considered in this analysis. The effect of Initial/Final State Radiation (ISR/FSR) is determined by the following procedure. We prepare another signal sample by linking a routine to turn FSR off in ISAJET. We estimate the size of FSR effect to be the acceptance difference between nominal and new samples. Assuming that the size of ISR effect is similar to that of FSR effect, we take a square-root of quadrature sum of two estimates as our systematic uncertainty due to gluon radiation. They are summarized in Table 7.3.

Q^2 Dependence

The default Q^2 for the two body process in ISAJET is defined as follows:

$$Q^2 = \max\left(\frac{2\hat{s}\hat{t}\hat{u}}{\hat{s}^2 + \hat{t}^2 + \hat{u}^2}, 4M_t^2\right)$$

We examine the acceptance change varying the scale into $0.25Q^2$ and $4Q^2$ using two different routines in ISAJET. We choose the maximum deviation as our systematic uncertainty. They are summarized in Table 7.3.

Parton Distribution Function

We estimate the uncertainty due to the choice of PDF with the same method as that of $Z \rightarrow \tau\tau$ mentioned in Section 7.2. They are summarized in Table 7.3.

Jet Energy Scale

The systematic uncertainty due to the jet energy scale originates from the error in the overall calorimetry calibration. We vary absolute and relative energy scales by $\pm 5\%$. We choose the maximum deviation as our systematic uncertainty. They are summarized in Table 7.3.

$M_{\tilde{t}_1} \text{ (GeV}/c^2\text{)}$	70	80	90	100	110	120	130
Source of systematic uncertainty	Systematic uncertainties (%)						
Gluon radiation	2.4	2.4	2.3	2.3	2.2	2.2	2.1
Q^2 dependence	6.8	6.8	6.8	6.7	6.6	6.6	6.6
PDF	4.8	4.8	4.7	4.7	4.6	4.6	4.5
Jet energy scale	3.0	2.1	2.8	2.2	1.4	1.6	1.0
MC statistics	5.5	3.7	3.6	3.0	2.8	2.4	2.3
Total	10.7	9.7	9.7	9.3	8.9	8.8	8.6

Table 7.3: Systematic uncertainties from $\tilde{t}_1 \bar{\tilde{t}}_1 \rightarrow (\tau^+ b)(\tau^- \bar{b}) \rightarrow \mu \tau_h b \bar{b} + X$ analysis, where $M_{\tilde{t}_1} = 70 \sim 130 \text{ GeV}/c^2$

Chapter 8

Results & Discussion

We have searched for the pair-production of the scalar top quarks which are predicted by supersymmetric theory. We consider the R_p violating decay of the scalar top quark via non-negligible λ'_{333} and ϵ_3 couplings, $\tilde{t}_1 \rightarrow \tau b$, which also violates tau lepton number, using the 105.3 pb^{-1} data collected by the CDF detector in $p\bar{p}$ collisions at $\sqrt{s} = 1.8 \text{ TeV}$. The experimental signature of $\tilde{t}_1 \bar{\tilde{t}}_1 + X \rightarrow (\tau^+ b)(\tau^- \bar{b}) + X \rightarrow \mu \tau_h b\bar{b} + X$ is considered, where τ_h is a hadronically decaying tau lepton. The data was inclusively triggered by a muon. We use a sample of $Z(\rightarrow \tau\tau) + 0$ -jet events to calibrate the analysis. We obtain a null result and set a 95% C.L. lower limit on $M_{\tilde{t}_1}$. An analysis has been performed concurrently with this one based on the signature $\tilde{t}_1 \bar{\tilde{t}}_1 + X \rightarrow (\tau^+ b)(\tau^- \bar{b}) + X \rightarrow e \tau_h b\bar{b} + X$ with the 106 pb^{-1} data inclusively triggered by an electron. In Section 8.2, the individual limits from both analyses are combined to set a complete limit. Similar analyses have been carried out by the OPAL and ALEPH Collaborations at LEP considering λ'_{33k} ($k = 1, 2, 3$) couplings and the process $e^+ e^- \rightarrow \tilde{t}_1 \bar{\tilde{t}}_1 \rightarrow (\tau^+ q)(\tau^- \bar{q})$ (see Section 3.3), and a null result was also obtained. We compare our limit to theirs.

8.1 Results

The statistical method setting a limit in new particle searches in the CDF experiment is briefly presented in this section. Next, we describe our results with the limit on $M_{\tilde{t}_1}$.

In new particle searches, one selects from a large number of events those which bear characteristics of the new process, while minimizing the events from well-known processes. This results in a small number of events passing the selection criteria. In our case, the result is consistent with the background expectation. At first, we set an upper limit on the number of signal events presenting in the sample at a Confidence Level (C.L.) of 95%, employing a statistical method which allows us to take into account the systematic uncertainties in the signal acceptance and expected background. For single-channel counting experiments like this analysis, the classical Helene formula [67], with Bayesian integration over systematic uncertainties in the signal acceptance and background, is employed to determine upper limits on Poisson processes in the presence of both statistical and systematic uncertainties, simultaneously in the signal acceptance and background. This is the standard method adopted by the CDF Collaboration [68, 69].

We observe no candidate events passing our selection criteria in the data, while we expect 1.13 ± 0.04 events from the Standard Model processes, $\gamma^*/Z(\rightarrow \tau\tau)+\text{jets}$, $W(\rightarrow \mu\nu \text{ or } \tau\nu)+\text{jets}$, $t\bar{t}$ and $WW/WZ/ZZ$. Therefore, we calculate the 95% C.L. upper limits on the pair-production cross section of the scalar top quark, when $M_{\tilde{t}_1}$ is 70, 80, 90, 100, 110, 120 and 130 GeV/ c^2 . We first calculate $N_{\tilde{t}_1\bar{\tilde{t}}_1}^{95\%CL}$ used to calculate $\sigma_{\tilde{t}_1\bar{\tilde{t}}_1}^{95\%CL}$ by the formula introduced in Section 3.4, Equation (3.9), which calibrates the $\tilde{t}_1\bar{\tilde{t}}_1$ analysis with $Z \rightarrow \tau\tau$

analysis. In the Equation (3.9), $N_{\tilde{t}_1\tilde{t}_1}^{obs} - N_{\tilde{t}_1\tilde{t}_1}^{BG}$ is modified to $N_{\tilde{t}_1\tilde{t}_1}^{95\%CL}$ for the calculation of $\sigma_{\tilde{t}_1\tilde{t}_1}^{95\%CL}$ and we assume $\beta \equiv B(\tilde{t}_1 \rightarrow \tau^+ b) = 1$ (100%). A_Z^{MC} , ε_Z^{trg} and $N_Z^{obs} - N_Z^{BG}$ are obtained from the $Z \rightarrow \tau\tau$ analysis and summarized in Table 8.4 (see Section 8.2). The results are shown in Table 8.1. We combine all uncertainties in quadrature to obtain total systematic uncertainty shown in the table (see Tables 7.1, 7.2 and 7.3). We also calculate the 95% C.L. expected upper limits assuming that we observe one event in the data as expected from our background estimations and assuming exact consistency between the data and MC simulation in the $Z \rightarrow \tau\tau$ analysis. For the calculation, we modify the number 23 for OS data to 33 ($\sim 23/0.7$) and 2 for LS data to 3 ($\sim 2/0.7$) using simple proportionality, since 30 ($\sim (23-2)/0.7$) $Z(\rightarrow \tau\tau) + 0$ -jet events are expected from MC simulation after OS–LS subtraction. These new numbers give $N_Z^{obs} - N_Z^{BG} = 29.1 \pm 6.0(\text{stat}) \pm 0.2(\text{sys})$ and change systematic uncertainty due to data statistics in $Z \rightarrow \tau\tau$ analysis from 24.9% to 20.6%. Thus, the total systematic uncertainty in $Z \rightarrow \tau\tau$ analysis decreases from 26.1% into 22.1% and as a consequence the total uncertainty changes. The results are shown in Table 8.2. Both limits are calculated using the Poisson statistics. Figure 8.1 shows both calculations at the same time with NLO QCD calculation. We set a 95% C.L. lower limit on $M_{\tilde{t}_1}$ at 75 GeV/ c^2 by taking the cross point between the limit derived by this analysis and NLO calculation. The expected limit is 80 GeV/ c^2 .

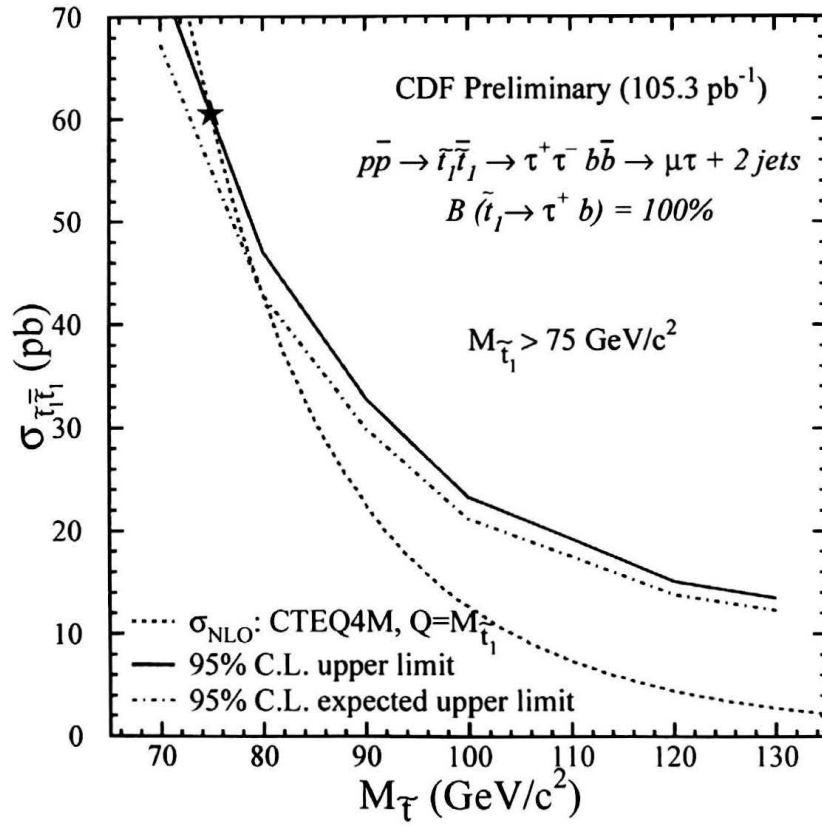


Figure 8.1: 95% C.L. limits for $\tilde{t}_1 \tilde{t}_1^* + X \rightarrow (\tau^+ b)(\tau^- \bar{b}) + X \rightarrow \mu \tau_h b \bar{b} + X$ along with the NLO QCD calculation

$M_{\tilde{t}_1}$ (GeV/ c^2)	Acceptance (%)	$\varepsilon_{\tilde{t}_1\tilde{t}_1}^{trg}$ (%)	Total uncertainty (%)	$N_{\tilde{t}_1\tilde{t}_1}^{95\%CL}$	$\sigma_{\tilde{t}_1\tilde{t}_1}^{95\%CL}$ (pb)
70	0.37	83.6	28.2	3.46	73.8
80	0.58	83.3	27.8	3.44	47.0
90	0.83	83.4	27.8	3.44	32.8
100	1.17	83.7	27.7	3.44	23.2
110	1.41	83.6	27.6	3.44	19.2
120	1.79	83.7	27.5	3.44	15.1
130	2.00	83.8	27.5	3.44	13.5

Table 8.1: 95% C.L. limits on the production cross section of $\tilde{t}_1\tilde{t}_1 + X \rightarrow (\tau^+b)(\tau^-\bar{b}) + X \rightarrow \mu\tau_h b\bar{b} + X$, where $M_{\tilde{t}_1} = 70 \sim 130$ GeV/ c^2 .

8.2 Limits

We set a 95% C.L. lower limit on $M_{\tilde{t}_1}$ at 75 GeV/ c^2 . The analysis considering the “electron” signature, $\tilde{t}_1\tilde{t}_1 + X \rightarrow (\tau^+b)(\tau^-\bar{b}) + X \rightarrow e\tau_h b\bar{b} + X$, sets a 95% C.L. lower limit on $M_{\tilde{t}_1}$ at 111 GeV/ c^2 . Here, we combine two individual limits to set a complete limit for $\tilde{t}_1\tilde{t}_1 + X \rightarrow (\tau^+b)(\tau^-\bar{b}) + X \rightarrow \ell\tau_h b\bar{b} + X$.

We use a Bayesian statistical method which calculates the upper limits on Poisson processes at 95% C.L. given a certain number of observed events, an expected number of background events from known processes, and uncertainty on both the overall acceptance and the expected backgrounds.

The combination has been done by multiplying the likelihood results from the electron and muon analyses. Both are Poisson probabilities for the observed number of events and are smeared with two Gaussian likelihoods

$M_{\tilde{t}_1}$ (GeV/ c^2)	Acceptance (%)	$\varepsilon_{\tilde{t}_1\tilde{t}_1}^{trg}$ (%)	Total uncertainty (%)	$N_{\tilde{t}_1\tilde{t}_1}^{95\%CL}$	$\sigma_{\tilde{t}_1\tilde{t}_1}^{95\%CL}$ (pb)
70	0.37	83.6	24.6	4.57	67.3
80	0.58	83.3	24.1	4.54	42.8
90	0.83	83.4	24.1	4.54	29.9
100	1.17	83.7	24.0	4.54	21.1
110	1.41	83.6	23.8	4.53	17.5
120	1.79	83.7	23.8	4.53	13.8
130	2.00	83.8	23.7	4.53	12.3

Table 8.2: 95% C.L. expected limits on the production cross section of $\tilde{t}_1\tilde{t}_1 + X \rightarrow (\tau^+b)(\tau^-\bar{b}) + X \rightarrow \mu\tau_h b\bar{b} + X$, where $M_{\tilde{t}_1} = 70 \sim 130$ GeV/ c^2 .

which incorporate the errors in the acceptance and the backgrounds. We normalize the channels according to the relative luminosities. The smearing is done using a Monte Carlo method which averages over 100,000 pseudo-experiments. This method effectively puts all the uncertainty into an effective $N_{\tilde{t}_1\tilde{t}_1}^{95\%CL}$ which can be put into Equation (3.9). Because the both analyses use the $Z \rightarrow \tau\tau$ analysis for calibration, the same formula is adopted for the calculation. See Tables 8.1 and 8.3 for the acceptance and efficiency estimations for the signal events, and Table 8.4 for the summary of the $Z \rightarrow \tau\tau$ analysis. The final results are summarized in Table 8.5 and Figure 8.2. We set a 95% C.L. upper limit on $\sigma_{\tilde{t}_1\tilde{t}_1}$ at 4.69 pb and lower limit on $M_{\tilde{t}_1}$ at 119 GeV/ c^2 for $\beta = 1$.

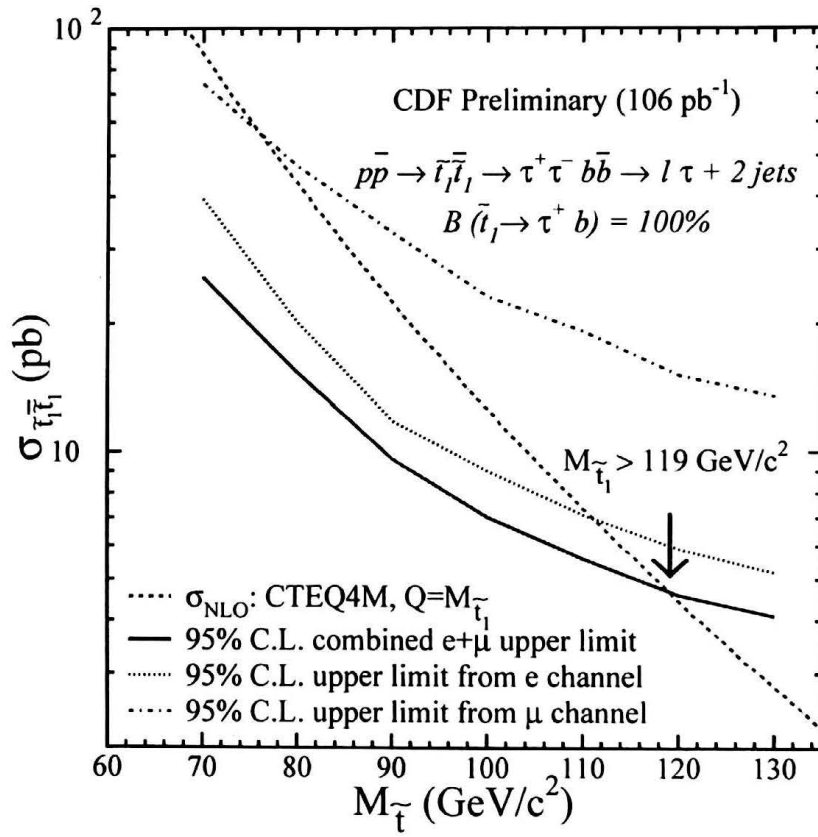


Figure 8.2: 95% C.L. limits for $\bar{t}_1 \bar{t}_1 + X \rightarrow (\tau^+ b)(\tau^- \bar{b}) + X \rightarrow \ell \tau_h b\bar{b} + X$ along with the NLO QCD calculation

$M_{\tilde{t}_1}$ (GeV)	$A_{\tilde{t}_1\tilde{t}_1}^{MC}$ (%)	$\varepsilon_{\tilde{t}_1\tilde{t}_1}^{trg}$ (%)	Total uncertainty (%)	$N_{\tilde{t}_1\tilde{t}_1}^{95\%CL}$	$\sigma_{\tilde{t}_1\tilde{t}_1}^{95\%CL}$ (pb)	$\sigma_{\text{theory}}^{NLO}$ (pb)
70	0.55	77.1	22.3	3.26	39.4	86.5
80	0.93	77.5	21.2	3.23	20.1	42.8
90	1.57	77.6	20.8	3.22	11.8	22.5
100	2.06	78.1	20.2	3.21	9.0	12.6
110	2.58	78.1	19.6	3.19	7.1	7.3
120	3.08	78.5	19.5	3.19	5.9	4.4
130	3.49	78.5	19.4	3.19	5.2	2.8

Table 8.3: 95% C.L. limits on the production cross section of $\tilde{t}_1\tilde{t}_1 + X \rightarrow (\tau^+b)(\tau^-\bar{b}) + X \rightarrow e\tau_h b\bar{b} + X$, where $M_{\tilde{t}_1} = 70 \sim 130 \text{ GeV}/c^2$ [27].

	electron channel	muon channel
$N_Z^{obs} - N_Z^{BG}$	45.6 ± 7.8	20.1 ± 5.0
$A_Z^{MC} \text{ (%)}$	1.48	0.86
$\varepsilon_Z^{trg} \text{ (%)}$	74.5	83.0

Table 8.4: Results of the $Z \rightarrow \tau\tau$ analysis [27, 28]

$M_{\tilde{t}_1}$ (GeV)	$N_{\tilde{t}_1\bar{\tilde{t}_1}}^{95\%CL}$	$\sigma_{\tilde{t}_1\bar{\tilde{t}_1}}^{95\%CL}$ (pb)	$\sigma_{\text{theory}}^{NLO}$ (pb)
70	3.67	25.7	86.5
80	3.60	15.3	42.8
90	3.56	9.6	22.5
100	3.54	7.0	12.6
110	3.51	5.6	7.3
120	3.51	4.6	4.4
130	3.51	4.1	2.8

Table 8.5: 95% C.L. Combined limits on the production cross section of $\tilde{t}_1\bar{\tilde{t}_1} + X \rightarrow (\tau^+b)(\tau^-\bar{b}) + X \rightarrow \ell\tau_h b\bar{b} + X$, where $M_{\tilde{t}_1} = 70 \sim 130 \text{ GeV}/c^2$.

Chapter 9

Conclusion & Summary

A search for the lightest scalar top quark, a superpartner of the top quark, has been performed with the signature, $\tilde{t}_1 \bar{\tilde{t}}_1 + X \rightarrow (\tau^+ b)(\tau^- \bar{b}) + X \rightarrow \ell \tau_h b \bar{b} + X$, where ℓ is an electron or a muon, and τ_h is a hadronically decaying tau lepton. Both electron and muon analyses obtain null results and set 95% C.L. lower limits on $M_{\tilde{t}_1}$ at 111 and 75 GeV/ c^2 , respectively. We combine the two limits and set a 95% C.L. lower limit at 119 GeV/ c^2 . This limit is stronger than the current limit set by the ALEPH Collaboration at LEP.

Appendix A

The Main Injector (MI) and the Antiproton Recycler Ring

The construction of the MI results in significant enhancements to both the collider and fixed target experiments in Fermilab.

A.1 Brief History

The MI has been a decade in the construction. In 1987, a study of how Fermilab could enhance the performance of the Tevatron beyond its original performance goals, by integrating a new accelerator or accelerators within the existing complex was undertaken and a report identifying several possibilities, all with a common strategy – produce more antiprotons for the collider – was written. The report contained several designs including the construction of two new accelerators operating at 20 GeV and the construction of the second Tevatron for proton-proton collisions, supported by a new Main Ring. Finally, a Main Ring replacement supporting continued proton-antiproton collisions

in the existing Tevatron was chosen. Fermilab proposed this project to the Department Of Energy (DOE) in 1989, and funding for the MI project was approved in 1991. After extended design and R&D period, the construction was started in the spring of 1993. The project was completed in 1999.

The completion of the MI represents not an end but a beginning. It will take great effort to realize its full potential for the improvement of the research program at Fermilab. At last, we have reached a point where we can see clearly that Fermilab will reap the benefits of the MI for decades to come.

A.2 Particle Acceleration in Run II

A.2.1 The Main Injector

The MI is located south of the Antiproton Storage Ring and tangent to the Tevatron Ring at the FØ straight section. It will perform all duties currently required of the existing Main Ring with concurrent reduction in the background rates seen in the colliding beam detectors. The MI will supply high intensity proton beams for antiproton production, combine proton bunches from the Booster into a single high intensity bunch to use in the collider, and effectively accelerate antiprotons to inject into the Tevatron. The MI accelerates protons from 8 GeV to 120 GeV for antiproton production, and provides high duty factor 150 GeV beam to the Tevatron during collider operation, a capability which does not presently exist in the Main Ring. Particles circle the MI's 3.2186 km circumference nearly 100,000 times per second. The MI decelerates antiprotons from the Tevatron, sending them to the Recycler Ring and sends protons to the NuMI experiment for neutrino production.

A.2.2 The Antiproton Recycler Ring

The Recycler Ring shares the tunnel with the MI, recovering and recycling antiprotons from the Tevatron. It uses permanent magnets which operate without the need for power and water.

The role of the Recycler Ring is to provide more antiprotons for the Tevatron (for a tenfold increase in collisions), which proportionally increases the luminosity (more possibility for discovery). This is accomplished by acting as a high reliability post-Accumulator and receptacle for recycled antiprotons from previous collider stores. The Recycler Ring recovers and stores antiprotons that would have been discarded. The recycled antiprotons are transferred to the MI, and accelerated to use in future Tevatron collider experiments. Prior to the development of the Recycler Ring, the peak luminosity goal of the upgrade was $8 \times 10^{31} \text{ cm}^{-2}\text{s}^{-1}$. With the construction of the Recycler Ring, a typical peak luminosity of $2 \times 10^{32} \text{ cm}^{-2}\text{s}^{-1}$ is expected.

Appendix B

The CDF Upgrades

The goal of Tevatron Run II is to accumulate more than 35 fb^{-1} at $\sqrt{s} = 2.0 \text{ TeV}$, using luminosities up to $2 \times 10^{32} \text{ cm}^{-2}\text{s}^{-1}$. The modest increase in the energy has a major impact on physics, but little impact on the detector performance. The high luminosities, the number of bunches and the time between crossings require extensive changes to the experimental apparatus. Ten years of experience with CDF and Tevatron physics has been applied in the design of an upgraded CDF detector called “CDF II.” It is described in [45]. The crossing time defines an overall time constant for signal integration, data acquisition and triggering. Two sets of Tevatron operating conditions for Run II are:

- $\mathcal{L} = 1 \times 10^{32} \text{ cm}^{-2}\text{s}^{-1}$, 396 ns crossing time (36 bunches)
- $\mathcal{L} = 2 \times 10^{32} \text{ cm}^{-2}\text{s}^{-1}$, 132 ns crossing time (108 bunches)

Appendix C

Perspectives on Scalar Top Search in Run II

In Run II, the luminosity enhancement provided by the MI in conjunction with the good quality detector, the CDF II, will dramatically increase the discovery reach. The CDF II will collect data at $\sqrt{s} = 2.0$ TeV. The integrated luminosity will be greater than 35 fb^{-1} . The production cross section for heavy superpartners will increase significantly with the higher energy. SUSY searches will cover a wide range of parameter space. Figure C.1 shows the pair-production cross section of the lightest scalar top quark at the Tevatron in Run II.

For Run II, the CDF experiment is implementing a new tau trigger which combines the information of specific physics signatures with tracking requirements for the tau. The experience gained during Run I and Monte Carlo simulations have taught that tracking information is more efficient than calorimeter information, especially for low- p_T taus. Track isolation can be used to further reduce the acquisition rate.

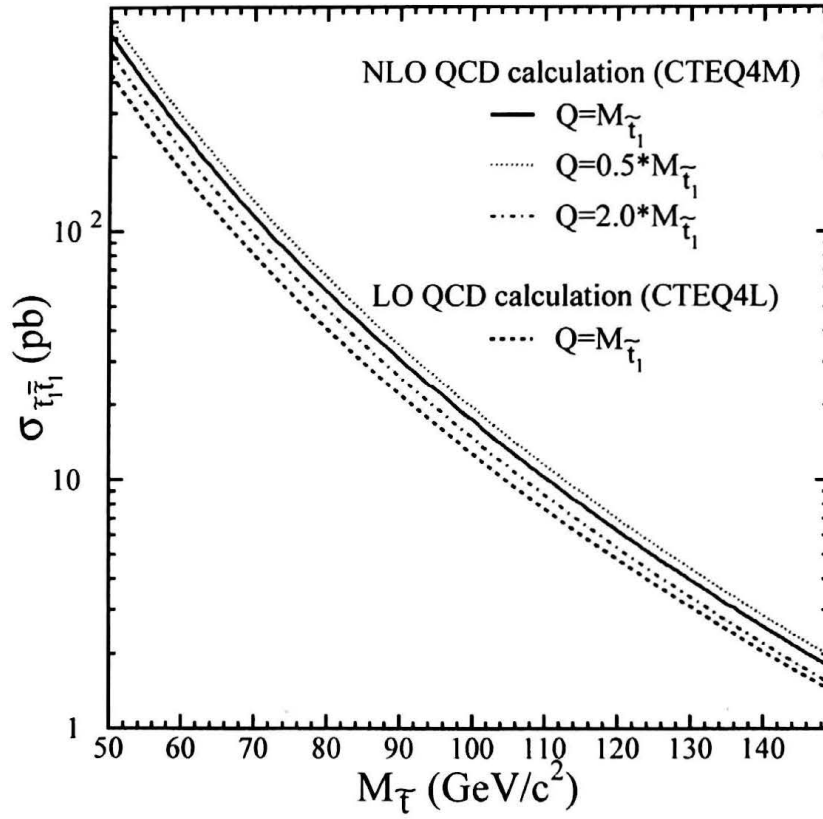


Figure C.1: The pair-production cross section of the lightest scalar top quark at the Tevatron in Run II

Bibliography

- [1] National Research Council, *Elementary-Particle Physics: Revealing the Secrets of Energy and Matter* (1998).
- [2] S. L. Glashow, *Partial-symmetries of weak interactions*, Nucl. Phys. **22**, 579 (1961).
- [3] S. Weinberg, *A model of leptons*, Phys. Rev. Lett. **19**, 1264 (1967).
- [4] A. Salam, in *Elementary Particle Theory*, edited by N. Svartholm, 367, Almquist and Wiksells, Stockholm (1969).
- [5] S. L. Glashow, J. Iliopoulos and L. Maiani, *Weak Interactions with Lepton-Hadron Symmetry*, Phys. Rev. **D2**, 1285 (1970).
- [6] Particle Data Group, *Review of Particle Physics*, Eur. Phys. J. **C15**, 1-878 (2000).
- [7] F. Caravaglios, F. Parodi, P. Roudeau and A. Stocchi, *Determination of the CKM unitarity triangle parameters by end 1999*, hep-ph/0002171 (2000).
- [8] http://delphiwww.cern.ch/~offline/physics_links/lepc.html

- [9] K. Huang, *Quarks, Leptons, & Gauge Fields*, World Scientific Publishing (1982).
- [10] Edited by G. L. Kane, *Perspectives on supersymmetry*, Advanced Series on Directions in High Energy Physics, Vol. 18 (1998).
- [11] M. Drees, *An Introduction to Supersymmetry*, hep-ph/9611409 (1996).
- [12] S. Dawson, *The MSSM and why it works*, hep-ph/9712464 (1997).
- [13] H. E. Haber, *Recent Directions in Particle Theory*, Proceedings of the 1992 Theoretical Advanced Study Institute in Particle Physics, edited by J. Harvey and J. Polchinski, World Scientific, 589-686 (1993).
- [14] S. Dimopoulos and D. Sutter, *The supersymmetric flavor problem*, Nucl. Phys. **B452**, 496 (1995); D. Sutter, *The Supersymmetric Flavor Problem and Mu to E Plus Gamma*, hep-ph/9704390 (1997).
- [15] H. E. Haber, *The status of the minimal supersymmetric standard model and beyond*, Nucl. Phys. B (Proceedings Supplements) **62A-C**, 469 (1998).
- [16] M. A. Díaz, J. Ferrandis, J. C. Romão and J. W. Valle, *Gauge and Yukawa Unification with Broken R-parity*, hep-ph/9801391 (1998).
- [17] Edited by H. Dreiner, *Searching for R-parity Violation at Run-II of the Tevatron*, hep-ph/9906224 (1999).
- [18] H. Dreiner, *Introduction to Explicit R-parity Violation*, hep-ph/9707435 (1997).

- [19] M. A. Díaz, *The Minimal Supersymmetric Standard Model with a Bilinear R-parity Violating Term*, hep-ph/9711435 (1997).
- [20] W. Beenakker, M. Krämer, T. Plehn and M. Spira, *SUSY Particle Production at the Tevatron*, hep-ph/9810290 (1998).
- [21] W. Beenakker, M. Krämer, T. Plehn, M. Spira and P. M. Zerwas, *Stop production at hadron colliders*, Nucl. Phys. **B515**, 3-14 (1998).
- [22] W. Beenakker, R. Höpker and M. Spira, *PROSPINO: A Program for the Production of Supersymmetric Particles In Next-to-leading Order QCD*, hep-ph/9611232 (1996).
- [23] W. Porod, D. Restrepo and J. W. F. Valle, *Light Stop: MSSM versus R-parity Violation*, hep-ph/0001033 (2000).
- [24] F. de Campos, M. A. Díaz, O. J. P. Eboli, M. B. Magro, L. Navarro, W. Porod, D. A. Restrepo and J. W. F. Valle, *R-parity violating decays of the Top-Quark and the Top-Squark at the Tevatron*, hep-ph/9903245 (1999).
- [25] A. Bartl, W. Porod, M. A. García-Jareño, M. B. Magro, J. W. F. Valle and W. Majerotto, *New signatures for a light stop at LEP2 in SUSY models with spontaneously broken R-parity*, hep-ph/9606256 (1996).
- [26] CDF Collaboration, *Search for Third-Generation Leptoquarks from Technicolor Models in $p\bar{p}$ Collisions at $\sqrt{s} = 1.8\text{TeV}$* , Phys. Rev. Lett. **82**, 3206 (1999).
- [27] Y. Miyazaki, M. J. Kim, M. Tanaka, T. Kamon, M. Chertok, J. P. Done, Y. Kato, D. H. Kim, T. Okusawa, Y. Seiya and K. Yamamoto, *Search for*

- R-Parity Violating Decays of Scalar Top Quarks in Two Taus and Two Jets Events – Electron Channel* –, CDF Note 5570 (2001).
- [28] M. J. Kim, Y. Miyazaki, M. Tanaka, T. Kamon, M. Chertok, J. P. Done, Y. Kato, D. H. Kim, T. Okusawa, Y. Seiya and K. Yamamoto, *A Search for R-parity Violating Scalar Top Quark Decays in Two Tau and Two Jet Events – Muon Channel* –, CDF Note 5584 (2001).
- [29] M. J. Kim, Y. Miyazaki, S. W. Lee, T. Kamon and D. Toback, *Combined Limits from Searches for Pair-production and R-parity Violating Decays of Scalar Top Quarks*, CDF Note 5601 (2001).
- [30] OPAL Collaboration, *Search for R-parity violating decays of scalar fermions at LEP*, Eur. Phys. J. **C12**, 1 (2000).
- [31] ALEPH Collaboration, *Search for R-parity Violating Decays of Supersymmetric Particles in e^+e^- Collisions at Centre-of-Mass Energies from 189 GeV to 202 GeV*, Eur. Phys. J. **C19**, 415-428 (2001).
- [32] T. J. LeCompte and W. Sakumoto, *Measurement of the Level 1 CMU High p_T Trigger Efficiency*, CDF Note 3028 (1995).
- [33] J. D. Lewis and T. J. LeCompte, *Measurement of Run IA Level 2 CMUP Trigger Efficiencies*, CDF Note 3130 (1995).
- [34] J. P. Done, M. Chertok, T. Kamon, S. Lammel and J. D. Lewis, *Study of Level 2 Inclusive Muon Trigger Efficiency in Run IB*, CDF Note 4017 (1999).
- [35] T. J. LeCompte and D. A. Glenzinski, *A Period of High p_T Muon Level 2 Trigger Failures in Run IB*, CDF Note 2985 (1995).

- [36] T. Kamon, Y. Kato and J. Wolinski, *Study of the Inclusive Lepton Trigger Efficiency for the Run IA SUSY Trilepton Analysis*, CDF Note 2596 (1995).
- [37] N. L. Bruner, *Level 3 Trigger Efficiencies for the Low p_T Inclusive Lepton Data Sets MULB and ECLB*, CDF Note 4700 (1998).
- [38] J. P. Done, M. Chertok and T. Kamon, *Study of Run IB Lepton Identification Efficiencies for SUSY Searches*, CDF Note 4218 (1997).
- [39] J. P. Done, M. Chertok and T. Kamon, *Study of Run IB Lepton Isolation Efficiencies for SUSY Searches*, CDF Note 4291 (1998).
- [40] CDF Collaboration, *Measurement of $\sigma B(W \rightarrow e\nu)$ and $\sigma B(Z^0 \rightarrow e^+e^-)$ in $p\bar{p}$ Collisions at $\sqrt{s} = 1.8$ TeV*, Phys. Rev. Lett. **76**, 3070 (1996).
- [41] D. Cronin-Hennessy, J. R. Dittmann, A. T. Goshaw, S. A. Hauger, W. Kowald, T. J. Phillips and W. J. Robertson, *Measurement $Z \rightarrow e^+e^- + N$ Jet Cross Sections in 1.8 TeV $p\bar{p}$ Collisions*, CDF Note 3360 (1996).
- [42] http://www.fnal.gov/pub/accel_tour.html
- [43] CDF Collaboration, *A Two Level Fastbus Based Trigger System for CDF*, Nucl. Instrum. Meth. **A269**, 51 (1988).
- [44] CDF Collaboration, *The CDF Detector: An Overview*, Nucl. Instrum. Meth. **A271**, 387 (1988).
- [45] CDF II Collaboration, *The CDF II Detector Technical Design Report*, FERMILAB-Pub-96/390-E (1996).
- [46] H. Baer, F. E. Paige, S. D. Protopopescu and X. Tata, hep-ph/0001086.

- [47] F. A. Berends, W. T. Giele, H. Kuijf and B. Tausk, Nucl. Phys. **B357**, 32 (1991).
- [48] P. Avery, K. Read and G. Trahern, Cornell Internal Note CSN-212 (unpublished) (1985).
- [49] G. Marchesini and B. R. Webber, Nucl. Phys. **B310**, 461 (1988); G. Marchesini *et al.*, Comput. Phys. Commun. **67**, 465 (1992).
- [50] J. P. Done, M. Chertok and T. Kamon, *ISAJET Monte Carlo Validation*, CDF Note 4903 (1999).
- [51] <http://wwwinfo.cern.ch/asdoc/pdflib.ps.gz> (2000).
- [52] H. L. Lai, J. Huston, S. Kuhlmann, J. Morfin, F. Olness, J. F. Owens, J. Pumplin and W. K. Tung, *Global QCD Analysis of Parton Structure of the Nucleon: CTEQ5 Parton Distributions*, hep-ph/9903282 (1998).
- [53] H. L. Lai, J. Huston, S. Kuhlmann, F. Olness, J. Owens, D. Soper, W. K. Tung and H. Weerts, *Improved parton distributions from global analysis of recent deep inelastic scattering and inclusive jet data*, Phys. Rev. **D55**, 1280 (1997).
- [54] S. D. Drell and T-M Yan, *Massive lepton-pair production in hadron-hadron collisions at high energies*, Phys. Rev. Lett. **25**, 316 (1970).
- [55] CDF Collaboration, *Measurement of Drell-Yan electron and muon pair differential cross sections in $p\bar{p}$ collisions at $\sqrt{s} = 1.8$ TeV*, Phys. Rev. **D49**, 1 (1994).
- [56] The Top Group, *The New Combined CDF $t\bar{t}$ Production Cross Section for Run I*, CDF Note 5043 (1999).

- [57] CDF Collaboration, *Evidence for W^+W^- Production in $p\bar{p}$ Collisions at $\sqrt{s} = 1.8$ TeV*, Phys. Rev. Lett. **78**, 4536 (1997).
- [58] J. Ohnemus, Phys. Rev. **D44**, 3477 (1991).
- [59] J. Ohnemus and J.F. Owens, Phys. Rev. **D43**, 3626 (1991).
- [60] S. Jadach, J. H. Kühn and Z. Was, *TAUOLA-a library of Monte Carlo programs to simulate decays of polarized τ leptons*, Comput. Phys. Commun. **64**, 275 (1991).
- [61] M. Jezabek, Z. Was, S. Jadach and J. H. Kühn, *The τ decay library TAUOLA, update with exact $\mathcal{O}(\alpha)$ QED corrections in $\tau \rightarrow \mu(e)\nu\bar{\nu}$ decay modes*, Comput. Phys. Commun. **70**, 69 (1992).
- [62] Z. Was and S. Jadach, *TAUOLA Monte Carlo for τ Decays. A Question of Systematic Errors*, CERN-TH 6727/92 (1992).
- [63] S. Jadach, Z. Was, R. Decker and J. H. Kühn, *The τ decay library TAUOLA, version 2.4*, Comput. Phys. Commun. **76**, 361 (1993).
- [64] CDF Collaboration, *The $\mu\tau$ and $e\tau$ Decays of Top Quark Pairs Produced in $p\bar{p}$ Collisions at $\sqrt{s} = 1.8$ TeV*, Phys. Rev. Lett. **79**, 3585 (1997).
- [65] CDF Collaboration, *Search for the Charged Higgs Boson in the Decays of Top Quark Pairs in the $e\tau$ and $\mu\tau$ Channels at $\sqrt{s} = 1.8$ TeV*, Phys. Rev. **D62**, 012004 (2000).
- [66] CDF Collaboration, *Search for Third-Generation Leptoquarks from Technicolor Models in $p\bar{p}$ Collisions at $\sqrt{s} = 1.8$ TeV*, Phys. Rev. Lett. **82**, 3206 (1999).

- [67] O. Helene, Nucl. Instrum. Meth. Phys. Res. **A212**, 319 (1983)
- [68] G. J. Feldman and R. D. Cousins, *Unified approach to the classical statistical analysis of small signals*, Phys. Rev. **D57**, 3873 (1998).
- [69] J. Conway, *Setting Limits and Making Discoveries in CDF*, CDF Note 5236 (2000).

질량중심에너지 1.8 TeV 양성자-반양성자 충돌실험에서
R-패러티가 깨어지는 붕괴 채널을 통한 스칼라 톱 쿼크의 탐색

김 민 정

경북대학교 대학원 물리학과 입자물리학 전공
(지도교수 김 동 희)

(초 록)

CDF 검출기를 통하여 질량중심에너지 1.8 TeV의 양성자-반양성자 충돌 하에서 획득한 106 pb^{-1} 의 데이터를 바탕으로 초대칭성 이론에 의해 그 존재가 예측되는 입자인 스칼라 톱 쿼크가 쌍생성된 증거를 탐색하였다. 쌍생성된 스칼라 톱 쿼크는 각각이 R-패러티를 깨뜨리며 타우 렙톤과 바텀 쿼크로 붕괴한다고 가정하였다. 이어서 두 타우 중 하나가 전자나 뮤온 그리고 그에 상응하는 중성미자들로 붕괴하며, 나머지 타우는 강입자들로 붕괴한다고 가정하였다. 데이터의 분석 결과, R-패러티가 깨어지는 스칼라 톱의 붕괴 현상에 대한 증거는 발견되지 않았다. 관측된 사건의 수, 예측되는 배경사건의 수, 그리고 계통오차를 바탕으로 우선 스칼라 톱 쿼크 쌍생성 산란 단면적의 상한치를 95% 유의 수준으로 4.69 pb 에서 설정하였다. 이 결과를 이론적 계산과 비교함으로써 스칼라 톱 쿼크의 질량 하한치를 또한 95%의 유의 수준으로 $119\text{ GeV}/c^2$ 에서 설정하였다.